

Miguel Fernando López Garcia

Modelling and Experimental Testing of an Innovative Sabatier Reactor for a Power-to-Gas Plant

Fraunhofer-Institut für Energiewirtschaft und
Energiesystemtechnik IEE

Miguel Fernando López Garcia

Modelling and Experimental Testing
of an Innovative Sabatier Reactor for a
Power-to-Gas Plant

FRAUNHOFER VERLAG

Kontaktadresse:

Fraunhofer-Institut für
Energiewirtschaft und Energiesystemtechnik IEE
Königstor 59
34119 Kassel
Telefon +49 (0)561 7294-0
Telefax +49 (0)561 7294-100
E-Mail info@iee.fraunhofer.de
URL www.iee.fraunhofer.de

Bibliografische Information der Deutschen Nationalbibliothek

Die Deutsche Nationalbibliothek verzeichnet diese Publikation in der Deutschen Nationalbibliografie; detaillierte bibliografische Daten sind im Internet über <http://dnb.d-nb.de> abrufbar.
ISBN (Print): 978-3-8396-1356-6

D 34

Zugl.: Kassel, Univ., Diss., 2018

Druck: Mediendienstleistungen des
Fraunhofer-Informationszentrum Raum und Bau IRB, Stuttgart

Für den Druck des Buches wurde chlor- und säurefreies Papier verwendet.

© by **FRAUNHOFER VERLAG**, 2018

Fraunhofer-Informationszentrum Raum und Bau IRB
Postfach 80 04 69, 70504 Stuttgart
Nobelstraße 12, 70569 Stuttgart
Telefon 07 11 9 70-25 00
Telefax 07 11 9 70-25 08
E-Mail verlag@fraunhofer.de
URL <http://verlag.fraunhofer.de>

Alle Rechte vorbehalten

Dieses Werk ist einschließlich aller seiner Teile urheberrechtlich geschützt. Jede Verwertung, die über die engen Grenzen des Urheberrechtsgesetzes hinausgeht, ist ohne schriftliche Zustimmung des Verlages unzulässig und strafbar. Dies gilt insbesondere für Vervielfältigungen, Übersetzungen, Mikroverfilmungen sowie die Speicherung in elektronischen Systemen.

Die Wiedergabe von Warenbezeichnungen und Handelsnamen in diesem Buch berechtigt nicht zu der Annahme, dass solche Bezeichnungen im Sinne der Warenzeichen- und Markenschutz-Gesetzgebung als frei zu betrachten wären und deshalb von jedermann benutzt werden dürften. Soweit in diesem Werk direkt oder indirekt auf Gesetze, Vorschriften oder Richtlinien (z.B. DIN, VDI) Bezug genommen oder aus ihnen zitiert worden ist, kann der Verlag keine Gewähr für Richtigkeit, Vollständigkeit oder Aktualität übernehmen.

**Modelling and experimental testing of an
innovative Sabatier reactor for a
Power-to-Gas plant**

Dissertation for the acquisition of the academic degree
Doktor der Ingenieurwissenschaften (Dr.-Ing)

Submitted to the Faculty of electrical engineering and computer sciences
of the University of Kassel

by
Miguel Fernando López Garcia

Day of defence: 16th February 2018

Abstract

The scientific community has proven that anthropogenic actions have contributed to the global warming which has been experienced since industrial revolution times in our planet. Essential actions such as the transition of the actual energy system based on conventional fossil fuels to a system based 100% on renewable sources is required in order to mitigate the impacts on the population and the planet itself. Therefore, several governments worldwide have started to integrate renewable energy generators into their energy systems, these changes should be carried out gradually thus proper policies, social consents are taken into account and technology maturity is achieved. Germany is one of the leading countries in the world which supports and invests in renewable energies. Governmental institutions, the industry sector and scientific experts have foreseen that the expansion towards a 100% renewable energy system is not achievable without an appropriate expansion of energy storage technologies. These technologies can be distinguished themselves by their nature i.e chemical, electrical, electro-chemical, mechanic or thermal. Most importantly, such technologies should be able to receive or inject an amount of energy during a determined period of time, they can also be classified according their storing duration as short-term or long-term energy storage technologies. In an energy system with high penetration of renewable energies is expected that seasonal electricity surpluses arise which means that long-term energy storage technologies are going to play an important role in balancing the demand and production side.

For example Power-to-Gas (PtG) plants are classified as a type of long-term energy storage technologies, PtG plants store electricity surpluses from renewable energy sources most-likely wind and PV farms by producing gaseous energy carriers such as hydrogen and methane. An essential component of the plant consists of a catalytic reactor which operation and temperature control are very important in terms of the efficiency. Some reactor concepts have been adapted for Power-to-gas technologies whereas other innovative ideas are currently being developed. Micro-channel reactors represent an attractive concept due

to their great heat and mass transfer properties. The scope of this doctoral thesis comprises the development of a mathematical model which estimates the concentration of CH₄ in the reactor product gas and its dependency with different operating points. The model consists of partial differential equations which are solved using Matlab-Simulink. Tests are carried out in a lab-scale PtG plant which was built at Fraunhofer Institute for Energy Economics and Energy System Technology (IEE) in Kassel in order to validate the model results and determine the values of the activation energy (E_a), the pre-exponential Arrhenius factor (A) and the empirical coefficient (n). A comparison between the estimated and measured results is presented and discussed, finally conclusions are drawn and some perspectives and recommendations for future projects are presented.

Erklärung

”Hiermit versichere ich, dass ich die vorliegende Dissertation selbständig, ohne unerlaubte Hilfe Dritter angefertigt und andere als die in der Dissertation angegebenen Hilfsmittel nicht benutzt habe. Alle Stellen, die wörtlich oder sinngemäß aus veröffentlichten oder unveröffentlichten Schriften entnommen sind, habe ich als solche kenntlich gemacht. Dritte waren an der inhaltlichen Erstellung der Dissertation nicht beteiligt; insbesondere habe ich nicht die Hilfe eines kommerziellen Promotionsberaters in Anspruch genommen. Kein Teil dieser Arbeit ist in einem anderen Promotions- oder Habilitationsverfahren durch mich verwendet worden.”

30.01.2018

Eigenhändige Unterschrift der Doktorandin/des Doktoranden

Preface

This doctoral thesis is the result of my work as scientific staff member in the project *direct methanation of biogas* which was carried out at Fraunhofer Institute for Energy Economics and Energy System Technology (IEE). I would like to thank the director of the institute Prof. Dr. Clemens Hoffmann for the supervision of this scientific work as well as Prof. Dr. Gunther Kolb for being part of this process as my second supervisor. I would also like to thank Jochen Bard (head of the division *energy process engineering*) and Matthias Puchta (head of the department *Energy storage*) for the support and the helpful feedbacks during these years. I am thankful to Dr. Michael Schwalm for the help provided which allowed me to understand the background of the mathematical equations, Bahram Panahandeh and Fabian Bonnet for the development of the control strategy which enabled the operation of the PtG plant and for the support during the experiments, Ramona Schröder and Frank Schünemeyer for the project management and construction of the PtG plant respectively, Daniel Hau and Matthias Wecker for their support regarding the PLC software, Philipp Ackermann and Dominik Manteuffel for the support provided on the electrical component of the PtG plant. I also am enormously thankful to my parents and sister who have always been by my side to unconditionally support and encourage me.

Nomenclature

A	Pre-exponential factor of the Arrhenius form	$[mol^{1/n-5}m^{15-3/n}sec^{-1/n}]$
A_c	Channel cross-sectional flow area	$[m^2]$
C_p	Heat capacity of the gas phase	$[J/kgK]$
$D_{k,Kn}^e$	Effective Knudsen diffusion coefficient	$[m^2/sec]$
D_{kl}	Binary diffusion coefficients	$[m^2/sec]$
D_{kl}^e	Effective binary diffusion coefficient	$[m^2/sec]$
D_{km}	Mean mixture diffusion coefficient	$[m^2/sec]$
E_a	Activation energy	$[J/mol]$
f	Friction factor	$[-]$
G	Gibbs free energy	$[-]$
G_r°	Standard molar Gibbs free energy	$[-]$
G_z	Graetz number	$[-]$
H	Enthalpy	$[J/mol]$
H_{ch}	Channel height	$[m]$
h_k	Species heat enthalpy	$[J/mol]$
h_{conv}	Heat transfer coefficient	$[W/m^2K]$
j_k	Diffusive mass flux of gas-phase species	$[kg/m^2sec]$
k_b	Boltzmann constant	$[J/K]$
K_{eq}	Reaction equilibrium constant	$[-]$
K_g	Number of gas species	$[-]$
k_f	Forward rate constant	$[mol^{1/n-5}m^{15-3/n}sec^{-1/n}]$
k_r	Backward rate constant	$[mol^{1/n-3}m^{9-3/n}sec^{-1/n}]$
L	Channel length	$[m]$
n	Empirical coefficient	$[-]$
N_u	Nusselt number	$[-]$
P	Gas phase pressure	$[Pa]$
P_c	Catalytically active perimeter of the channel	$[m]$

D_h	Hydraulic diameter of the channel	$[m]$
P_k	Partial pressure of species k	$[Pa]$
P'	Corrected partial pressure of species k	$[Pa]$
P'_{know}	Normalised partial pressure of species k	$[Pa]$
Pr	Prandlt number	$[-]$
q	Global rate of progress of the Sabatier reaction	$[mol/m^3sec]$
q_g	Heat flux	$[W/m^2sec]$
\dot{q}_{qw}	Convective heat transfer rate between channel flow and reactor channel wall	$[W/m^3]$
R	Universal gas constant	$[J/molK]$
Re	Reynolds number	$[-]$
S	Entropy	$[J/molK]$
\dot{s}_k	Molar production rate of species by surface reaction	$[mol/m^2sec]$
s_v	Space velocity	$[sec^{-1}]$
t	Time	$[sec]$
T	Absolute temperature	$[K]$
T_g	Temperature of the gas phase	$[K]$
T_w	Channel wall temperature	$[K]$
u	Mean gas phase velocity	$[m/sec]$
\dot{V}_{kest}	Estimated outlet volumetric flow of species k	$[l/h]$
\dot{V}_{kin}	Inlet volumetric flow of species k	$[\%]$
\dot{V}_{kmes}	Measured outlet flow of species k	$[l/h]$
\dot{V}_{knew}	New outlet volumetric flow of species k	$[l/h]$
$\dot{V}_{totalnew}$	New total volumetric flow	$[l/h]$
W_{ch}	Channel width	$[m]$
W_{jk}	reduced molecular weight	$[g/mol]$
W_k	Species molecular weight	$[kg/mol]$
\bar{W}	Average molecular weight of the gas phase	$[kg/mol]$
x	Spatial coordinate	$[m]$
X_k	Gas species mole fraction	$[-]$
X_{knew}	Gas species mole fraction (water considered)	$[-]$
$[X_k]$	Gas species mole concentration	$[mol/m^3]$
$[X_T]$	Total gas phase mole concentration	$[mol/m^3]$
Y_k	Species mass fraction	$[-]$
α	Channel aspect ratio	$[-]$

λ	Thermal conductivity of the gas phase	$[W/mK]$
μ	Viscosity of the gas phase	$[Nsec/m^2]$
ν_k	Species stoichiometric coefficient	$[-]$
ρ	Mass density of gas phase	$[kg/m^3]$
τ	Educt residence time in the reactor	$[sec]$
τ_w	Wall shear stress	$[Pa]$
ϵ	Reduced potential well depth	
σ	Reduced collision diameter	$[Å]$
$\xi_{H2_{est}}$	Estimated conversion of hydrogen	$[-]$

Acronyms

IMM	Fraunhofer Institute for Microengineering and Microsystems
IEE	Energy Economics and Energy System Technology
ISI	Fraunhofer Institute for Systems and Innovation Research
IPCC	Intergovernmental Panel on Climate Change

Abbreviations

ACAS	Adiabatic compressed-air storage systems
AE	Alkaline electrolysis
CHP	Combined heat and power
CSTR	continuous stirred-tank reactors
HHV	Higher heating value of hydrogen
EEG	Erneuerbare-Energien-Gesetz
el	Electric
GW	Gigawatt
HBFZ	Hessian Biogas Research Center
MW	Megawatt
PEME	Polymer electrolyte membrane electrolysis
RE	Renewable energies
RES	Renewable energy sources
ROR	run-of-the river hydro-power
PHSP	pumped-hydro electric storage plants

PtG	Power-to-Gas
SNG	Substitute natural gas
SOE	Solid oxide electrolyte electrolysis
TWh	Terawatt hour
th	Thermic

Introduction

Climate change is one of the biggest challenges that humanity will face in the next decades. It is crucial to ensure a successful energy transition from a system based on fossil fuels to a safe, affordable and reliable system based on renewable energy sources (RES) such as the sun, wind, geothermal, hydro-power and biomass. Such a transition can be achieved by developing new technologies and strategies which promote the use of e.g. clean electricity or heat as well as promote the increase in the energy efficiency. Germany has already started its energy transition, several clean technologies are mature, operational and produce more than 25% of the electricity [1]. Further growth and funding for technology development is foreseen in the near future. In this context, renewable energies (RE) are expected to contribute with 40 - 45% of the electricity production by 2025, 55 - 60% by 2035 and at least 80% by 2050 [1].

However, the production of electricity through RE represents well-known challenges for the infrastructure of the actual electrical system such as the fluctuation of the electricity production, its volatility and forecasting errors inherent to the resource. These issues cause grid stability problems as a consequence of the mismatch between produced and consumed electricity. This issue can be overcome by developing and integrating storage technologies which are either able to deliver or take high quantities of energy in short or relatively long periods of times according to the temporal demand. Although, this issue is actually managed in Germany mainly by 0.04 TWh of pumped-storage hydropower plants (PHSP) [2], it is foreseen that PHSP and other storage technologies such as adiabatic compressed-air storage systems (ACAS) and batteries will not be able to supply the required storage capacity to balance the electric grid in the future [2][3].

In this context, the PtG concept which is described in section 2.1 represents an alternative to store electricity in form of gaseous energy carriers such as hydrogen and methane

for a long period¹ of time due to the large storage capacity of the German gas grid compared to other storage technologies. PtG plants consists of two components, one where hydrogen is produced via *electrolysis* and a second where hydrogen reacts with carbon dioxide/monoxide to produce methane (*Sabatier reaction*). The latter is called methanation and currently, five different Sabatier reactor concepts have been tested for this process step: fixed-bed, fluidised-bed, honeycomb, bubble column and micro-channel reactor, their respective description as well as pros and cons are presented in section 1.4.2.

Fraunhofer Institute for Energy Economics and Energy System Technology (IEE) in cooperation with Fraunhofer Institute for Microengineering and Microsystems (IMM) have decided to pursue a roadmap to develop PtG plants from lab- to demo-scale. The reactor concept which is adopted for this purpose is a micro-channel reactor whereas the production of hydrogen will be provided via Polymer Electrolyte Membrane Electrolysis (PEM)². As first scale, a 10 kW³_{th} lab-plant to gain experience was built up; as second scale a 50kW⁴_{el} is planned to start operating by 2017 in the Hessian Biogas Research Center (HBFZ). As further step, a 500kW⁵_{el} PtG plant will be integrated to a biomass plant in the federal state of Thüringen - Germany. In all cases the Sabatier-reactor is manufactured and delivered by Fraunhofer IMM.

Within this roadmap, the objective of this doctoral thesis is ***modelling and experimental testing of an innovative reactor for a Power-to-Gas plant***. In order to achieve the objective, a mathematical model considering physical and chemical processes in the reactor was programmed in Matlab-Simulink. Different operating points regarding the temperature, pressure and inlet volumetric flow of educt gas were simulated. Subsequently, experimental test were carried out in order to acquire data which allowed model validation. The model will be used as an state observer for a pilot PtG plant.

In chapter 1 of this doctoral thesis, the role of energy storage technologies in a renewable energy based system is discussed. Additionally, the PtG technology as a way to store electricity surpluses is introduced. Moreover, the state of the art of water electrolyser, a

¹In the range of days, weeks and even months

²Except for the lab-scale where hydrogen was supplied by conventional gas bottles.

³The rated power refers to the caloric value of the product gas.

⁴The rated power refers to the electrical rated power of the electrolyser. The PtG plant will be built up in HBFZ and offers the possibility to apply the knowledge acquired in the lab-scale plant.

⁵The rated power refers to the electrolyser.

comparison between the biologic and catalytic methanation as well as a comparison between the reactor concepts used for methanation is presented. Chapter 2 introduces the PtG concept, it discusses the technology efficiency and different sources of carbon dioxide. Additionally, the option biogas as carbon dioxide source in Germany for PtG plants is presented. This chapter concludes by presenting the different carbon dioxide capture and storage technologies (CCS). Chapter 3 describes the modelling of the chemical equilibrium for the methanation reaction as well as the governing equations of the mathematical model. Additionally, this chapter presents the simulation environment, model estimates and how the reactor model is going to be implemented in the control strategy. Chapter 4 describes the components and sub-components of the lab-scale PtG plant such as *gas supply, methanation unit and technique of measurement*. Chapter 5 presents the conditions at which the experimental tests were carried out, a comparison between the model estimates is as well presented. The plant was operated at four different points regarding the inlet volumetric flow of educt gas (0.25, 0.50, 0.75 and 1.0 Nm³/h), the reactor operating pressure and temperature were set to 15 bar and 350 °C, water vapour was condensed and separated from the product gas downstream the reactor. In order to analyse the product gas composition samples were taken and sent to a laboratory. Chapter 6 discusses the results and gives an outlook of the new steps which are needed in future projects.

Contents

List of Figures	xxi
List of Tables	xxv
1 Theoretical background and technological state of the art	1
1.1 Role of energy storage technologies in a renewable energy based system	1
1.2 Power-to-gas as energy storage technology	8
1.3 Electrolysis	10
1.3.1 Alkaline electrolysis	10
1.3.2 Polymer Electrolyte Membrane electrolysis	11
1.3.3 Solid oxide electrolysis	12
1.4 Methanation	13
1.4.1 Biologic methanation	14
1.4.2 Catalytic methanation	17
1.4.2.1 Conventional reactor concepts	17
1.4.2.2 Innovative reactor concepts	26
1.4.2.3 Mechanisms of catalyst deactivation	36
1.4.3 Summary and conclusions	37
2 PtG concept and carbon dioxide sources	41
2.1 Concept	41
2.2 Carbon dioxide sources	42
2.2.1 Biogas as carbon dioxide source	43
2.2.2 Carbon dioxide capture and storage technologies	44
3 Modelling	53
3.1 Chemical equilibrium	53

3.2	Governing equations	56
3.2.1	Temporal derivative of the species mass fraction	58
3.2.2	Temporal derivative of the velocity	60
3.2.3	Temporal derivative of the temperature	62
3.3	Determination of the kinetic parameters of the Sabatier reaction	63
3.3.1	Lunde and Kester approach	63
3.3.2	Experimental runs	66
3.4	Spatial discretisation	71
3.5	Model structure and simulation environment	72
3.5.1	Model structure	72
3.5.2	Simulation environment	73
3.5.3	Model results	75
3.5.3.1	Temperature effect on the CH ₄ , CO ₂ and H ₂ outlet volumetric percentage	76
3.5.3.2	Pressure effect on the CH ₄ , CO ₂ and H ₂ outlet volumetric percentage	78
3.5.3.3	Effect of the inlet volumetric rate on the CH ₄ , CO ₂ and H ₂ outlet volumetric percentage	81
3.6	Control strategy and the reactor model	83
3.6.1	Reactor model as state observer	84
4	PtG lab-scale plant	85
4.1	Gas supply	85
4.2	Methanation	86
4.3	Technique of measurement	89
5	Experimental set-up and results	91
6	Discussion	93
	Bibliography	95
7	Appendix	109

List of Figures

1.1	RE installed capacities for the 40%, 63% and 80% scenario	2
1.2	Residual load for a 100%-RE scenario	3
1.3	Pumped hydro electric storage plants for a 40%-RE scenario and adequate areas	4
1.4	Energy storage technologies	8
1.5	Residual load for different RE-based scenarios	9
1.6	Spatial distribution of PtG plants for a 85%-RE scenario in Germany	10
1.7	Anaerobic degradation of organic biomass to methane	15
1.8	Methanogenic bacteria	15
1.9	Lurgi coal gasification process	19
1.10	Graphical representation of the Great Plains Synfuels Plant	20
1.11	Simplified HICOM process flow diagram	21
1.12	Linde process for SNG and isothermal reactor	22
1.13	Fixed-bed RMP process flow diagram	22
1.14	Fluidised bed reactors	24
1.15	Comflux pilot plant and process flow diagram	25
1.16	Slurry bubble reactor used by Shaikh	27
1.17	Three-phase methanation (Chem System Inc.)	29
1.18	Three-phase methanation reactor (KIT) and the effect of the solids loading as well as the effect of the gas phase velocity on the bubble size.	30
1.19	Honeycomb reactor developed at KIT	31
1.20	Membrane micro-reactor designed by Cui et al.	33
1.21	Cross section of the double-side (left) and one-sided (right) silicon heat exchangers manufactured by Aleppe et al	33
1.22	Cross-flow heat exchanger/reactor	35
1.23	Counter-flow heat exchangers/reactors developed at Fraunhofer IMM	36

2.1	Power-to-Gas concept	41
2.2	Power-to-Gas efficiency	42
2.3	CO ₂ potentials and locations for PtG plants in Germany	44
2.4	Post combustion CCS pilot plant using reactive absorption	46
2.5	CO ₂ absorption pilot plant in Esbjerg (Denmark)	47
2.6	Reactor types used for CLC purposes	49
2.7	Hydrate based gas as CCS technology (process flow diagram)	51
3.1	Volumetric concentration of CH ₄ and CO ₂ in equilibrium.	56
3.2	Determination of the activation energy using the method proposed by Lunde and Kester.	66
3.3	Estimated and measured vol.% of CO ₂ , H ₂ , CH ₄ as well as estimated vol.% of H ₂ O used in the determination of the activation energy.	68
3.4	Estimated and measured vol.% of CO ₂ , H ₂ , CH ₄ as well as estimated vol.% of H ₂ O used in the determination of the pre-exponential Arrhenius factor.	68
3.5	Standard deviation of the Y values with respect to the curve fit vs the empirical coefficient n	69
3.6	Y vs the inverse of the reactor mean temperature. Experimental data used to determine the activation energy of the Ru-based catalyst in the reactor.	70
3.7	Y vs the inverse of the reactor mean temperature. <i>Left:</i> Experimental data found by Lunde und Kester [4]. <i>Right:</i> Experimental data used to determined the activation energy of the Ru-based catalyst in the reactor.	71
3.8	Discretisation of the spatial coordinate.	71
3.9	Optimum number of segments.	72
3.10	Structure of the Matlab-Simulink model	72
3.11	Subsystem state of variables (graphical representation)	73
3.12	Micro-channel function and integration Subsystem	74
3.13	Structure of the integration subsystem	74
3.14	Simulation environment programmed in Matlab-Simulink	75
3.15	Vol.% of the gas components along the reactor length; Inlet volumetric flow 1 Nm ³ /h and 350 °C.	76
3.16	Temperature effect on the CH ₄ outlet volumetric percentage. 1 Nm ³ /h inlet volumetric flow of educt gas, 15 bar reactor operating pressure.	77
3.17	Temperature effect on the CO ₂ outlet volumetric percentage. 1 Nm ³ /h inlet volumetric flow of educt gas, 15 bar reactor operating pressure.	77

3.18	Temperature effect on the H ₂ outlet volumetric percentage. 1 Nm ³ /h inlet volumetric flow of educt gas, 15 bar reactor operating pressure.	78
3.19	Pressure effect on the CH ₄ outlet volumetric percentage. 1 Nm ³ /h inlet volumetric flow of educt gas, 350 °C reactor wall temperature	79
3.20	Pressure effect on the CO ₂ outlet volumetric percentage. 1 Nm ³ /h inlet volumetric flow of educt gas, 350 °C reactor wall temperature	80
3.21	Pressure effect on the H ₂ outlet volumetric percentage. 1 Nm ³ /h inlet volumetric flow of educt gas, 350 °C reactor wall temperature	80
3.22	Effect of the inlet volumetric flow on the CH ₄ outlet volumetric percentage. 350 °C reactor wall temperature and 15 bar operating pressure.	81
3.23	Effect of the inlet volumetric flow on the CO ₂ outlet volumetric percentage. 350 °C reactor wall temperature and 15 bar operating pressure.	82
3.24	Effect of the inlet volumetric flow on the H ₂ outlet volumetric percentage. 350 °C reactor wall temperature and 15 bar operating pressure.	82
3.25	State machine	83
4.1	Gas supply	85
4.2	Pressure reducers	86
4.3	Type of platelets in the reacting stack	87
4.4	Methanation reactor and its reacting stack	87
4.5	Plate heat exchanger and three-way valve	89
4.6	Pump	89
4.7	Overview of the micro gas chromatograph	90
5.1	Measured, estimated and equilibrium concentration of CH ₄ . Operating conditions: 350 °C, 15 bar, 0.25, 0.50, 0.75 and 1.0 Nm ³ /h.	91
7.1	PtG lab-scale plant. Source: Fraunhofer IEE	109
7.2	PtG process diagram. Source: Fraunhofer IEE	110
7.3	Experimental conditions and outlet partial pressures of the gas components used for the determination of E_a	111
7.4	Experimental conditions and outlet partial pressures of the gas components used for the determination of the pre-exponential Arrhenius factor A	112
7.5	Y vs the inverse of the reactor temperature. Comparison between the values found by Lunde and Kester and the values found experimentally in the lab.	113

7.6	Values of the activation energy E_a and the pre-exponential Arrhenius factor	
	A vs n	114

List of Tables

1.1	Comparison of the electrolyser technologies	13
1.2	Operation parameters and gas composition in the pilot plant of the Lurgi process	18
1.3	Gas composition of ADAM I	20
1.4	Dry gas composition of the RMP process at 27 bar	23
1.5	Operating conditions of the Thyssengas pilot plant	25
1.6	Comparison between catalytic and biologic methanation	38
1.7	Reactor concept pros and drawbacks	39

1 Theoretical background and technological state of the art

In section 1.1 the role of energy storage technologies in a renewable energy based system is discussed. Additionally, different storage technologies e.g. PHSP, pore and cavern storage, flywheel among others are presented. In section 1.2 the PtG technology is introduced as a way to store electricity surpluses, a discussion about how much PtG installed capacity for different RE-based scenarios is presented. In section 1.3 electrolyzers technologies are presented, their technical and operating characteristics as well as the drawbacks of each technology and how the integration with RES is affected are mentioned. Section 1.4 describes the biological and catalytic methanation processes, the differences between them are commented. Finally, this section presents different reactor concepts used for biologic and catalytic methanation.

1.1 Role of energy storage technologies in a renewable energy based system

Germany has decided to change its actual energy system in order to reduce greenhouse emissions by 80% - 95% until 2050 compared to 1990 [5] and consequently reach the goals established by the IPCC [6]. Jentsch [5], discussed in her work three different scenarios regarding the share of RE in the German gross electricity consumption until 2050. The first scenario corresponds to a renewable energy share of 40% and it is supposed to be reached by 2020. This scenario considers photovoltaic farms as the most dominant technology with an installed capacity of 53.5 GW followed by onshore and offshore wind farms with an installed capacity of 39 and 10 GW respectively, 7.8% of the share is assumed to be provided by other renewable technologies¹. The next scenario has to be reached by 2030 and corresponds to

¹As other renewable technologies, river power plant, geothermal power and bio CHP power stations are considered

a share of 63%, by then there will be 65 GW of photovoltaic farms installed, 46 GW of onshore wind farms and 24 of offshore wind farms, 8.4% of the share is assumed to be provided by other renewable technologies¹. The last scenario is supposed to be reached by 2050, it corresponds to a 85% share of the gross electricity generation and can be divided as follows: 79 GW installed of photovoltaic farms; 54.3 GW of onshore wind farms, 34.5 GW of offshore wind farms and 10.5% of the share provided by other renewable technologies¹ [7]. *Figure 1.1* illustrates the scenarios mentioned above. Furthermore, Fraunhofer IEE carried out a study where 100% electric supply in Germany through RE sources is considered. It was concluded that for a such scenario, 60% from the electricity supply should be provided by wind farms which corresponds to an installed capacity of 87 GW onshore wind farms, 40 GW offshore wind farms, 20% of the electricity supply by photovoltaic farms (133.7 GW), 20% by bioenergy (17.3 GW) and 10% by hydroelectric and geothermal power (9.5 GW) [8]. Wind farms should operate 8.760 hours i.e. the complete year whereas biogas plants and photovoltaic farms should operate below 8000 and 5000 hours respectively [8].

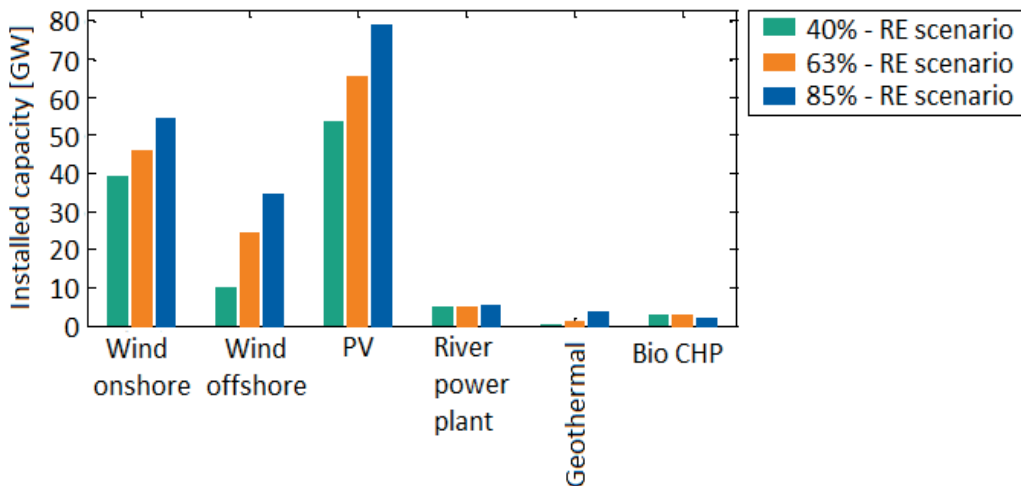


Figure 1.1: RE installed capacities for the 40%, 63% and 80% scenario [9].

An increase of RE in the energy system implies fluctuation of the electricity production due to the seasonal changes of the resource. Spatial balance of the power generated and consumed can be achieved by transporting electricity from a region(s) where surpluses arise to a region(s) where there is a need of electricity. However, it is important to note that this mechanism is not always possible due to capacity limitations of the electric grid infrastructure or the demand/production profile between regions. Temporal balance of the electric grid can be achieved by storing electricity surpluses for a period of time in order to be used when required. However, appropriate energy storage technologies which

are integrated in an adequate manner, which are flexible enough and able to meet the grid requirements every time must be developed and deployed. *Figure 1.2* illustrates the residual load considering 100% electricity production from RE sources. If the complete year for this scenario is considered, around 187.7 TWh electricity surpluses are expected to be generated [10].

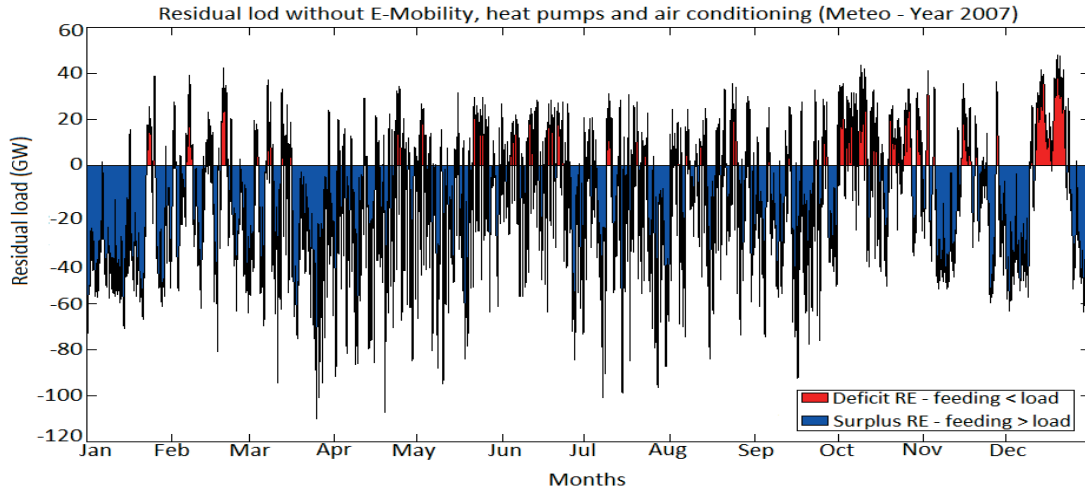


Figure 1.2: Residual load for a 100%-RE scenario [10].

Energy storage technologies can be classified into short term storage technologies which are able to store/deliver electricity for few hours and long term storage technologies which are able to store/deliver electricity surpluses for a time period of weeks or months. If all other sources of energy are shut down, the latter type is expected to balance the electric grid for a period of days considering the average consumption in Germany [8]. PHSP pump water to a higher reservoir at times when electricity surpluses arise to be later directed to a turbine in order to meet the electricity demand, its storage capacity depends on the reservoir height and size. This type of storage technology has an efficiency between 70% - 80% [11][12] and an energy density between 0.2 - 1.6 kWh/m³. Considering a height of the water column between 70 - 600 m, pumped hydro electric storage plants are flexible e.g. the power plant Goldisthal which has a rated capacity of 1060 MW is able to operate its turbine at full load within 98 seconds and its pump within 256 seconds, this power plant can operate for 8 hours which corresponds to a storage capacity of 8480 MWh [12] per day. The role that this technology can play in a 100% RE scenario depends on the geographical conditions [8]. The study presented by Knorr et al. [8] for the 2020 scenario suggested the operation of 39 PHSP (83.7 GWh capacity) with a generating, pumping capacity of 11.1 and 12.2 GW respectively, two ACAS systems with a generating capacity of 0.4 GW and

a pumping capacity of 0.2 GW are as well considered. Moreover, PHSP are estimated to operate more often during summer than winter due to the fact that PHSP are normally designed to support the distribution of the feed-in capacity of photovoltaic systems during the day. *Figure 1.3* depicts the spatial distribution of PHSP and identified areas for new projects in Germany. For example, in the federal state Thüringen, 13 locations with a potential of 5.1 GW were identified [12]. In Bayern, 16 locations with a potential of 11 GW were identified [12]. In the federal state Baden-Württemberg 13 locations with a total capacity of 19 GW were identified [12]. In Nordrhein-Westfalen, 5 locations with a potential of 1.4 GW were identified [12].

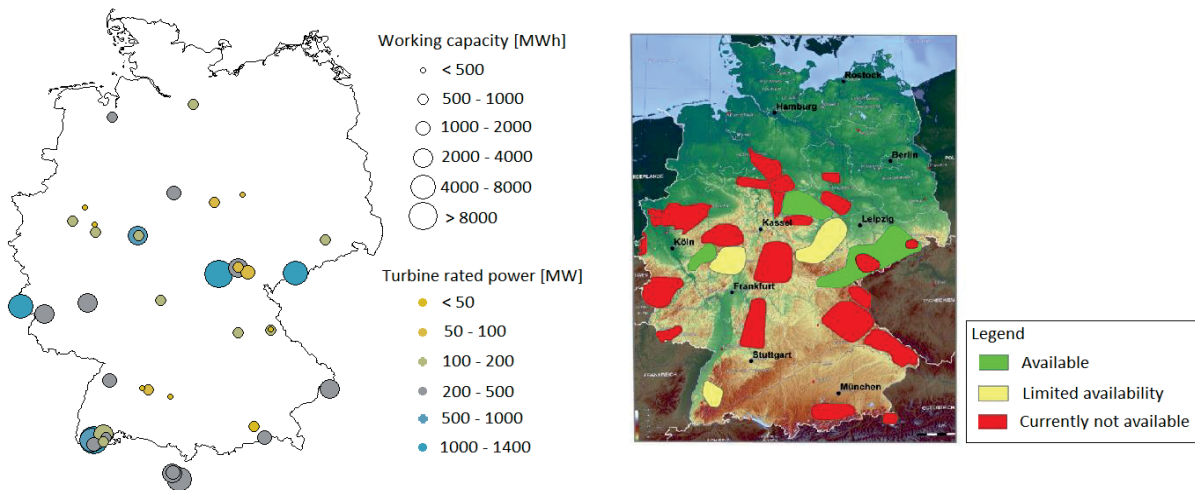


Figure 1.3: Pumped hydro electric storage plants for a 40%-RE scenario and adequate areas [8].

In addition to PHSP, there is a high potential to store energy with pore and cavern storage technologies. Thereby, hydrogen, air, methane and carbon dioxide can be compressed and stored in underground hollow voids or pressurised containers to be used when required. Among the aforementioned gases, methane has the highest calorific value (1100 kWh/m³ at 120 bar) followed by hydrogen (280 kWh/m³ at 120 bar) and compressed air (2.9 kWh/m³ at 20 bar) [12]. There is a maximal potential² in Germany of 325 TWh if new pore and cavern storage systems with a total volume of 11.6 and of 19.3 billions Nm³ respectively are considered [12]. Moreover, the *Zentrum für Energieforschung Stuttgart* reported in 2012 a maximal potential³ of 671 TWh for compressed air and 1763 TWh for

²It refers to the amount of chemical energy which can be stored in form of methane for that specific volume of cavern and pore storage systems.

³It refers to the potential of salt caverns in the north of Germany. It is important to note that unavail-

hydrogen. Flywheel energy storage systems store electricity surpluses in form of rotational energy. This technology consists of an electric motor/generator, a bearing, the flywheel itself and a frequency converter which allows to output the grid frequency even though the rotational speed can vary during the charging/discharging process [11]. The limiting factor regarding the maximal value of the rotational speed which can be reached is the tensile strength of the material, therefore light materials with high tensile strengths are preferred in order to achieve high energy densities [12][11]. Flywheel energy storage systems can be classified as low-speed or high-speed flywheels. On the one hand, low-speed flywheels are made of metallic components, an operating range of 5000 - 10000 rpm and an energy density of 5 Wh/kg [11][12] can be achieved. On the other hand, High-speed flywheels can operate in a higher range regarding the rotational speed (up to 100000 rpm), thus energy densities of 100 Wh/kg can be achieved; the normal application range regarding the rated power and storage capacity of flywheels spans between 100 - 250 kW and 3.3 - 25 kWh respectively [11][12]. Since, flywheels can be charged and discharged very quickly (within milliseconds with an efficiency of 95%), this type of energy storage technology is adequate and preferred to feed in or receive peak power [11][12] for short periods of time.

Superconducting magnetic energy storage systems represent another type of technology. These storage technologies store direct current which is then used as a source of a magnetic field [13][12][11]. During the charging process a coil with superconductive properties is supplied with direct current produced by a rectifier, thereby a magnet field is created and energy can be stored, once the charging process is completed the circuit is closed by using a superconductive switch. During the discharging process, the circuit is connected to an inverter in order to produce alternative current. Theoretically speaking, superconducting magnetic energy storage systems can reach efficiencies up to 97% for both charging and discharging processes, rated powers around 10 MW and storage capacities of 5.6 kWh are common for this type of energy storage technology [12]. The main drawback is the cooling effort for getting the superconductive properties of the materials, this leads to 10 - 12% of losses per day and therefore this type of technology is adequate to be deployed for short term storage [12][11]. Energy densities between 300 - 3000 Wh/kg can be reached. Additionally, due to the high flexibility of this type of storage technology, superconducting magnetic energy storage systems can ensure grid and voltage quality. Capacitors are

ability due to other uses and ecological constraints have to be considered. Additionally, compressed air which has the lowest calorific value could represent up to 700 times of the actual PHSP installed capacity in Germany [12].

another type of storage technology, these store energy through physical and chemical processes. Capacitors can be divided into electrochemical-double layer, hybrid and pseudo capacitors, a large number of capacitors are used as part of electric devices and their lifespan is higher than 1 million operating cycles. Capacitors are mainly made of two separated electrodes and a dielectric material where electricity flows through and it is stored even after the supply is interrupted. According to Doetsch et al. [12] an efficiency of 85 - 98% can be achieved with supercapacitors which have an electrolytic solution between the electrodes instead of a dielectric material, energy densities from 5 - 10 Wh/kg can be reached with capacitors available in the market. Capacitors are normally use during short periods of time to provide or receive large amount of power and they can be integrated in wind turbines in order to assist the blade control or emergency shut-down processes [11][12][14]. Plant sizes for double-layer capacitors have 1.5 MW rated powers and storage capacities of 0.002 MWh [15].

Batteries are another type of energy storage technologies, these use electrochemical reactions for the charging and discharging processes. Batteries can be deployed in different areas depending the parameters and properties, in this doctoral thesis the technical aspects of lead-acid, nickel-based, lithium-ion, high temperature and redox-flow batteries are discussed. Lead-acid batteries are commercially available, this type of battery is used normally for grid stabilisation purposes, lead-acid batteries can reach an energy density between 50 - 100 wh/l and efficiencies in the range of 75% - 80%. Common plant sizes of lead-acid batteries span in the range of 1 - 5 MW rated power and up to 10 MWh storage capacity [12][15]. Nickel-cadmium batteries are considered as a state of the art technology which can offer energy densities between 25 - 80 Wh/kg (35 - 135 Wh/l) [12] and an efficiency of 70%. Additionally, nickel-cadmium batteries can be deeply discharged for a decent number of cycles and are able to work at temperatures below 0 °C [11]. However, nickel-cadmium batteries are not environmentally friendly and expensive to manufacture. This type of battery is used as start batteries or for emergency current supply, it is common to find plant sizes in the range of 27 MW - 46 MW rated power [12]. Lithium-ion batteries are implemented for electro-mobility purposes as well as intermediate storage systems specially when electricity is produced by RE [12]. Compared to other types of batteries, Li-ion batteries have a high energy density (100 -160 Wh/kg) and efficiencies in the range of 90% - 95%, this type of battery can be used 1000 - 5000 cycles (5 - 10 years) [12]. Unlike other types of batteries, high temperature batteries operate at temperatures

at which the electrodes melt and the electrolyte remains solid, due to temperature fluctuations during operation a precise control strategy for the temperature must be integrated in order to avoid material stress or damage [12]. ZEBRA batteries are an example of high temperature batteries, their electrodes are made of sodium (negative electrode) and nickel chloride (positive electrode), efficiencies of 91% as well as energy densities from 80 - 100 Wh/kg (140Wh/l) are reported by Doetsch et al. [12]. Sodium-sulphur batteries are another example of high temperature batteries, Sodium-sulphur batteries have a higher energy density than ZEBRA batteries (130 Wh/kg) and efficiencies of 87%, the operating temperature range spans between 290 - 360 °C, Sodium-sulphur batteries can be used between 1000 - 4000 operating cycles i.e. approximately 15 years, common plant sizes span between 1 MW - 52 MW rated power and have a storage capacity between 7 MWh - 254 MWh [12][11]. Redox-flow batteries represent another type of battery, the storage and conversion process in this type of battery take place spatially separated, consequently power and storage capacity can be independently dimensioned. These batteries consist of two separated tanks which contain the electrolyte and a stack where the energy conversion takes place [12]. For this type of battery a pump is used in order to feed the electrolyte material from the tanks to the stack. Moreover, due to the spatial separation of the electrolyte, redox-flow batteries present almost no self discharge and can be deep discharged. However, redox-flow battery systems are complex because additional components such as pumps, sensors and tanks are required [12]. Vanadium-redox batteries for example have an efficiency of 80% (considering the periphery) [12]. According to Doetsch et al. [12], there are vanadium- and polysulphide-bromide-redox systems operating in the United States, Japan, Australia and England with a rated power up to 15 WM and a storage capacity of 120 MWh [12]. According to Fraunhofer ISI, common plant sizes span between 0.01 - 2 MW with a storage capacity between 0.1 - 2 MWh and these plants are used for storing energy within hours or up to one day [12]. In this section different technologies that can be used and deployed to store energy from RE in the electric system were discussed. The advantages and disadvantages of these technologies were also discussed as well as the range in which these technologies can store energy i.e. kWh, MWh, GWh, TWh. Considering long term storage, chemical storage technologies for instance PtG offers the possibility to store energy in the range of TWh which means that electricity supply can be guaranteed for periods of time longer than a month [16], this represents an advantage when comparing PtG plants to PHSP which can store electricity in the range of GWh and therefore PHSP can only provide electricity for no longer than an hour if the total electricity consumption

of Germany (600 TWh [9]) were to be supplied. PtG technologies can contribute to the grid stability by transforming electricity surpluses into rich-energy gases which are stored in the existing gas infrastructure. These gases can be used to produce electricity at times when RES are not able to meet the load. Furthermore, these gases can be transported through the gas infrastructure which represents a balancing strategy of the electric grid from the geographic point of view. Additionally, PtG technologies allow the development of synergies between RE, the heating sector, the mobility sector, as well as the chemical and metallurgical industry [5]. *Figure 1.4* illustrates the storage capacity of different technologies. PtG as energy storage technology is discussed in the following section.

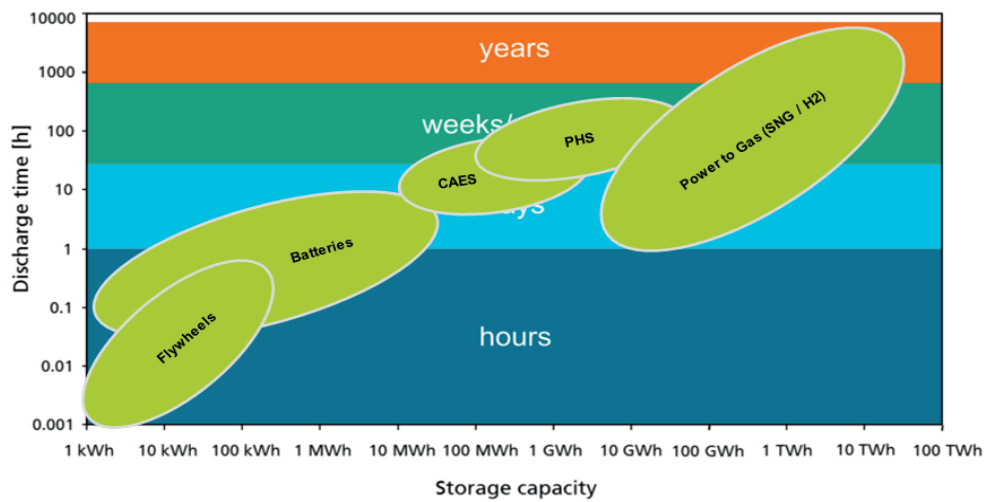


Figure 1.4: Energy storage technologies [9].

1.2 Power-to-gas as energy storage technology

Considering a 85%-RE scenario, PtG technologies are important in the sense of balancing the grid by storing electricity surpluses in the range of terawatt hour and thereby enabling seasonal storage. In this section, the analyses are based on the scenarios presented by Jentsch et al. [9] where a gross electricity demand⁴ in Germany of 573, 571 and 622 TWh is expected as well as a share of RE in the electricity system of 40%, 63%, 85% by 2020, 2030, 2050 respectively [17][9]. *Figure 1.5* illustrates the estimated residual load in Germany for the aforementioned scenarios with and without demand side management (DMS). For the

⁴The value considers transmission losses, power plant own consumption as well as the electricity associated to chemical and PHSP [9].

40%- and 63%-RE scenarios, it can be seen that the residual load is positive (RE-feeding < load) almost throughout the complete year. However, delays of the electric grid expansion for these scenarios could lead to the production of electricity surpluses, PtG plants could therefore be deployed to store these electricity surpluses. For the 85%-RE scenario, it can be seen that the residual load is estimated to be negative (RE-feeding > load) from the beginning of the second half of the year.

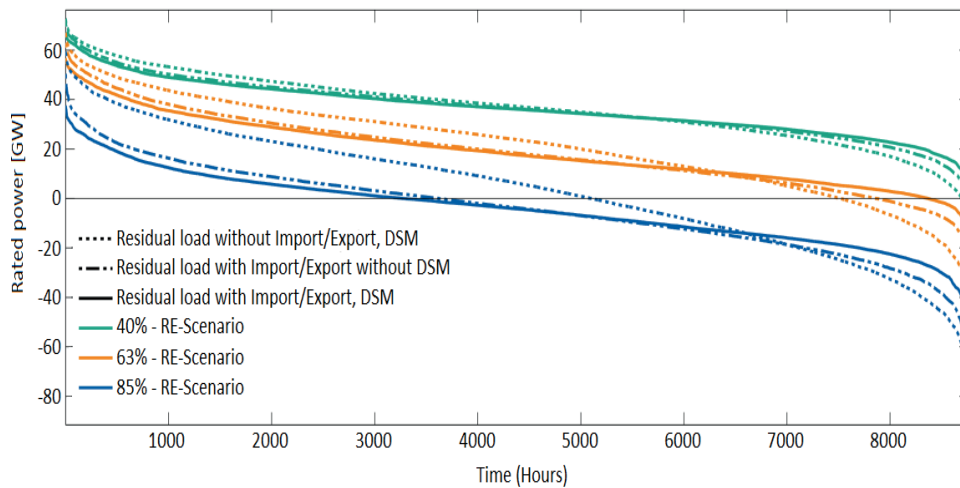


Figure 1.5: Residual load for different RE-Based scenarios [5][9].

Jentsch et al. [9] reported that for the 63%-RE scenario⁵, an amount of 800 GWh/year electricity surpluses are expected. Considering this scenario PtG plants can store 3.7 TWh/year electricity surpluses from the electric grid which corresponds to an installed rated power of 2 GW and an operating time of 1900 full hours. Furthermore, since the CH₄ produced by PtG plants can replace the use of fossil fuels, a reduction of CO₂ equivalent emissions around 0.5 Millions/year in the electric system is expected [9]. 70 TWh/year electricity surpluses are estimated to be produced for the 85%-RE scenario, optimally speaking, PtG plants should be located close to the areas where electricity surpluses arise in order to avoid unnecessary grid expansion and transmission losses i.e. PtG should operate and store the electricity surpluses most likely in regions 21 and 22 (*see figure 1.6*) where a considerable amount of electricity will be produced by onshore and offshore wind farms [9]. Besides region 21 and 22, it is estimated that PtG plants operate as well in the eastern and southern parts of Germany (region 83 and 42) [9]. Additionally, there are other factors that must be considered when determining optimal locations for the operation of

⁵The scenario assumes delays on the expansion of the grid infrastructure

1. Theoretical background and technological state of the art

PtG plants e.g. an adequate CO₂ supply, a gas feeding point, possibility to use the reaction heat and the oxygen produced via electrolysis [5].

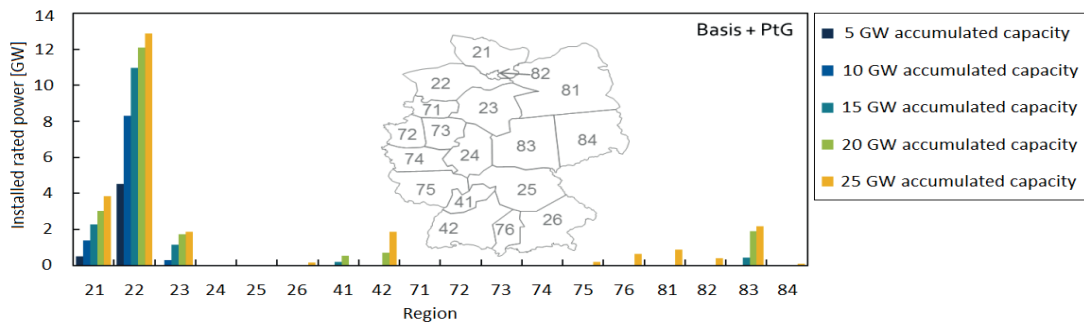


Figure 1.6: Spatial distribution of PtG plants for a 85%-RE scenario in Germany [5][9].

Furthermore, Jentsch et al.[9] reported that a PtG installed capacity⁶ of 25 GW would be able to store the electricity surpluses that arise in the 85%-RE scenario, an increase of the PtG capacity would contribute to the integration of more RE into the electric system, reduce the plants operating hours and the costs of the electric system as well as its annual associated CO_{2eq} emissions.

1.3 Electrolysis

1.3.1 Alkaline electrolysis

It is the most mature technology and dominates the market nowadays, this technology has been implemented for more than 100 years at industrial scale. Potassium hydroxide (KOH) with a concentration between 20 - 40 wt% [18] acts as basic electrolyte. Alkaline electrolyzers operate in a temperature range which spans between 49.9 - 79.9 °C [18], pressures between atmospheric and 15 bar [19], current densities in the range of 300 - 500 mA/cm² [19] and cell voltages between 1.8 - 2.4 V [18]. Alkaline electrolyzers can produce an hourly amount of H₂ between 1 - 760 Nm³ [19] and have a specific electrical energy consumption for systems that produce more than 10 Nm³ from 4.1 - 6.0 kWh/Nm³ which corresponds to an energy efficiency⁷ of 60 - 88%. Hydrogen and oxygen gas purity in alkaline electrolyzers ranges between 99.8 - 99.9% and 99.3 - 99.8% [18] respectively. It is important to note that

⁶It was assumed that only PtG technologies are able to store the system electricity surpluses for a long term [9].

⁷Calculated efficiency based on HHV of H₂

gas purity decreases if the electrolyser is operated at part load, consequently the lower limit at which alkaline electrolysers are operated is 20% of their rated power [18][19]. Alkaline electrolysers must have a quick start-up, shut-down processes, low energy consumption in standby mode, the ability of being slightly overloaded, operated at high pressures and dynamically if they are going to be integrated into the energy sector. Smolinka et al. [18] reported that due to the complexity of the system design (peripheral components and long respond times), dynamic operation is not achievable with alkaline electrolysers. However, it has been proven that new alkaline electrolysers can operate dynamically as long as some adaptations e.g. the implementation of a proper power electronic system. Furthermore, a constant warm-up mechanism is required in order to keep the operating temperature of the electrolyser in standby mode [18].

1.3.2 Polymer Electrolyte Membrane electrolysis

Polymer electrolyte membrane (PEM) electrolysers consist of two sections (anode and cathode) separated by a membrane that acts as electrolyte and is assembled in between two conducting plates [18], the membrane conducts protons and is coated with electrodes which contain a catalyst. Unlike alkaline electrolysers, the electrolyte of PEM electrolysers is solid (normally perfluorosulfonic acid polymer is used), it shows high thermal, chemical and mechanical stability as well as low permeability to hydrogen and oxygen [18]. However, the disadvantages of this type of membrane are its short lifespan, high production costs and loss of proton conduction. The efficiency of PEM and alkaline electrolysers are in the same range (60 - 88%), the electric energy demand of PEM electrolysers for systems that produce more than 10 Nm³/h can be reduced to values less than 6.0 kWh/Nm³ [18]. It is important to note that PEM electrolysers are expected to have higher efficiencies in the future [18]. PEM electrolysers have a shorter lifespan compared to alkaline electrolysers, the membrane degradation is the most common problem leading to poorer gas quality and leakages [18]. Regarding the integration of PEM electrolysers into a RE-based energy systems, technical features such as high power density, broad part-load range (5 - 100%), overload capability, short start-up process and short time responses represent some advantages over alkaline electrolysers [18]. The main issue when operating PEM electrolysers at part load is the migration of hydrogen through the membrane to the oxygen compartment.

1.3.3 Solid oxide electrolysis

Solid oxide electrolysis becomes an interesting application if waste heat is available (geothermal, nuclear, solar). The main disadvantages of this technology are its long start-up time, limitations regarding its flexible operation and materials. This type of electrolyser works at temperatures around 700 °C, pressures up to 50 bar, theoretical cell voltages of 1.48 V and efficiencies higher than 90% [19]. Since solid oxide electrolysers operate at high temperatures, decomposition of CO₂ is also possible thus the production of CH₄ from a mixture of H₂ and CO₂ can be achieved if a catalyst is placed downstream [18]. The lifespan of solid oxide electrolysers is relatively low, the longest lifespan was reported by Tietz et al. [20], in this case the stack degenerated faster than other components leading to an operating time of 9000 h. Additionally, an increase in the current density led to shorter lifespans [18][20].

Regarding the integration of solid oxide electrolysers with RE sources, the following issues have to be taken into account: the operation of solid oxide electrolysers under load variations leads to changes of the Joule heat and consequently temperature gradients along the stack i.e. material stresses which shorten the lifespan of the electrolyser. Therefore start-up and shut-down processes must be carried out slowly, this is only achievable if the electrolyser temperature is not lower than 600 °C during the standby operating mode [18]. Slow shut-down and start-up processes as well as material stresses due to load variations do not represent an advantage if solid oxide electrolysis are going to be integrated to RES. *Table 1.1* compares the electrolyser technologies discussed in this section and lists the advantages and drawbacks of each technology.

Table 1.1: Comparison of the electrolyser technologies [18][19][21].

	Electrolyser technology		
	AE	PEME	SOE
Operating temperature (°C)	50 - 80	50 - 70	700 - 1000
Operating pressure (bar)	1 - 150	<500	<25
Efficiency (%)	60 - 88	60 - 88	>90
Hydrogen production (Nm ³ /h)	<760	<450	<5
Specific electrical consumption (kWh/Nm ³)	4.1 - 6.0	<6.0	<5
Advantages	Maturity, durability, robustness, availability for large scales	Wide range of part- load operation and flexible operation	Reduction of the electrical consumption, integration of waste heat
Drawbacks	Limited part- load operation, slow start-up process, high corrosion	Safety issues caused by H ₂ at the anode	High degradation rate of materials, low hydrogen production

1.4 Methanation

The methanation is the chemical process of reducing carbon dioxide or carbon monoxide to methane. There are two types of methanation, the biologic methanation whereby methane is produced by microorganisms as a product of their metabolic pathways and the catalytic methanation which takes place in the presence of inorganic metal-based catalysts [22].

Methanation processes have been coupled to ammonia plants in the past to eliminate small CO traces in H₂ rich feeding streams [22] and to produce CH₄ from coal, crude oil and naphtha [22], but recent interest for adapting the technology as a way to produce SNG has been growing due to the oil prices and other energy concerns. In this section the biologic methanation, the operating conditions and the technical characteristics for five approaches implemented by two German companies (*MicroEnergy GmbH and Krajetz GmbH*) are presented. Additionally, the catalytic methanation is also presented, operating conditions, technical aspects, challenges as well as different reactor concepts such as fixed-, fluidised-bed, column-bubble, honeycomb and micro-channel are discussed. Advantages and disadvantages between the biologic and the catalytic methanation are presented at the end of this section.

1.4.1 Biologic methanation

The Biologic methanation is the process which *figure 1.7* describes. This process takes place in a temperature range of 40 - 70 °C which means that the produced water is in liquid state leading to a reaction enthalpy ΔH^0 of -253 kJ/mol [23][24]. The first reports about biologic methanation date back to the beginning of the twentieth century. Back in the 1930s some scientists investigated its metabolisms [25][26][27][28]. Further work was pursued where the effect of the temperature, agitation and residence times on the CH₄ production was analysed. For example the work reported by Guiot et al. [29] states that the methane production was improved when the temperature of the medium was increased from 35 to 60 °C. Although 90% conversion of H₂ has been reported, residence times from 0.7 - 2h, stirring of 100 - 400 rpm were required [30], mass transfer limitations due to low solubility of H₂ in the medium was reported as well by Wise et al. [31], Barik et al. [32], Klasson et al. [30], Guiot et al. [29].

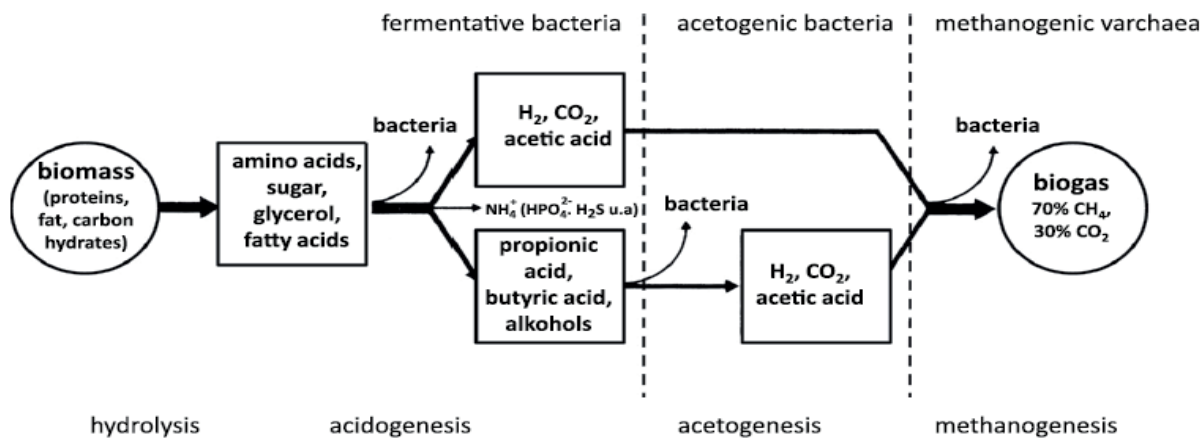
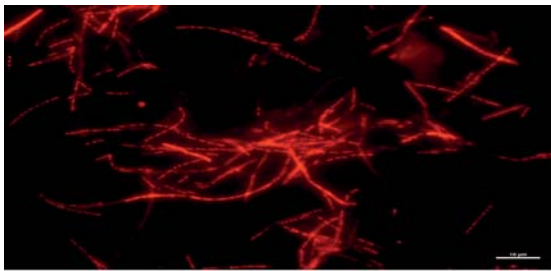
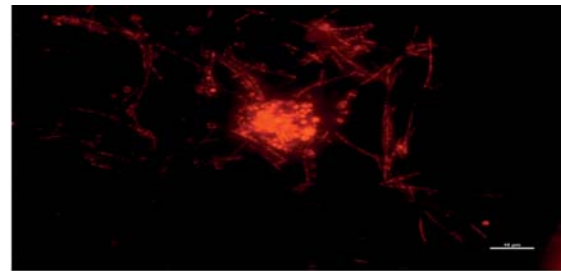


Figure 1.7: Anaerobic degradation of organic biomass to methane [33].

Moreover, it has been reported that some types of bacteria such as *Methanothermobacter thermautotrophicus*, *Methanococcus thermolithotrophicus* and *Methanothermobacter marburgensis* are able to produce more methane compared to other types bacteria [34][35][36]. The adequate pH for these bacteria spans from 6.9 - 7.8 [29], some studies where real gas such as biogas and flue gas were implemented, reported good production of methane by *Methanothermobacter marburgensis* and *thermautotrophicus* in the presence of sulphuric components such as H₂S [37][38]. *Figure 1.8* shows two types of bacteria which have been inoculated into a methanation reactor.



(a) Archaea spp.



(b) Methanosaeta spp.

Figure 1.8: Methanogenic bacteria [33].

Regarding the reactor technology, mostly biologic methanation experiments have been carried out in *continuous stirred-tank reactors* (CSTR), where a homogeneous distribution of the substrate is reached by stirring frequencies of 300 - 1200 RPM [24][30][29][39][36]. Thus, if it is considered that the electricity demand of the stirrer is proportional to $f^3 d^5$ where f stands for the frequency and d for the diameter, it is reasonable to state that

for stirrers with large diameters and high operating frequencies a considerable electricity demand is to be expected [24]. Other authors have reported an improvement in the mass transfer coefficient of H₂ by using a porous diffuser as gas distributor in CSTR [40]. An interesting approach where biomass was immobilised in fixed-bed reactors was studied by Vega et al. [41] and Klasson et al. [42][43]. The studies reported an improvement in the conversion as well as a decrease in the energy demand. There are some companies in Germany which have researched different plant concepts regarding the integration of biologic methanation and existing biogas facilities using as substrate organic raw material from the agricultural and forestry industry (*approach i*) or biowaste (*approach ii*), in this case H₂ is fed into a biogas fermenter containing biomass where the biologic methanation takes place [24]. At *MicrobEnergy GmbH* and *Krajete GmbH* two other approaches have been researched, in both approaches biogas is separated from the biologic methanation stage which in these two cases consists in a pure and special bacterial culture. For the *approach iii*, biogas is used as reacting gas at the methanation stage together with H₂, whilst for the *approach iv*, biogas is first upgraded and then the CO₂ which is separated by the upgrade unit, reacts with H₂ at the methanation stage [24]. Furthermore, an alternative (*approach v*) using CO₂-rich gases from industry processes and pure bacterial cultures has been researched at *Krajete GmbH*.

Regarding the capacity of the plants, *approaches i-iv* were implemented in a range from 1, 2.5 and 5 MW_{th}⁸ whereas a plant of 110 MW_{th}⁸ implementing *approach v* was built up, these were operated for a minimum of 1200 and a maximum of 8400 full load hours [24]. The biologic methanation unit for the *approaches i - iv* was operated at 16 bar; the process in *approach v* was carried out at 70 bar. All outlet gas streams contained a volumetric percentage of CH₄ greater than 96%, the operating temperature in all cases was 20 °C [24]. Moreover, the efficiency of a PtG plant with a biological methanation process step can be defined as follows:

$$\eta = \frac{P_{CH_4}}{P_{el}} = \eta_{electrolysis} \eta_{bio-meth} \quad (1.1)$$

Considering the approaches mentioned above, the efficiency of a PtG plant spans between 53% - 58%, the lower value considers the electricity demand for the electrolyser as well as the stirrer in the reactor. Furthermore, if the heat of reaction (biologic methanation step) is used to heat up the biogas fermenter, the overall efficiency increases up to 69% [24].

⁸Corresponds to the calorific value of the gas produced after the biologic methanation step and it was adjusted in order to integrate the biogas plant

1.4.2 Catalytic methanation

Unlike the biological methanation where the process takes place in the presence of microorganisms, the catalytic methanation takes place in the presence of inorganic catalysts such as *nickel-, ruthenium-, cobalt-, iron-, platinum-, rhodium-based*. *Sabatier and Senderens* were the first scientists who researched this type of methanation [28]. The studies showed nickel as a very efficient catalyst for the methanation reaction [28]. The catalysts are required in order to accelerate the reaction stated in *equation* (1.2) which is otherwise relatively slow in order to meet commercial targets [28].



Equation (1.2) is a reversible reaction which can be broken down as follows:



The reaction takes place within a temperature range of 250 - 500 °C [44], reactant conversion is favoured at low operating temperatures and high pressures [45][22]. The exothermicity of the reaction represents a challenge to prevent over heating of the catalyst and hence its deactivation [28]. Regarding the chemical mechanism between the substrate and the catalyst, two schemes have been proposed [28]. On the one hand, Medsford [46] suggests that the synthesis of CH₄ takes place without CO as intermediate. On the other hand, Bahr [47] states in his work that the synthesis of CH₄ takes place with CO as intermediate which was consistent with some studies in which ruthenium and iron catalysts were implemented [28]. Apart from reaction 1.3 and 1.4, the Boudouard reaction, CO and CO₂ reduction, methane pyrolysis, alkane and alkene formation may take place in parallel [48].

1.4.2.1 Conventional reactor concepts

In the 1960s, the importance of natural gas as energy carrier in the united states increased⁹, this raised concerns about possible shortages and the government started funding projects to research new ways to produce natural gas e.g. through methanation of coal from power plants [22]. Furthermore, due to the oil crisis in the 1970s efforts were intensified and other

⁹In the 1950s approximately 13 % of the primary energy consumption was supplied with natural gas. This number increased to 30% in the 1960s and 1970s [22]

countries such as Great Britain and Germany started funding projects and developing technologies for such purpose as well. This section presents the reactor technologies for producing methane which were developed back then.

1.4.2.1.1 Fixed-bed reactors

Fixed bed reactors contain packed catalyst in a static bed or in pellet form [49]. The Lurgi coal gasification process that consists of two adiabatic fixed-bed reactors which have an internal recycle in between was used in two pilot plants, one operated in Sasolburg (South Africa) and the other one in Schwechat (Austria) [22]. The pilot plant that operated in Sasolburg used a syngas side-stream from the Fisher-Tropsch unit, whilst in the second pilot plant, the syngas from naphtha was converted to CH₄. Both plants were operated for 1.5 years with two different nickel-based catalysts, the first catalyst showed deactivation relatively fast, whilst the second catalyst was tested for 4000 h with a feed-gas flow rate of 18.2 Nm³/h and reached equilibrium temperature after 32% of the bed length [22]. The first fixed-bed reactor in this case was operated with an inlet temperature of 300 °C, the outlet temperature was 450 °C; the second fixed-bed reactor was operated with an inlet temperature of 260 °C, outlet temperature of 315 °C. *Table 1.2* lists the operating conditions for the reactors as well as the gas compositions.

Table 1.2: Operation parameters and gas composition in the pilot plant of the Lurgi process [22].

	Feedgas	Fixed bed reactor R1		Fixed bed reactor R2	
		Inlet	Outlet	Inlet	Outlet
Temp.(°C)	270	300	450	260	315
Gas flow rate (wet),(Nm ³ /h)	18.2	96.0	89.6	8.2	7.9
H ₂	60.1	21.3	7.7	7.7	0.7
CO	15.5	4.3	0.4	0.4	0.05
CO ₂	13.0	19.3	21.5	21.5	21.3
CH ₄	10.3	53.3	68.4	68.4	75.9
C ⁺ ₂	0.2	0.1	0.05	0.05	0.05
N ₂	0.9	1.7	2.0	2.0	2.0

Moreover, the effect of the sulphur content in the feed-gas was also investigated. The data obtained suggested a decrease in the conversion when the concentration of hydrogen sulphide (H_2S) was kept between 0.02 - 4.0 mg/ Nm^3 , the lower value led to a decrease in the conversion from 0.5 - 0.46 after 6.3% of the total catalyst bed whereas the higher value led to a conversion decrease from 1.0 - 0.78 after the 23.8% of the total catalyst bed. Eisenlohr et al. [50] reported in his work that an operation of 150 h with a hydrogen sulphide concentration of 4.0 mg/ Nm^3 in the feed-gas corresponds to one year operation when a concentration of 0.08 mg/ Nm^3 total sulphur is contained in the feed-gas. *Figure 1.9* shows a graphical representation of the Lurgi coal gasification process.

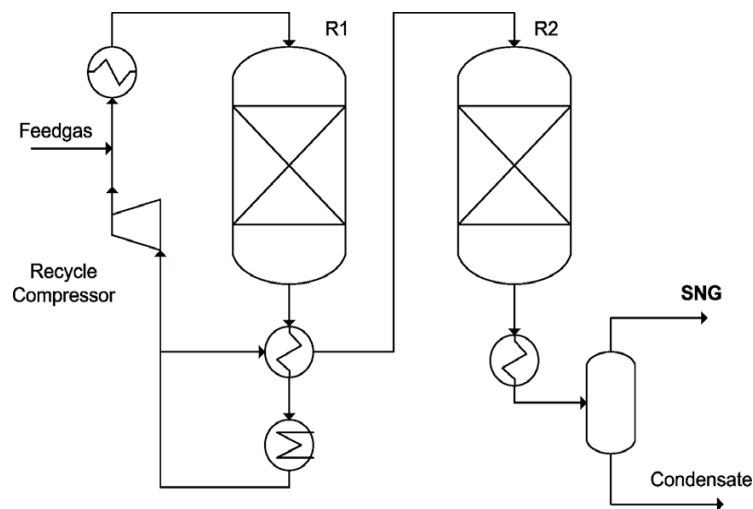


Figure 1.9: Lurgi coal gasification process [22][51].

Despite the efforts and the construction of pilot and demo plants during this period of time, the only plant which operated commercially was *the Great Plains Synfuels Plant* in North Dakota (United States). This plant consists of 14 Lurgi Mark IV fixed-bed gasifiers, a shift conversion unit, a rectisol unit where carbon dioxide and sulphur removal takes place, a methanation unit (fixed-bed reactors) and a drying-compression unit. The plant was designed to produce up to 4.8 millions m^3 CH_4 per day [51].

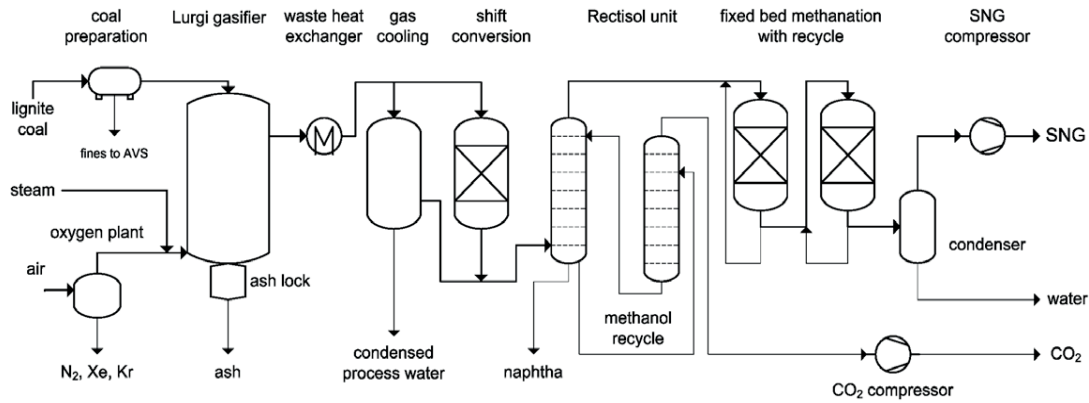


Figure 1.10: Graphical representation of the Great Plains Synfuels Plant [22][51].

From 1970 to 1980 the *Kernforschungszentrum Jülich*, *Rheinische Braunkohlewerke* and *Haldor Topsøe* started to investigate the steam reforming of methane and the methanation of synthesis gas as a way to store and distribute heat produced by nuclear reactors [52]. The methanation process was investigated in a bench-scale unit called ADAM I which consisted of three adiabatic fixed-bed reactors [22]. Additionally for ADAM I, the TREMP concept (Topsøe’s Recycle Energy efficient Methanation Process) which is a way to use the reaction heat to produce high pressure superheated steam was implemented. The catalyst was tested at 600 °C for more than 8000 h, the gas compositions and operating conditions are shown in *table 1.3*.

Table 1.3: Gas composition of ADAM I [52][22].

	Feed	R1 Inlet	R1 Exit	R2 Exit	R3 Exit	SNG
Temp. (°C)		300	604	451	303	23
Press. (bar)	27.3	27.2	27.1	27.05	27.0	27.0
Gas (Nm ³ /h)	535	1416	1255	348	334	119
Gas composition (vol.%)						
H ₂	65.45	36.88	20.96	8.10	1.77	3.11
CO	9.84	4.28	1.17	0.00	0.00	0.00
CO ₂	8.96	6.13	4.46	2.07	0.95	1.67
CH ₄	11.30	28.12	37.44	44.36	47.28	82.95
H ₂ O	-	19.19	29.82	38.84	43.06	0.10
N ₂	4.4	5.41	6.15	6.64	6.93	12.16

In 1972 the first demo plant worldwide which completed the entire process chain from coal to CH_4 was built up in Scotland by the British Gas Corporation and the Continental Oil Company (Conocophilips). The demo plant used fixed-bed reactors which were operated adiabatically with a gas recycle in between. The plant produced 59 millions m^3 per day CH_4 which were fed into the natural gas grid. Another approach which use fixed-bed reactors in series and cooling between them was proposed by the Ralph M. Parsons Company (United States), the outlet volumetric percentage reached by the last reactor was 43% [22].

The *British Gas Corporation* developed the HICOM process which combines the shift and methanation reaction, thereby an efficiency of 70% from coal to methane was proposed by Ensell et al. [53]. The gas produced by the coal gasifier is cooled down, desulphurised and saturated before it is fed into the methanation unit. Subsequently, the product gas is purified (removal of CO_2). The product gas of the main methanation unit is split into two streams, part of the product gas is recycled so that temperature control of the reactors is achieved and the remaining gas is fed into one of many low temperature fixed-bed reactors hence traces of CO and H_2 can be further converted to CH_4 [22]. *Figure 1.11* depicts a simplified process flow diagram of the HICOM approach.

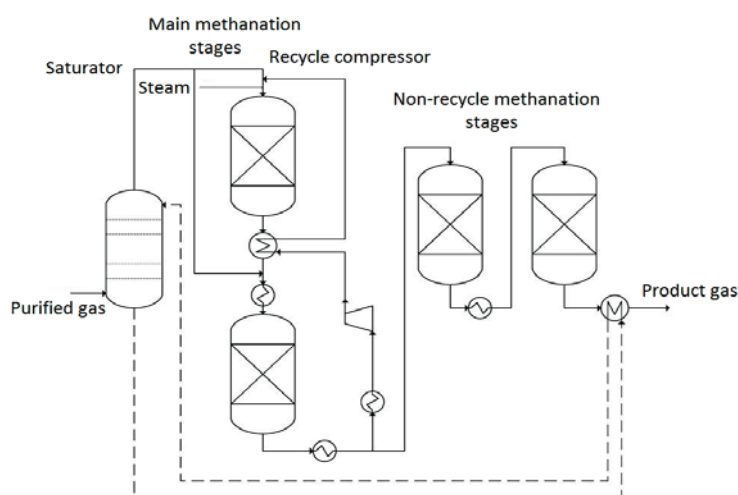


Figure 1.11: Simplified HICOM process flow diagram [22][53].

Additionally, during the 1970s the German company Linde AG developed an isothermal fixed-bed reactor with indirect heat exchange. The reactor was designed to produce steam using the heat of the methanation reaction. Moreover, part of the steam was planned to be fed into the syngas mixture to avoid carbon deposition [22]. The syngas mixture can

1. Theoretical background and technological state of the art

be fed into an isothermal and adiabatic methanation reactor, part of the gas produced by the isothermal reactor is fed into the adiabatic reactor to increase the amount of CH_4 . Finally, both product gases are mixed, cooled and dried [22]. *Figure 1.12* shows an adapted graphical representation of the SNG process and the isothermal reactor proposed by Linde.

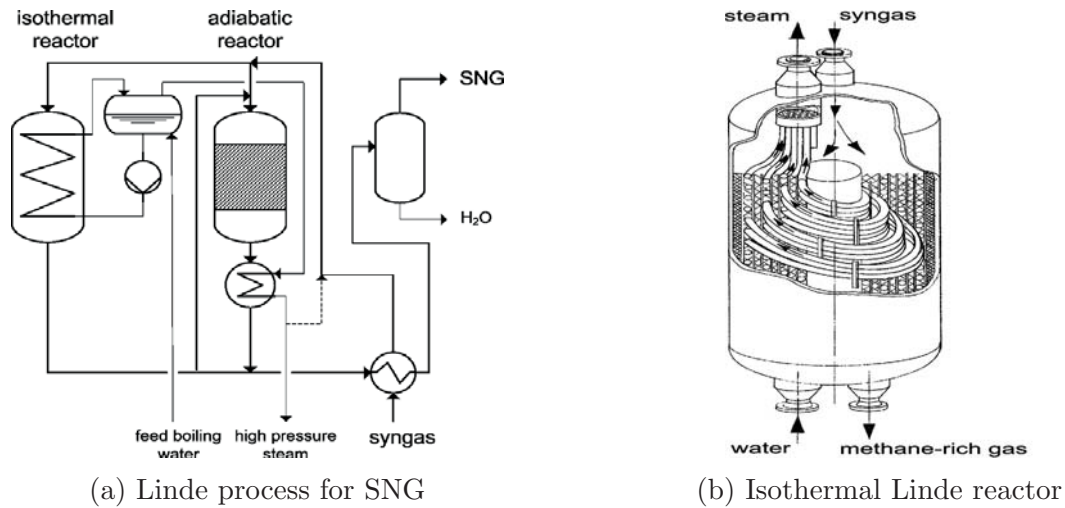


Figure 1.12: Linde process for SNG and isothermal reactor [22].

The RMP process was proposed by the Ralph M. Parsons company in the united state. The process consists of high temperature methanation without gas recycle and no separate shift conversion step. 4 to 6 adiabatic fixed-bed reactors with gas cooling in between are used for methanation purposes, steam is fed into the first reactor whilst the syngas can be fed with different distribution ratios into the first four reactors [22]. Pressures between 4.5 and 77 bar and temperatures between 315 and 538 °C are reported in the literature [22].

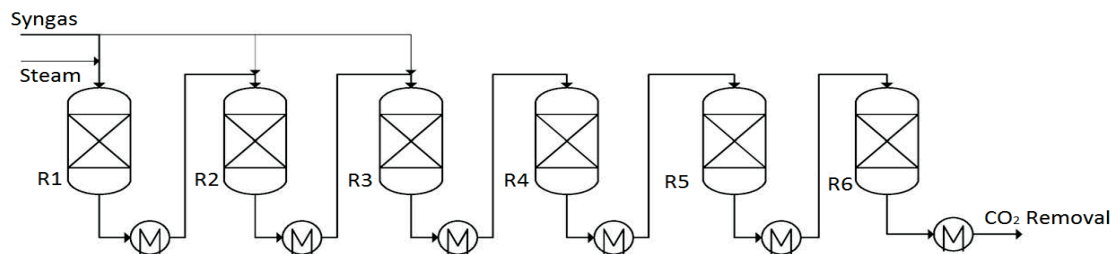


Figure 1.13: Fixed-bed RMP process flow diagram [22][54].

Figure 1.13 depicts the RMP process. Additionally, table 1.4 lists the operation conditions and gas composition in the different reactors.

Table 1.4: Dry gas composition of the RMP process at 27 bar [54][22].

	Syngas	R1	R2	R3	R4	R5	R6
Temp. (°C)(inlet)	-	482	538	538	538	316	260
Temp. (°C)(outlet)	-	773	779	773	717	604	471
Press. (bar)(outlet)	27.3	26.7	25.6	24.6	23.6	22.6	21.5
Syngas (vol.%(inlet)	-	40	30	30	-	-	-
Steam/gas (inlet)	1.20	0.88	0.56	0.43	0.50	0.65	0.83
Dry gas composition (vol.% at the outlet)							
H ₂	49.80	53.53	48.07	43.09	36.90	22.86	9.29
CO	49.80	13.97	18.46	20.63	15.25	5.64	0.87
CO ₂	0.10	25.80	24.04	23.64	29.21	39.90	46.84
CH ₄	0.30	5.70	9.43	12.64	18.64	31.60	43.00

Another process which was designed using fixed-bed reactors is the ICI/Koppers process. ICI stands for Imperial Chemical Industries in Great Britain. The aim of the process was the production of SNG from a Koppers-Totzek coal gasifier using a Ni-based catalyst which showed good activity and selectivity for a 1500 h test run. Three adiabatic reactors were connected in series, the temperature was varied between 300 - 729 °C and the vol.% composition of CH₄ obtained at the outlet of the third reactor was 29.1% (dry gas).

1.4.2.1.2 Fluidised-bed reactors

Unlike fixed-bed reactors the catalyst in fluidised-bed reactors is contained within a fluid phase which can be from an inert liquid to particles suspended. [49]. The United States Department of the Interior (former Bureau of Mines) carried out a project which aim was the production of high quality CH₄ through coal gasification and methanation [55]. Two fluidised-bed reactors (one with multiples feed inlets and one with three gas inlets at the reactor bottom) and one fixed-bed reactor were operated for more than 1000 h. For the experimental tests a Raney-nickel and iron based catalyst were used (90 - 120 cm catalyst bed height), both of them had a particle diameter from 63 - 180 μm, an operating temper-

1. Theoretical background and technological state of the art

ature from 200 - 400 °C and an operating pressure up to 20.7 bar [22]. Good temperature control was reported in the fluidised-bed reactor with multiple feed inlets, the operation with the iron based catalyst did not meet the quality necessary to feed the product gas into the grid (the conversion of H₂ and CO was lower than 80% and C₂₊, C₃₊ hydrocarbons were formed). The nickel based catalyst on the other hand showed to be catalytically active enough to ensure the desired gas quality. The fluidised-bed reactor with multiple feed inlets was operated for 1120 h at temperatures from 370 - 395 °C showing a conversion of H₂ and CO greater than 95% [22]; the catalyst was regenerated after 492 h. The goal of the Bi-Gas project also was the production of high quality CH₄ from coal. For this project, a fluidised-bed reactor with two feed inlets was implemented, the methanation took place in a temperature range of 430 - 530 °C and a pressure range of 69 - 87 bar. The composition of the reactant gas was 59 vol.% H₂, 19 vol.% CO, 20 vol.% CH₄ and some traces of CO₂, H₂O as well as N₂. The reported CO conversion was between 70 to 95% [22][56]. *Figure 1.14a* depicts the fluidised-bed reactor with multiples feed inlets used for the department of the Interior of the United States as well as the fluidised-bed reactor used in the Bi-Gas project.

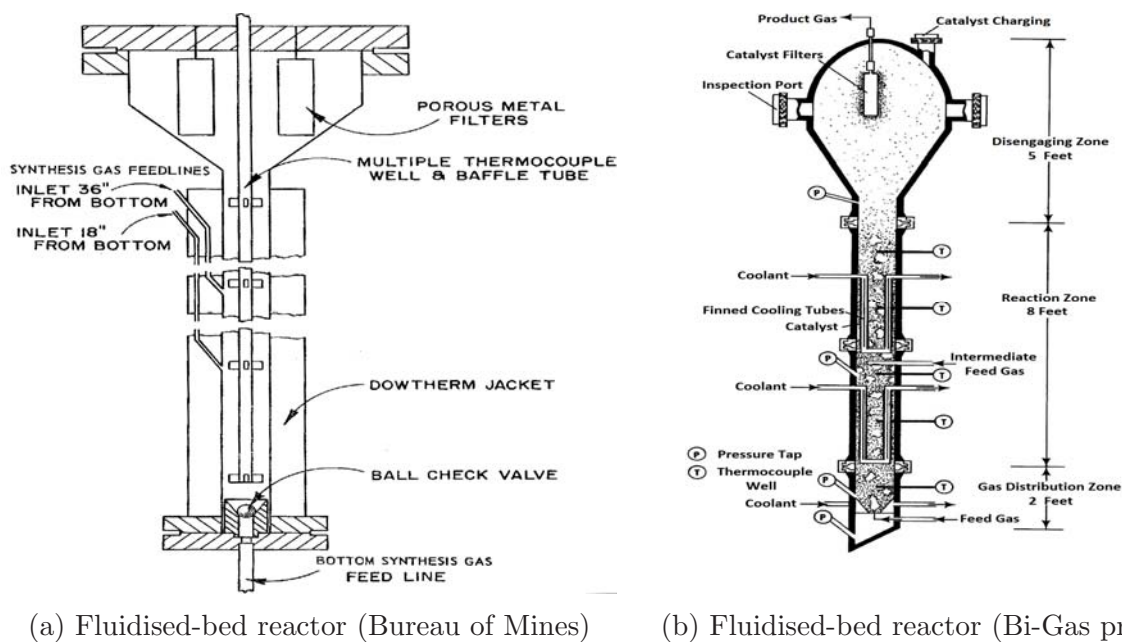


Figure 1.14: Fluidised bed reactors [22][57][58].

Additionally, from 1975 - 1986 the *university of Karlsruhe* and *Thyssengas GmbH* carried out some research on the production of SNG from coal gasification implementing fluidised-bed reactors (*Comflux process*).

A pilot plant was commissioned and operated by *Didier Engineering GmbH* from 1977 - 1981. The operating conditions of the Thyssengas pilot plant are listed in *table 1.5*.

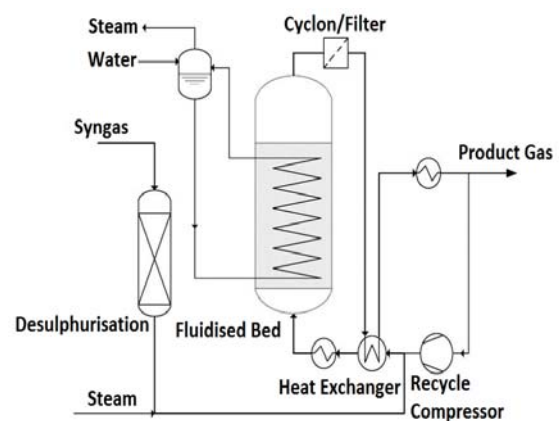
Table 1.5: Operating conditions of the Thyssengas pilot plant [22].

Temperature (°C)	300 - 500
Pressure (bar)	20 - 60
H ₂ /CO ratio	Up to 4
Recycle/feed ratio	Up to 2
Gas velocity u (m/s)	0.05 - 0.2
Bed diameter (m)	0.4
Bed Height (m)	2 - 4
Particle size (μm)	50 - 250
Catalyst mass (kg)	200

Furthermore, a demo plant (2000 Nm³_{SNG}/h) was operated in Oberhausen (Germany). During this project the kinetics of the reaction, deactivation mechanisms, the attrition resistance of the catalyst, the effects of sulphur and carbon deposition on nickel catalysts were investigated. The results showed that for a commercial scale, the avoidance of some units such as the shift and the compression of the recycled product gas can lead to some reduction of the operational and investments costs (up to 10% compared with plants using fixed-bed reactors) [22]. *Figure 1.15* depicts the pilot plant operated by *Didier Engineering GmbH* and shows a graphical representation of the Comflux process.



(a) Comflux pilot plant



(b) Comflux process flow diagram

Figure 1.15: Comflux pilot plant and process flow diagram [22][59][60].

1.4.2.2 Innovative reactor concepts

Conventional reactor concepts were mostly developed for the production of SNG from large scale coal plants which were operated under certain conditions. The integration of these reactors for the production of methane in PtG plants poses technical limitations such as low dynamic operation and poor heat exchange properties. Therefore, new reactor concepts with high dynamic, good heat transfer properties which can be deployed for decentralised power plants have to be developed. This section presents alternative reactor concepts for the production of methane in PtG plants.

1.4.2.2.1 Three-phase reactors

Three-phase reactors or slurry bubble column reactors consist of a liquid phase which contains the catalyst suspended in small particles (between 5 - 150 μm ; a loading up to 50% vol. [61]) and a gas phase which is distributed through spargers leading to bubbles formation in the liquid phase, the latter can have a counter- or co-current configuration with respect to the gas phase [62]. According to Shaikh [62], slurry bubble column reactors have good heat and mass transfer, low operating and maintenance costs but one of the main disadvantages is the back-mixing of the liquid phase which leads to a decrease in the conversion. This type of reactor has been used in the chemical, biochemical, pharmaceutical and petrochemical industry for the partial oxidation of ethylene to acetaldehyde, the liquid-phase methanol synthesis, Fischer-Tropsch synthesis, cultivation of bacteria and mold fungi, production of animal cell culture, treatment of sewage among others applications [62]. The conversion and selectivity of slurry bubble column reactors can be affected by the hydrodynamics, therefore a proper design (sparger; reactor geometry) and operation (temperature; pressure; liquid load; catalyst load) is required. Another important aspect of slurry bubble column reactors is the flow regime. It is expected that different hydrodynamic behaviours arise with different flow regimes which can lead to different mixing as well as different heat and mass transfer properties in the reactor, specially at industrial scales. Four types of flow regimes have been identified in slurry bubble column reactors, homogeneous (bubbly), heterogeneous (churn-turbulent), slug and annular flow [62]. The homogeneous flow regime takes place at low - moderate superficial gas velocities¹⁰, in the homogeneous flow the bubble size is uniform, small and depends on the gas distribution

¹⁰Moderate superficial gas velocities is a definition used when working with multiphase flows and porous media. It refers to the hypothetical flow velocity assuming that the fluid of interest is the only one flowing along the cross sectional area.

as well as the physical properties of the liquid. The heterogeneous flow takes place at high superficial velocities, the presence of small and large bubbles are normal for this type of flow. Moreover, liquid circulation in the reactor occurs for this type of flow regime due to the non-uniformity of the gas hold-up distribution in the radial direction [62]. In his work Shaikh [62] studied the hydrodynamic behaviour of a slurry bubble column reactor using non-invasive techniques which can be implemented at industrial scales. The reactor consisted of a stainless steel column with an inner diameter of 0.162 m, a height of 2.5 m. The gas was fed into the reactor with a pressure of 14.5 bar and a maximal flow rate of 8.8 m³/h. Two operating pressures (1 and 10 bar) were tested, different superficial velocities as well as solids loading were also varied. *Figure 1.16* depicts the slurry bubble reactor used by Shaikh in his work.

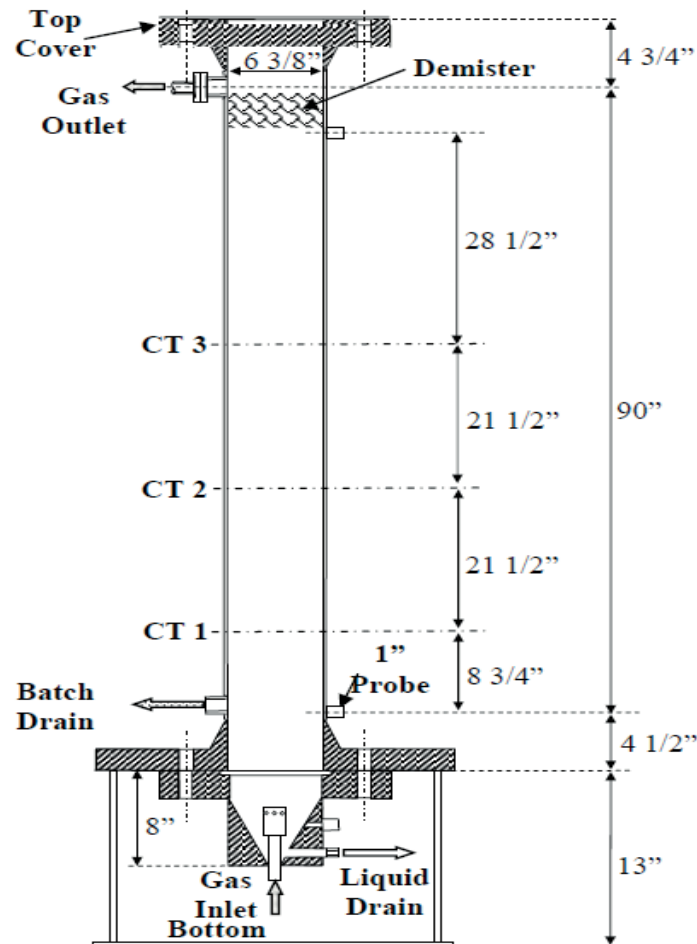


Figure 1.16: Slurry bubble reactor used by Shaikh [62].

On the one hand, the results suggested that the gas hold-up decreases with an increase in the solids loading because the pseudo-viscosity of the liquid phase increases which contributes to the coalescence of bubbles and this leads to the formation of large bubbles. Thus a transition between the flow regimes occurs at lower superficial gas velocities. On the other hand an increase in pressure led to an increase of the gas hold-up at constant superficial gas velocity. Wilkinson et al. [63] reported that higher gas densities produced by an increase in pressure does not allow the formation of large bubbles and therefore smaller bubbles flow through the liquid phase. It is also important to remark that Shaikh [62] reported that when testing two different liquid phases (water and Therminol LT) a higher gas hold-up was observed at the bubbly flow regime when the liquid phase was water, whereas when Therminol LT was used as liquid phase, the higher gas hold-up was achieved at churn-turbulent flow regime. Shaikh reported that the hydrodynamic conditions at which the transition between different flow regimes depends on the the superficial gas velocity, column diameter, gas phase properties, liquid phase properties, distributor design and solid loading. *Chem System Inc.* in the United States developed a slurry bubble column reactor which aim was to remove the heat of reaction more efficiently. In this case the syngas was produced by a coal gasifier and then fed into the three-phase methanation reactor. After the methanation took place, the product gas was purified through a liquid phase and a product gas separator unit, the experiments were carried out using different types of nickel-based catalysts and the results suggested low conversion and loss of catalyst [22]. The liquid temperature ranged between 260 - 360 °C, pressure between 20.7 - 69 bar and the catalyst size between 0.79 - 4.76 mm. The reactor had a diameter of 2.0, a height of 1.2 m and the ratio H_2/CO was varied between 1 - 10. *Figure 1.17* shows a graphical representation of the three-phase methanation plant proposed by Chem System Inc.

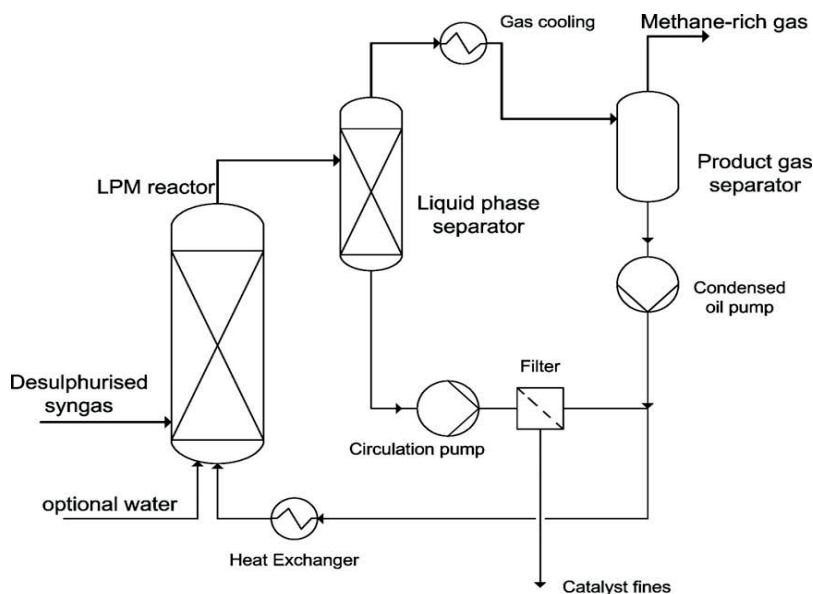


Figure 1.17: Three-phase methanation (Chem System Inc.) [22][64].

At Karlsruhe Institute of Technology (KIT), there have also been some research projects on three-phase methanation. Götz [65] in his work focused on the modelling of a three-phase reactor by considering the different mass transfer processes which take place in the different phases. Götz considered the transport from the gas phase to the gas-liquid interface, transport from the gas-liquid interface to the liquid bulk, transport from the liquid bulk to the catalyst outer surface followed by the diffusion, adsorption and chemical reaction of the gas molecules inside the catalyst pores; once the reaction ends, the product desorption and transport to the gas phase takes place. His work also stated that an increase in the gas density decreases bubble coalescence which means that the transition between the flow regimes (homogeneous to heterogeneous) occurs at higher superficial gas velocities. Moreover, the liquid phase should have thermal stability, low vapour pressure, low viscosity, low surface tension and good solubility with respect to the educt gas [65]. Hydrocarbons, silicon oils, perfluoropolyethers and ionic liquids are normally used in three-phase reactors as liquid phase. *Figure 1.18* shows a graphical representation of the bubble column reactor manufactured at KIT, the effect of the solids loading and gas velocity on the gas bubble size.

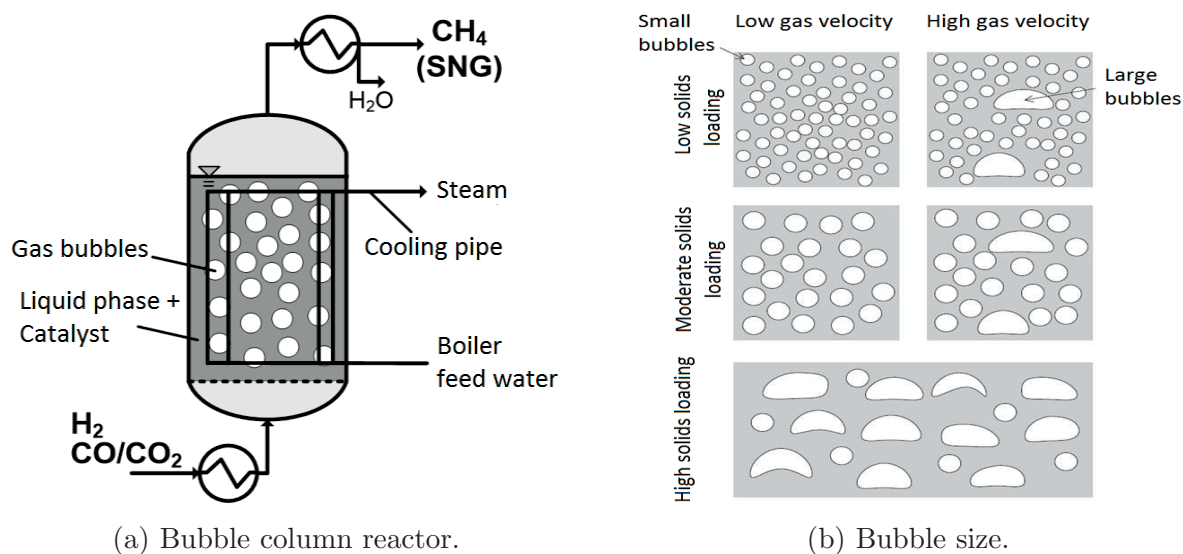


Figure 1.18: Three-phase methanation reactor (KIT) and the effect of the solids loading as well as the effect of the gas phase velocity on the bubble size [65].

Furthermore, Götz [65] carried out CO and CO₂ methanation experiments using four different fluids as liquid phase, the temperature was varied between 220 - 380 °C, the pressure between 1 - 20 bar, and a commercial nickel-based catalyst was implemented (NiKom2). The CO methanation results indicated that the mass transfer as well as the kinetics were positively influenced as the temperature increased, an increase in pressure led to better results which can be explained according to Götz as follows: with higher pressures the residence time of the gas, gas solubility and density increases. A CO conversion in the range of 20 - 90% was achieved [65]. Furthermore a comparison between the CO methanation carried out by Götz and other reactor concepts was discussed. Despite the low operating pressure in fluidised-bed reactors a production rate of CH₄ four times higher can be achieved. Mass transfer limitations between the gas and liquid phase, back-mixing in three-phase methanation reactors as well as higher operating temperature in the fluidised-bed may explain it. The CO₂ methanation experiments showed lower kinetics and therefore lower CO₂ conversion [65]. Decrease of the reaction rate due to mass transfer limitations between the gas and liquid phase can explain this results. A hyper-stoichiometric H₂/CO₂ ratio of 6.1 was required in to achieve conversions greater than 95%. Additionally, more research is required to find substances with adequate properties to be used as liquid phase in three-phase methanation reactors.

1.4.2.2.2 Honeycomb reactors

Another reactor concept that has been investigated for methanation purposes at (KIT) is the honeycomb reactor. Schollenberger [66] used a honeycomb reactor coated with a nickel-based catalyst in his work. The reactor consisted of a double-walled pipe with a 35 mm diameter, 50 mm length and 1465 m^{-1} specific surface. The wall temperature was held constant by using a heat transfer oil, the ratio H_2/CO_2 was varied between 1 - 15, the temperature between 220 - 300 °C, the pressure was kept constant at 8 bar, the volumetric percentage of H_2 , CO_2 , CH_4 , H_2O in the product gas varied between 43.7 - 83.9 %, 3.66 - 45.5 %, 14.4 - 28.6 % and 10 - 30 % respectively. The results suggested that the produced gas does not meet the requirements to be fed into the gas grid, Schollenberger proposed an upgrading unit downstream the reactor to remove the remaining CO_2 . Honeycomb reactors could represent an economic alternative to fixed-bed reactors due to the fact that honeycomb reactors have a pressure drop from 1 - 2 order of magnitudes lower than fixed-bed reactors considering same height and surface/volume ratio. However, more research is required regarding the optimisation and scaling. *Figure 1.19* depicts the structure of a honeycomb reactor developed at KIT.



Figure 1.19: Honeycomb reactor developed at KIT

1.4.2.2.3 Micro-channel reactors

The micro-channel reactor is the last type of reactor which is addressed in this doctoral thesis. Micro-channel reactors are made of small channels ($<1 \text{ mm}$ wide) where fluid

flows through. Enhanced heat transfer in micro-channel reactors has been reported, this property allows exothermic reactions to take place without hotspot formation. The reactor may be manufactured¹¹ to optimise slow reactions getting close to the thermodynamic equilibrium. For conventional reactor concepts, the improvement of the conversion for such reactions takes place by intermediate direct (cold gas, water injection) or indirect cooling (coolers switched between several stages of the reactor) [67]. Additionally, mass transfer is also enhanced in micro-channel reactors; according to Kolb et al. [67] in most cases the Sherwood number which is defined in equation (1.5) is equal to 3.66 for fully developed laminar flow.

$$Sh = \frac{k_g d_h}{D} \quad (1.5)$$

k_g denotes the mass transfer coefficient, d_h the hydraulic diameter of the channel and D the gas-phase diffusion coefficient. It can be inferred that higher values of k_g can be obtained for channel with smaller dimensions. Micro-channel reactors can be safely operated under explosive regime [67]. Another intrinsic advantage to these reactors is the easy scale-up due to the micro-channel "unit cell" which does not need to be changed [67], typical industrial applications of micro-channel reactors involve chemical processes e.g. cyclohexane dehydrogenation to benzene [68], organic synthesis reactions [69], Fischer-Tropsch synthesis [70], methanol steam reforming [71], among others. From the process point of view, plants which use micro-reactors present the following advantages compared to conventional reactors: size reduction, high flexibility, quicker response times, less investment and operating costs [72][73][74][75][76][77][78].

1.4.2.2.3.1 Chip-like micro-structured reactors

This type of reactor is manufactured resembling micro-electro-mechanical systems where non porous catalyst are applied, sensors and heaters can be coupled [79], short response times regarding heat exchange is observed in this type of reactor due to the thin walls. For instance, due to high conductivity, silicon membranes can be integrated in these reactors in order to enhance heat removal. Franz et al. [80] used such a reactor for ammonia oxidation, the results suggested improved heat removal and the reactor responded quickly to temperature changes (ca. 20ms) which according to Kolb et al. [67] allows dynamic operation. *Figure 1.20* depicts the structure of a micro-reactor developed by stacking up several

¹¹Heat-exchanging channels may be introduced in the reactor which allow the formation of temperature profiles[67].

platelets with sensors, the micro-reactor was used for the dehydrogenation of cyclohexane to benzene, the platelets are made of silicon and the channels are created through photo etching techniques. The micro-channels had a width of $500\ \mu\text{m}$, depth of $10\ \mu\text{m}$ and a length of $500\ \text{mm}$.

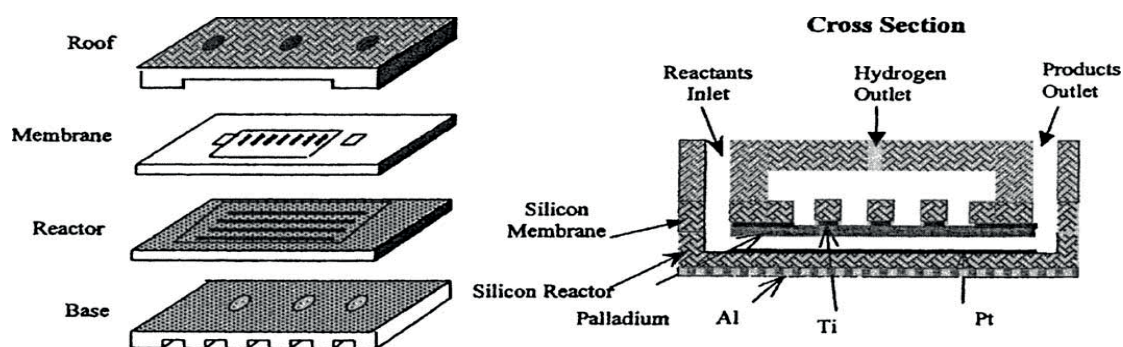


Figure 1.20: Membrane micro-reactor designed by Cui et al. [68].

Aleppe et al. [81] carried out some experiments for the dehydrogenation of methanol to formaldehyde in chip-like micro-reactors at temperatures greater than $600\ ^\circ\text{C}$, quick heating and cooling as well as short residence times in the micro-reactor were the main reasons for its implementation, in this case the channels had a length of $7.4\ \text{mm}$, $1.3\ \text{mm}$ width and $380\ \mu\text{m}$ depth. The system consisted of three sections heater/reactor/cooler, the heat exchange was achieved by a counter-flow configuration. *Figure 1.21* depicts the cross section of two micro-channel configurations used for this type of reactor. There has also been more research carried out on the field of *Chip-like micro-channel reactors* but further discussion is not presented in this dissertation, for more information refer to [67].

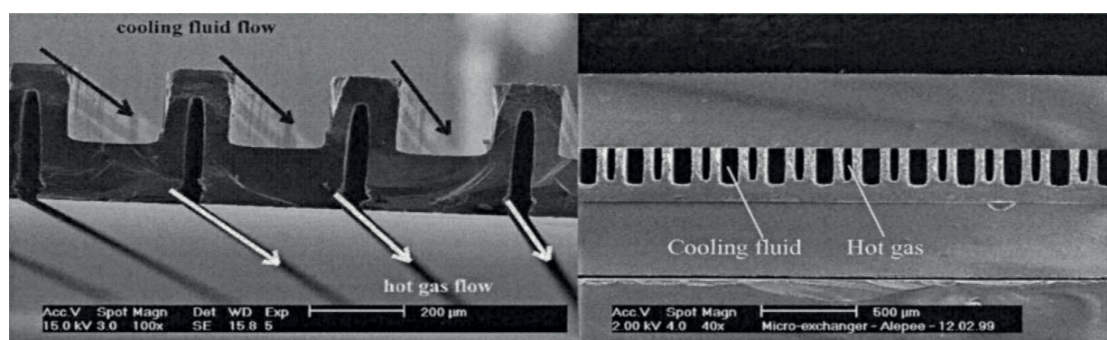


Figure 1.21: Cross section of the double-side (left) and one-sided (right) silicon heat exchangers manufactured by Aleppe et al. [81][67].

1.4.2.2.3.2 Stack-like reactors with external heating

The reactors developed by Wießmeier [82] and Kursawe et al. [83] are examples of *stack-like reactors with external heating*, the first reactor was used for the partial hydrogenation of cyclododecatrien to cyclododecene using Pd catalyst whereas the second reactor was used for benzene hydrogenation and ethylene oxide synthesis. The platelets used by Kursawe et al. [83] were made of either aluminium or aluminium alloys and each of them was designed to have 14 parallel micro-channels 300 μm wide and 700 μm deep. The micro-channels had a rough surface in order to contribute to the application of the catalyst, since it occurs through wash coating or another kind of coating for this type of reactor [67].

1.4.2.2.3.3 Stack-like reactors with integrated heat-exchanging capabilities

offer the possibility of higher heat transfer combined with the catalyst effectiveness provided by the micro-structures [67]. They can be divided into four categories: *Cross-flow heat exchangers/reactors*, *counter-flow heat exchangers/reactors*, *counter-flow heat exchangers/reactors for evaporation purposes*, *Ceramic micro-reactors for high temperature applications*. However, the fourth category is not discussed in this doctoral thesis.

Cross-flow heat exchangers/reactors

This type of reactor has been developed at *Forschungszentrum Karlsruhe*, catalyst can occur through wash coating or another type of coating. It is a modification of a micro-heat exchanger in which a catalyst is distributed on quadratic platelets. The platelets are stacked in a way that two adjacent parts have a 90° turn [67]. The reactor is designed in a way that allows two different flowing paths (reaction mixture and coolant), channel fabrication is achieved by mechanical surface cutting of the metal with ground-in mono-crystalline diamonds or ceramic micro-tools. Due to the thin walls, the ratio internal reaction volume and active internal reaction surface/total reactor volume is very large. However, the main drawbacks of this type of reactor are uneven temperature distribution and limited efficiency [84]. *Figure 1.22* shows a cross-flow heat exchanger/reactor developed at *Forschungszentrum Karlsruhe*.

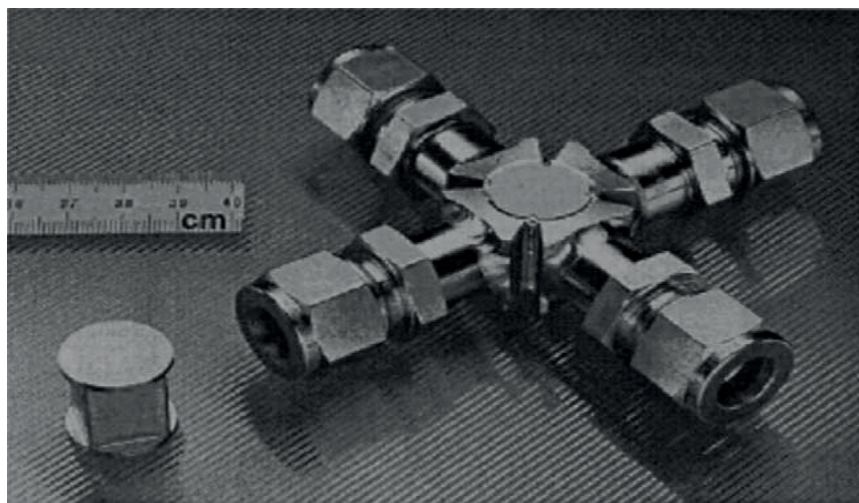
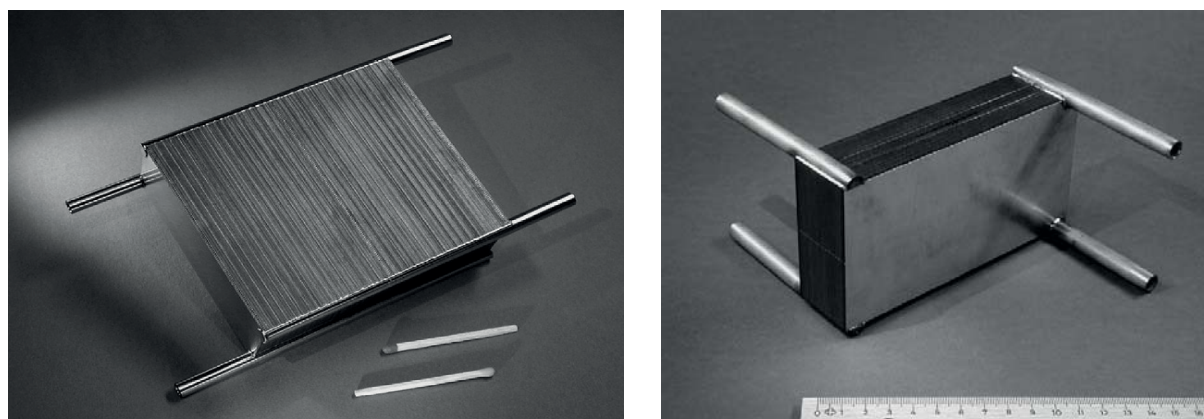


Figure 1.22: Cross-flow heat exchanger/reactor [67].

Counter-flow heat exchangers/reactors

show higher heat exchange properties between the working fluids than the previous type of reactor discussed above, additionally the possibility of developing a temperature profile in the zone where the reaction takes place represents another advantage since higher yields and selectivity can be achieved in one reactor unit [67]. Two fluid paths are common for this type of reactor, on one side the platelets where the reaction takes place are coated with a catalyst whereas the other path is used to supply or remove heat to/from the reaction side. Fitzgerald et al. [85] developed a micro-channel reactor with heat exchanging properties for the steam reforming of octane, the reactor was operated at ambient pressure and 650 °C, conversions of 95 % and a hydrogen selectivity of 90% were achieved. Other experiments were carried out by Walter et al. [86] using a micro-channel reactor with counter-flow heat exchanging properties, it was concluded that the main heat transfer limitation was between the heating oil and the stainless steel of the reactor. *Figure 1.23* shows an example of counter-flow heat exchangers/reactors.



(a) Combined methanol steam re-former/catalytic afterburner (b) Integrated water-gas shift reactor/heat exchanger

Figure 1.23: Counter-flow heat exchangers/reactors developed at Fraunhofer IMM [84].

Counter-flow heat exchangers/reactors for evaporation purposes

As their name indicates, evaporation of liquids by using the reaction heat can take place in this type of reactor. For instance Tonkovich et al. [87] obtained 90% size reduction by implementing a micro reactor for the burning of anode gas of the fuel cell with an efficiency of 93.2%, the size reduction was attributed to the micro-channels. Another example is the micro reactor developed by Drost et al. [88] for combustion purposes, the reactor achieved up to 91% efficiency.

1.4.2.3 Mechanisms of catalyst deactivation

According to Bartholomew [89], this phenomena is inevitable and can occur in different ways i.e. catalysts can be poisoned by other products of side reactions, their surfaces, pores and voids can be as well fouled by carbon or coke. In case the reaction takes place at high temperatures, crystallite growth or collapse of the catalyst support structure can suggest thermal degradation. Bartholomew [89] defined the following deactivation mechanisms: poisoning, fouling, thermal degradation, vapour formation, vapour-solid and solid-solid reactions, attrition and crushing. *Catalyst poisoning* is a chemical deactivation and consists in the strong chemisorption of reactants, products on the catalyst active sites leading to their blockages and possible changes in the electronic or geometric structure of the surface [90][91]. *Fouling* is a mechanical deactivation and consists in the deposition of components from the fluid phase on the catalyst surface and pores. *Thermal degradation* is, as its name

suggests, a thermal deactivation and consists in the loss of catalyst surface or support due to thermal stress. *Vapour formation* is also a chemical deactivation and consists in the reaction of gas with the catalyst to produce volatile compounds. *Vapour-solid and solid-solid reactions* is also classified as a chemical deactivation and consists in the reaction of fluid or support with the catalyst phase, the results of such reactions are inactive parts of catalysts which decrease its activity. *Attrition* is a mechanical deactivation and consists in the loss of catalytic material due to abrasion. *Crushing* is also a mechanical deactivation and consists in the loss of internal surface area due to mechanical stress (crushing) of the catalyst.

1.4.3 Summary and conclusions

In this section, the biologic and catalytic methanation were presented and discussed, there are some differences between biologic and catalytic methanation which should be considered when designing a plant. In *table 1.6* a comparison between these processes is presented. It is important to note that while the operating temperature (300 - 550 °C) of the catalytic methanation represents an opportunity to use some heat in order to increase the overall process efficiency, the biologic methanation takes place in a considerable lower temperature range (40 - 70 °C) at which much less heat can be used. Methanation plants which use the biologic approach are not able to process as many feed gas as the catalytic methanation (GHSV <100 for the biologic methanation, GHSV 500 - 5000 for the catalytic methanation). However, regarding the flexibility, the catalytic methanation is less flexible than the biologic methanation, due to slow startup times of the reactor.

Additionally, *table 1.7* lists the different reactor concepts used for the catalytic methanation as well as their pros and drawbacks.

Table 1.6: Comparison between catalytic and biologic methanation [24].

	Methanation	
	Catalytic	Biologic
Catalyst	Mostly nickel based	Biological enzymes
Reactor technology	Fixed-, fluidised-bed, bubble column, honeycomb, micro-channel	Stirred-tank reactor
Operating temperature (°C)	300 - 550	40 - 70
Operating pressure (bar)	> 10	> 4
Stage of development	Commercial	Lab/pilot
GHSV (h ⁻¹)	500 - 5.000	< 110
Reaction rate limitations	Kinetics (fixed-bed), gas-liquid mass transfer limitations (bubble-column)	Gas-liquid mass transfer limitations
CH ₄ outlet vol.-%	> 95 %	> 95 %
Tolerance to sulphuric components	Low	High
Flexibility	Moderate	High
Energy demand (kWh/m ³) ¹²	< 0.4	0.4 - 1.8
Use of the reaction heat	Very good (to cover electricity demand and CO ₂ separation)	Limited (to warm up the biogas digester)

¹²Kilowatt hour per cubic meter CH₄ produced at 16 bar (feeding pressure)

Table 1.7: Reactor concept pros and drawbacks [92].

	Reactor Technology	
	Pros	Drawbacks
Adiabatic	Wide range of operation, high reaction rate,	High thermal load on the catalyst, removal of heat is a challenge,
Fixed-bed	low mechanical load on catalyst, simple catalyst handling, dimensioning and scale-up	temperature gradients, multiple reactors in series, several compressors and/or heat exchangers required
Fluidised-bed	Effective heat removal, small temperature gradients, good mass transfer, only one reactor required	Catalyst attrition and entrainment, reduction of conversion due to bubbling
Bubble-column	Very effective heat removal, isothermal conditions, catalyst replacement during operation, less sensitive to fluctuating feed streams	Mass transfer limitations between liquid and gas phase, liquid phase degradation and evaporation, backmixing possible
Honeycomb	Pressure drop is two order of magnitude lower than conventional fixed-bed reactors, high thermal conductivity.	Optimisation and scaling studies are needed, low CH ₄ content in the product gas.
Micro-channel	Size and investment/operating cost reduction, easy scale-up process, good heat exchange.	Catalyst cannot be replaced during operation

2 PtG concept and carbon dioxide sources

This chapter presents a definition of the PtG concept as well as a description of the carbon dioxide sources that can be integrated to PtG plants. Carbon dioxide sources can be obtained from industrial process such as cement and electricity production. Biogas plants represent another way of providing carbon dioxide to the PtG process. Finally, carbon capture and storage technologies (CCS) are addressed and discussed.

2.1 Concept

PtG is a storage concept which enables electricity surpluses from RES to be converted into CH_4 and/or H_2 . Electricity surpluses are directed to electrolyzers which split water into hydrogen and oxygen; the latter can be either released into the atmosphere or used in the chemical or metallurgical industry [19]. Hydrogen can react with carbon dioxide sources to produce methane through the Sabatier reaction which was defined in equation (1.2). The product gas can be stored into the gas grid in order to produce electricity, heat when demanded or it can be used as fuel in the mobility sector [93][19].

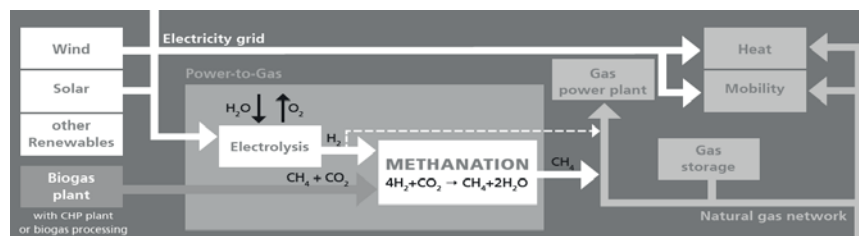


Figure 2.1: Power-to-Gas concept [93].

Figure 2.1 illustrates the PtG concept. The process efficiency from electricity to gas is ca. 63.6% without using the heat produced by the exothermic reaction. However, if the stored

gas is used to produce electricity, the overall process has an efficiency¹ of 38%. *Figure 2.2* illustrates the efficiency of a PtG plant assuming that the SNG is used to produce electricity.

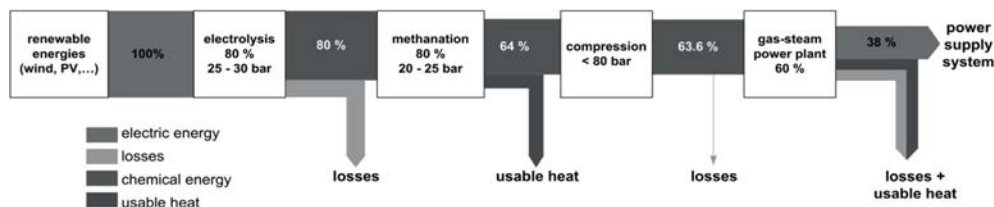


Figure 2.2: Power-to-Gas efficiency [94].

2.2 Carbon dioxide sources

According to Sterner [93] CO₂ can be obtained via absorption, adsorption, condensation and membrane separation processes from the air [93]. Adsorption, condensation, and membrane separation processes are not feasible due to the fact that these are energy-intensive. On the other hand, absorption processes have proven to be an efficient way to obtain CO₂ from the air. PtG plants coupled to absorption units allow the possibility to recycle carbon dioxide and therefore these can be useful in the scenario where the target values established by the IPCC regarding CO₂ emissions are not met [93].

Another possibility is to couple PtG plants to biogas digesters. The produced biogas can be fed into the Sabatier reactor after a desulphurisation unit, whereas the oxygen which is produced via electrolysis can be used for biogas production [93]. PtG plants which are coupled to biomass gasification facilities can be similarly integrated i.e. the gas produced at the gasification step which contains CO, CO₂, CH₄ and H₂ can be directed into the Sabatier reactor to be upgraded, hydrogen can be produced via electrolysis in case there is not enough produced H₂ at the gasification step. PtG plants coupled to sewage facilities represent another option where oxygen can be used in the waste water treatment or sludge activation [93]. Additionally, PtG plants can be coupled to fossil power plants and natural gas sites. In the former scenario, carbon dioxide can be captured after the combustion process. In the latter scenario, it is common to have CO₂ as waste component during the site exploration [93]. Jentsch [5] reported in her work that PtG plants could produce a

¹Process efficiency is calculated assuming a gas-steam power plant with an efficiency of 60%

methane quantity equivalent to 420^2 TWh_{th}/annum in Germany, if these plants are coupled to biological and industrial CO₂ sources. In comparison to the storage capacity of the technologies deployed in the German electric grid, this is clearly a higher figure [93].

PtG technologies face challenges regarding technical aspects such as catalytic deactivation and plant flexibility due to slow start-up/shut-down times. Catalyst deactivation may occur as a cause of coke formation or poisoning [93].

2.2.1 Biogas as carbon dioxide source

The work published by Trost et al. [96] discussed two possibilities of coupling biogas plants with PtG plants as CO₂ sources. The first possibility refers to the coupling of PtG plants with biogas plants which feed-in into the gas grid, this type of biogas plants require an upgrading unit after the fermentation in order to meet the requirements of the *Deutscher Verein des Gas- und Wasserfaches e.V.* (DVGW) regarding the gas quality. After the upgrading process, a CO₂-stream with a composition up to 99 vol.-% CO₂ may be obtained, this CO₂ is in most cases released into the atmosphere without being used; Trost reported the operation of 50 upgrading units with a feed-in capacity of 42000 Nm³/h biogas during 2010 in Germany [96]. Besides the use of the nearby gas grid infrastructure, the released heat at the electrolysis and methanation unit can be redirected in the biogas plant itself and/or in the upgrading unit in order to increase the efficiency of the overall system. Considering this operating mode, the biogas plant can be operated with a high number of full load hours, if the electricity demand needs to be matched, a CHP unit or a gas-fired power plant can start operating, the PtG plant will only operate using the CO₂ accumulated in the upgrading unit when electricity surpluses from renewable energy sources arise [96].

The second possibility is the *direct methanation of biogas*. Thereby, a mixture of CH₄ and CO₂ from the biogas plant is directed to the methanation unit in order to upgrade it and meet the DVGW regulations regarding gas quality [96]. It is important to remark that this operating mode allows the biogas plant to be more flexible i.e. in case there is electricity demand, the biogas is directed to the CHP unit, but in case electricity surpluses arise, the biogas is bypassed to the methanation unit and stored into the gas grid without operating the CHP unit [96].

²This corresponds to 17.5% of the final energy consumption in Germany during 2014 and 40% of the gross electricity production in the same year assuming conversion efficiencies of 60% [95].

In Germany, there are 223 biogas plants which feed into the gas grid an average amount of $623,11 \text{ Nm}^3/\text{h}$ [97], this corresponds to an average rated power³ of $6.9 \text{ MW}_{\text{el}}$ designated to electrolyzers in case these biogas plants are coupled as CO_2 source to PtG plants. Trost et al. [96] discussed as well the potential of biogas plants which can be coupled to PtG plants for *direct methanation* purposes. In this case 5905 biogas plants (status 2010) with an hourly production of 620000 Nm^3 are available and therefore $6900 \text{ MW}_{\text{el}}$ can be designated to electrolyzers. *Figure 2.3a* illustrates the locations of biogas plants regarding the electric rated power of their CHP unit. There are some areas with great potential such as Schleswig-Holstein, Niedersachsen und Bayern [96]. On the other hand, *figure 2.3b* illustrates the adequate locations regarding the CO_2 supply where direct methanation PtG plants with a capacity of 5 MW_{el} could operate in Germany [96].

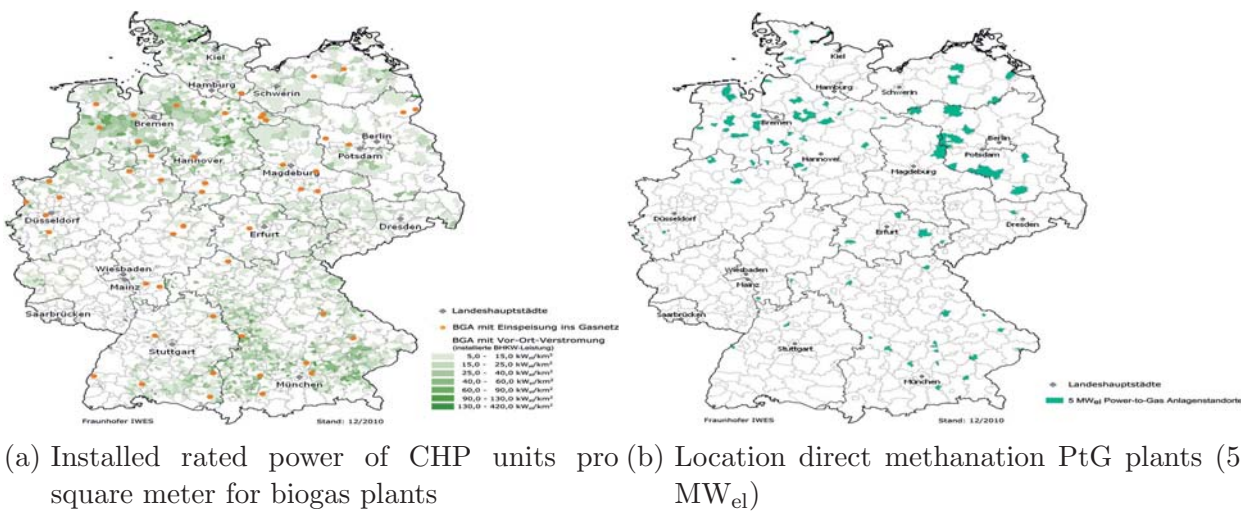


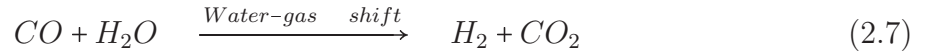
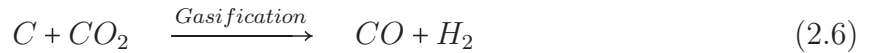
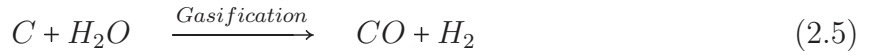
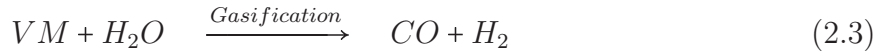
Figure 2.3: CO_2 potentials and locations for PtG plants in Germany [96].

2.2.2 Carbon dioxide capture and storage technologies

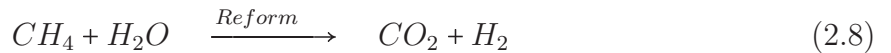
Regarding the capture process, carbon dioxide capture and storage technologies (CCS) can be classified as post-combustion, pre-combustion and oxyfuel combustion CCS technologies. *Post-combustion technologies* separate CO_2 from the flue gas after the combustion of the fuel, it is a mature technology and can be integrated to coal- and gas-fired plants, its main

³Based on the proportion $11.1 \text{ kW}_{\text{el}}/\text{Nm}^3$ biogas per hour [96]. The following assumptions were made: gas composition of the biogas produced 40% CO_2 and 60% CH_4 ; electrolyser efficiency of 75%; methanation efficiency of 83% [96].

drawback is the high energetic effort required to concentrate CO₂ (from 7% to more than 95.5%) which can represent a 70% increase in the price of electricity production according to US. National Energy Technology Laboratory [98]. *Pre-combustion technologies* pretreat before the combustion of the fuel (coal or gas). Specifically in the case of coal-fired plants, a gasification process with low oxygen takes place which leads to the production of syngas (equation 2.3, 2.5, 2.6). The syngas reacts then with steam and the reaction produces H₂ and CO₂ (equation 2.7).



In the case of gas-fired plants, CH₄ is reformed to syngas (equation 2.8) which then reacts in the water-gas shift reaction to increase the content of H₂ and produce CO₂ [98].



Oxyfuel combustion is the fuel combustion in the presence of oxygen instead of air. The oxygen is separated from the air before the combustion takes place, this results in a decrease of NO_x components in the exhaust gas which affect the separation process as well as higher flame temperatures. Thus, recirculation of the flue gas to the burners to control the flame temperature. The product gas which contains CO₂, SO₂ and particulate matter can be purified in order to obtain a rich CO₂ stream. The main drawback of oxyfuel CCS technologies is the separation of oxygen from the air, this is an energy intensive process that represents an increase of the plant energy demand (over 7%) [98].

Regarding the separation technology, CO₂ can be separated from the flue/fuel gas steam through wet scrubber, dry regenerable sorbents, membranes, cryogenics, pressure and tem-

perature swing adsorption [98]. Absorption is carried out by a liquid sorbent which can be regenerated through stripping, heating or other regenerative process. It is the most mature CO₂ separation technique. Sorbents such as monoethanolamine (MEA), diethanolamine (DEA), potassium carbonate are normally implemented. Veawab et al. [99] reported MEA as the most efficient⁴ (over 90%) sorbent among the alkanolamines. For instance, the aim of the integrated European project CASTOR was to test the performance of energy efficient sorbents (MEA, CASTOR 1, CASTOR 2) as part of a post-combustion CCS technology for coal flue gas in a pilot plant [100]. 55 - 110 kg/h of flue gas with a partial pressure of CO₂ from 35 - 135 mbar were fed into the absorber (*figure 2.4*) which had a packing height of 4.2 m and a diameter of 0.125 m. The rich sorbent was then fed into the desorber which consisted in a column with a packing height of 2.52 m and a diameter of 2.52 m, the outlet stream of the desorber contained mainly CO₂. During this process CO₂ removal rates up to 54% were reached [101].

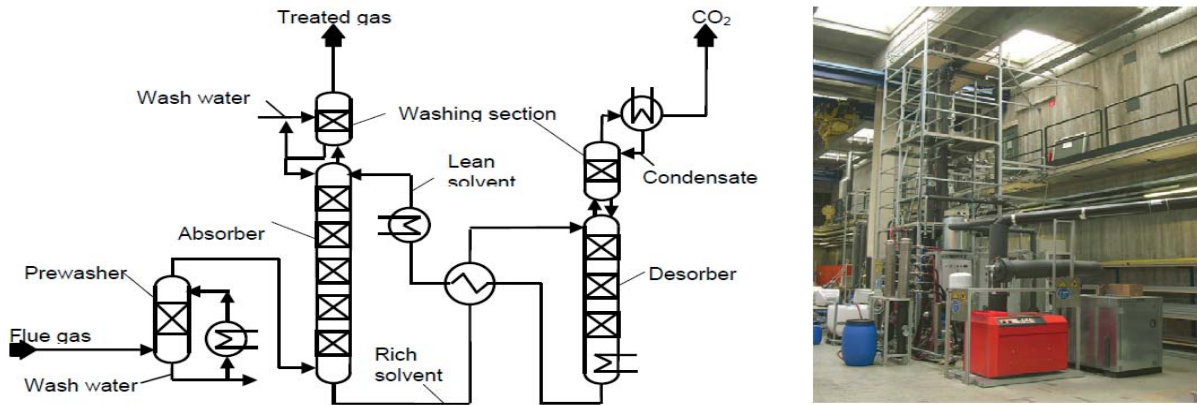


Figure 2.4: Post combustion CCS pilot plant using reactive absorption [101].

As part of the same European project, another CO₂ absorption plant was built at Esbjerg power station in Denmark. This was also a pilot plant which was able to process 5000 Nm³/h flue gas (12% CO₂) and produce 1 tCO₂/h, four experimental runs of 1000 hours each, were carried out in order to test the performance of a 30%-weight MEA and again the sorbents CASTOR 1 and CASTOR 2 were used. In this CO₂ pilot plant, the flue gas was

⁴The sorbent efficiency was calculated as follows:

$$\eta = 100 \cdot \left[1 - \left(\frac{y_{out}}{1 - y_{out}} \right) \left(\frac{1 - y_{in}}{y_{in}} \right) \right] \quad (2.9)$$

y_{in} and y_{out} denote the mole fractions of CO₂ at the bottom and the top of the absorption column respectively [99].

directed from the coal-fired power plant into the absorber which had an internal diameter of 1.1 m and a height of 20 m [100]. The rich sorbent (MEA) was then directed into the stripper unit which had an internal diameter of 1.1 m and a height of 13 m (*figure 2.5*) [100]. A CO₂ removal of 90% for the three sorbents was achieved. Additionally, a specific steam consumption of 3.5 - 3.8 kWh/t CO₂ [100] was required in the reboiler.

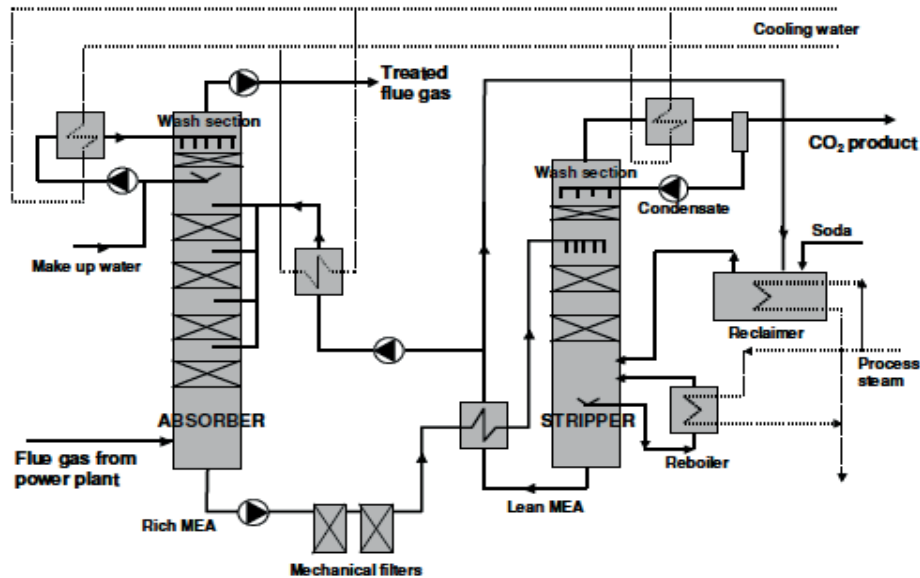
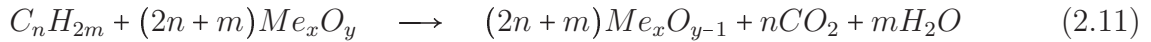
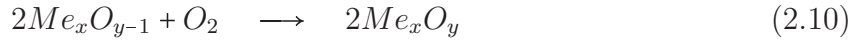


Figure 2.5: CO₂ absorption pilot plant in Esbjerg (Denmark) [100].

Furthermore, Kittel et al. [102] reported in his work corrosion of carbon steel pieces in the stripper where high temperature and fluid velocity are common under operating conditions. Other issues such as solvent loss, generation of volatile components as well as amine emissions which are harmful for humans and the environment must be considered when deploying CO₂ absorption based on alkanolanimes as CCS technology [98]. CO₂ can also be captured through adsorption processes, thereby a solid sorbent which is able to bind the CO₂ on its surface is implemented. Ideally speaking, a good sorbent should have a high selectivity for CO₂, a large specific surface area and could be easily regenerated [98]. The most common material used are zeolites, molecular sieves, calcium oxides, activated carbon, hydrotalcites and lithium zirconate [98]. Subsequently, the adsorbed CO₂ can be recovered by pressure or temperature swing processes.

Chemical looping combustion (CLC) is another technique which is implemented for capturing CO₂, thereby a metal oxide is used as oxygen carrier (OC) for fuel combustion purposes. The process consists of two stages, in the first stage, the carrier is oxidised in an

air reactor (AR) (*equation 2.10*); during the second stage, the fuel reacts with the oxygen carrier in a fuel reactor (FR) producing CO₂ and a reduced oxygen carrier thus closing the loop (*equation 2.11*) [103].



Furthermore, CLC processes can be classified according to the type of primary fuel, type of reactor design and the type of oxygen carrier. Regarding, the type of primary fuel, CLC processes can be classified as CLC of gaseous fuels where mainly natural gas and refinery gas are used, CLC of solid fuels where coal, pet-coke, solid wastes and biomass are implemented or CLC of liquid fuels where mainly non-sulphurous kerosene as well as heavy fuel oils and vacuum residues produced during the crude oil refining process are used [103]. Regarding the reactor type, CLC processes can be carried out in moving-/fluidised-bed, fixed or rotating reactors, their configuration or/and combination can variate in order to optimise the operation and therefore the CO₂ output for different types of fuels and oxygen carriers e.g. two or more fluidised-/moving-bed reactors can be interconnected or alternated [103]. Thon et al. [104] reported a 25 kW CLC system which consisted of fluidised-bed reactors where 90% of carbon capture efficiency was achieved, Ströhle et al. [105] reported the operation of a 1 MW_{th}⁵ CLC pilot plant which consisted of two interconnected fluidised-bed reactors at the Technical university of Darmstadt in Germany, the plant was able to achieve 80 % of carbon capture efficiency; the air reactor had an inner diameter of 0.59 m, a height of 8.66 and it was designed to operate at 1050 °C. The fuel reactor had an inner diameter of 0.4 m, a height of 11.35 m and it was designed to operate at 970 °C [105]. Alternating fixed-/fluidised-bed reactors are another type implemented in CLC processes. In this case at least two reactors operate in parallel and alternately, in both reactors oxidation and reduction processes take place. Rotating reactors represent the last type of reactor which can be implemented for CLC purposes, this type of reactor consists of two concentric sections, one of them contains an oxygen carrier which is rotated between different sectors belonging to the other section where air and fuel are fed radially, a stream of inert gas is fed in between the air and fuel stream in order to avoid mixing [103]. Håkonsen et al. [106] reported a fuel conversion of 90% and a carbon capture efficiency over 90% in a lab-scale rotating reactor for CLC purposes, it is important to note that

⁵The capacity corresponds to a solid fuel flow of 150 kg/h [105]

the latter value dropped when the rotational frequency of the section increased [106][103]. Figure 2.6 depicts the reactor types described above.

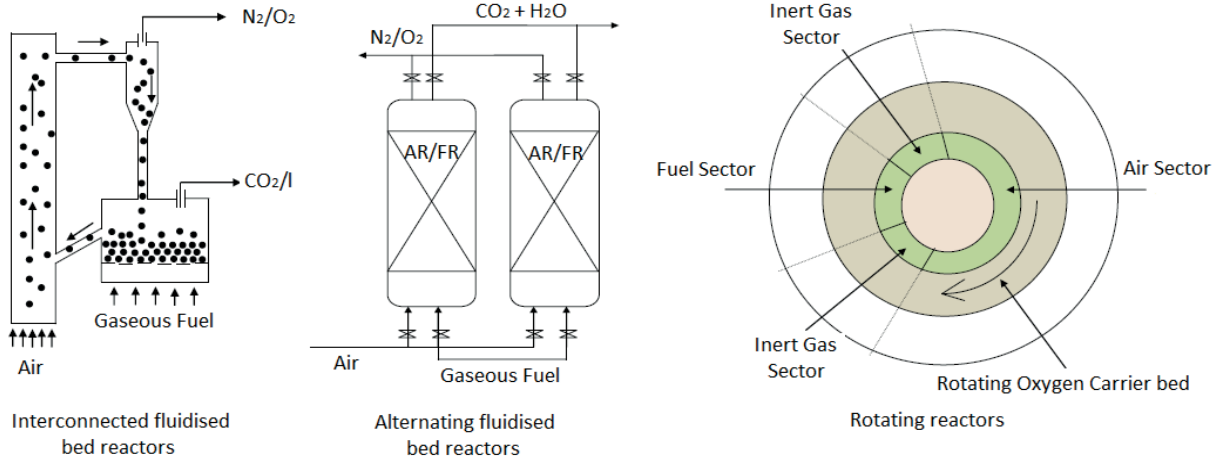


Figure 2.6: Reactor types used for CLC purposes [103].

CLC technologies can be as well classified regarding the type of oxygen carrier used in the process, they should be environmentally friendly, have a great carrying capacity, have a high reactivity during the oxidation and reduction process, have high resistance to mechanical stresses, be able to be grounded to the size required, be cost effective, have high melting points, withstand a determined number of operating cycles and the carbon deposition on the material should be minimal [103]. According to the aforementioned characteristics, the following oxygen carriers for CLC processes have been identified: Ni-based, Cu-based, Fe-based, Mn-based, Co-based [103]. Ni-based oxygen carriers have been well studied, they are very reactive and therefore high conversions can be achieved, moreover Ni-based oxygen carriers are able to operate at high temperatures (900 - 1100 °C) however some disadvantages such as toxicity, high porosity which causes low reaction rates [103] have been identified. Cu-based oxygen carriers on the other hand show high reaction rates and are able to transfer oxygen very well. Moreover, high conversion can be achieved with them, they are less expensive than other metal oxides and their use do not represent serious concerns to the environment. However, decomposition at low temperatures and agglomeration at high temperatures are considered as disadvantages for this type of oxygen carriers [103]. Fe-based oxygen carriers present the advantage of being non-toxic, environment friendly and cheap. Although these advantages, Fe-based oxygen carriers show weak redox characteristics as well as low fuel conversion and less oxygen transport capacity [103]. Mn-based oxygen carriers are similar to Fe-based oxygen carriers but they are not

very reactive. Although, Co-based oxygen carriers have an exceptional oxygen transfer capacity, high costs, toxicity and low reactivity represent some disadvantages for this type of oxygen carriers [103].

Membrane separation represents another possibility to capture CO₂ in CCS processes. The working principle of such membranes is to allow only CO₂ to flow through, while the other components of the gas stream are not allowed. As advantage this technology is economically attractive due to low costs and simplicity. However, low concentrations of CO₂ and pressures in the flue gas represent an issue due to the fact that the use of high selective membranes is required in order to achieve a CO₂ recovery of 80% with a purity of at least 80% [107][108]. A suitable membrane which is used for CO₂ purposes should have a high CO₂/N₂ permeability and selectivity, thermal and chemical resistance to the operating conditions, age resistance [108]. Polyimides, facilitated transport, mixed matrix, carbon molecular sieves and poly-ether-oxide are some types of membranes which have shown interesting properties regarding CO₂ selectivity and/or permeability [108]. Polyimides are the most researched type of membrane, this type of membrane is thermal and chemical stable, and exhibits a high CO₂ selectivity. Facilitated transport membranes contain a carrier which has affinity to certain molecule, this type of membrane has shown good CO₂ selectivity even in the presence of water vapour [108]. Mixed matrix membranes are manufactured in order to improve the properties of polymeric membranes. They are made of an inorganic material (micro or nano scale) which is integrated into a polymeric membrane allowing it to have an easy processability and a better performance [108]. Carbon molecular sieves is another type of membrane which can be implemented to separate CO₂. This type of membrane shows good transport properties for light gases, are thermal and chemical stable. However, their high fragility and costs represent the main drawbacks for this type of membrane [108]. Poly-ethylene oxide membranes have a strong affinity of CO₂, their manufacturing process is relatively easy but, this type of membrane tends to crystallise thus gas permeability is affected[108].

Research is being carried out in order to develop membranes which are able to provide higher flux rates and CO₂ selectivity. Regarding membrane application, the company Membrane Technology Research worked together with the Arizona Public Service Co. Cholla power plant to demonstrate a membrane system which was able to process flue gas from a coal-fired power plant and produced 1 ton CO₂/day [108]. Furthermore, other tests with

a novel counter-current membrane system suggested that for a 600 MW coal-fired power plant, a membrane with a surface of 700000 m² is required in order to capture 90% of the CO₂ contained in the flue gas stream. It was also estimated that such a system is able to produce 10000 ton CO₂/day [108]. Furthermore, Carbozyme is trying to develop a type of facilitated membrane which improves CO₂, a lab-scale system was tested and the results showed a CO₂ removal of 85% from a gas stream containing 25% CO₂. Regarding the energy requirements of membrane system for CCS purposes, Bounaceur et al. [107] stated that the energy demand of the membrane system is related to the CO₂ concentration in the flue gas stream. A membrane system will consume more energy than an absorption process for a gas stream containing 10% of CO₂, it is not longer the case for values from 20% CO₂ or higher i.e. implementing membranes with a selectivity of 60% leads to reasonable CO₂ recoveries and compositions with prices even lower than absorption processes [107].

Hydrate based gas separation (HBGS) is a new and promising technology which can be deployed for CO₂ separation purposes. During HBGS processes, gas hydrates are formed when a molecule is incorporated into a lattice containing basically hydrogen bonded water molecules [109]. Gas hydrates are non stoichiometric crystalline compounds that allow CO₂ to be separated from the other gases in the stream [109]. According to P. Babu et al. [109], high storage capacity and energy efficiency as well as no environmental damage are some of the advantages of this technology. A study reported that up to 90% of CO₂ can be recovered using hydrate based gas separation [110]. However, this technology is currently in the R&D stage, the low CO₂ concentration in the fuel gas stream, its compression cost and the implementation of further processing units represent other barriers which have to be overcome in the future [109]. *Figure 2.7* depicts a flow process based a hydrate gas formation for CCS purposes.

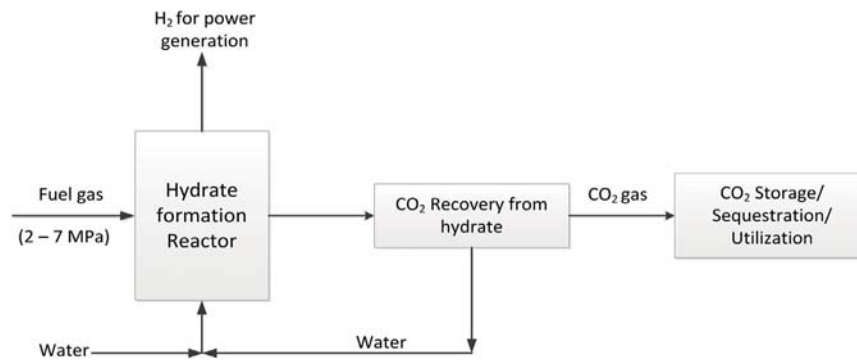


Figure 2.7: Hydrate based gas as CCS technology (process flow diagram) [109].

2. PtG concept and carbon dioxide sources

Cryogenic distillation represents another way to separate CO₂ from other gases. Thereby CO₂ is cooled until its desublimation temperature (-100 °C to -135 °C), solidified and separated afterwards, the process is carried out at high pressure and low temperature which means that its energy demand is relatively high (600 - 660 kWh/ton CO₂) [98]. Up to 90% - 95% of the CO₂ contained in the flue gas can be recovered [98].

3 Modelling

The chapter modelling presents the mathematical background of the simulations. *Section 3.1* introduces the chemical equilibrium concept of the *Sabatier* reaction as well as the *Gibbs free energy*. *Section 3.2* presents the governing equations of the mathematical model used to simulate the performance of the *Sabatier* reactor under different operating conditions. *Section 3.3* describes how to determine the experimental value of the empirical coefficient n , the activation energy E_a and the Arrhenius factor A . Results based on experimental data are presented and discussed. *Section 3.4* describes the spatial discretisation method required in order to solve the model equations. *Section 3.5* describes the model and the simulation environment structure, it also presents the estimated results of the mathematical model. Finally, *Section 3.6* describes how the reactor model can be integrated in the control strategy of a larger PtG plant.

3.1 Chemical equilibrium

Considering a certain chemical reaction, the chemical equilibrium is the state at which reactant and product concentrations have no further change [111]. The final species concentrations depend on the nature of the reaction and the thermodynamic conditions in which the reaction is carried out. In order to explain the chemical equilibrium of the *Sabatier* reaction, the Gibbs free energy G is an important quantity which has to be defined. The Gibbs free energy determines whether product formation takes place spontaneously or not [112]. It is defined as follows:

$$G = H - TS \tag{3.1}$$

3. Modelling

Where H denotes the enthalpy, T the absolute temperature and S the entropy of the system. If the process is isothermal, the change of the Gibbs free energy in a process under certain temperature, pressure conditions and certain concentration of reactants and products is represented as follows [112]:

$$\Delta G = \Delta H - T\Delta S \quad (3.2)$$

The changes of enthalpy and entropy in *equation* (3.2) are calculated by the difference between the product and reactant species.

$$\Delta H(T_2) = \Delta H(T_1) + \int_{T_1}^{T_2} C_p dT \quad (3.3)$$

$$\Delta S(T_2) = \Delta S(T_1) + \int_{T_1}^{T_2} \frac{C_p}{T} dT \quad (3.4)$$

Where C_p stands for the heat capacity and it is calculated as follows:

$$C_p = A + B \left[\frac{(C/T)}{\sinh(C/T)} \right]^2 + D \left[\frac{(E/T)}{\sinh(E/T)} \right]^2 \quad (3.5)$$

A , B , C , D and E are constants taken for each species from the *Dortmund data bank*. A negative change of the Gibbs free energy means that product formation is favoured under those conditions, whereas a positive change of the Gibbs free energy means that reactant formation is favoured. The process continues until the equilibrium is reached, at that step the change of Gibbs free energy equals zero [112].



If the chemical reaction (3.6) is considered, Kee et al. [112] stated that the change of the standard molar Gibbs free energy ΔG_r° can be defined as:

$$\Delta G_r^\circ = x\Delta G_{f,X}^\circ + y\Delta G_{f,Y}^\circ - a\Delta G_{f,A}^\circ - b\Delta G_{f,B}^\circ \quad (3.7)$$

Where, a, b, x, y are the stoichiometric coefficients of species A , B , X , Y respectively and ΔG_f° stands for the standard free energy of formation for a chemical component. In order to estimate the equilibrium volumetric percentage of CH_4 and CO_2 a temperature range between 200 and 700 °C and a pressure range between 6 and 16 bar are considered. Additionally, the Gibbs free energy for the different species is calculated in terms of their

enthalpy and entropy as it was defined in *equation* (3.2), the change of the standard molar Gibbs free energy is calculated according to *equation* (3.7). Furthermore, an extend of reaction ($\partial\xi$) is assumed therewith the outlet molar flow of species J_k is estimated as follows:

$$J_{CO_2} = (1 - \partial\xi) \cdot J_{CO_2in} \quad (3.8)$$

$$J_{H_2} = J_{H_2in} - 4\partial\xi \cdot J_{CO_2in} \quad (3.9)$$

$$J_{CH_4} = J_{CH_4in} + \partial\xi \cdot J_{CO_2in} \quad (3.10)$$

$$J_{H_2O} = J_{H_2Oin} + 2\partial\xi \cdot J_{CO_2in} \quad (3.11)$$

$$J_{total} = J_{CO_2} + J_{H_2} + J_{CH_4} + J_{H_2O} \quad (3.12)$$

Where, J_{kin} denotes the inlet molar flow of species k . The molar fraction of species k in the mixture can be calculated as the ratio between the molar flow of species k and the total molar flow J_{total} :

$$X_{CO_2} = J_{CO_2} / J_{total} \quad (3.13)$$

$$X_{H_2} = J_{H_2} / J_{total} \quad (3.14)$$

$$X_{CH_4} = J_{CH_4} / J_{total} \quad (3.15)$$

$$X_{H_2O} = J_{H_2O} / J_{total} \quad (3.16)$$

The species partial pressure can be calculated as the product of the molar fraction and the gas phase pressure P :

$$p_{CO_2} = X_{CO_2} \cdot P \quad (3.17)$$

$$p_{H_2} = X_{H_2} \cdot P \quad (3.18)$$

$$p_{CH_4} = X_{CH_4} \cdot P \quad (3.19)$$

$$p_{H_2O} = X_{H_2O} \cdot P \quad (3.20)$$

The equilibrium constant K_e can be defined as follows:

$$K_e = \frac{[p_{CH_4}] [p_{H_2O}]^2}{[p_{H_2}]^4 [p_{CO_2}]} \quad (3.21)$$

3. Modelling

Additionally, the equilibrium constant can be related to the change of the Gibbs free energy by means of the following expression:

$$\Delta G = \Delta G_r^\circ + RT \cdot \ln(Ke) \quad (3.22)$$

Where, R stands for the universal gas constant and T for the absolute temperature. The equilibrium volumetric percentage of the species is estimated when ΔG in *equation* (3.22) equals zero. *Figure 3.1* shows the equilibrium volumetric percentage of CH_4 and CO_2 for the temperature and pressure range mentioned above. In the case of CH_4 , an increase in the temperature leads to lower concentrations, whereas an increase in the pressure leads to higher concentrations. In the case of CO_2 , an increase of the temperature leads to higher concentrations, whereas an increase in the pressure leads to lower concentrations.

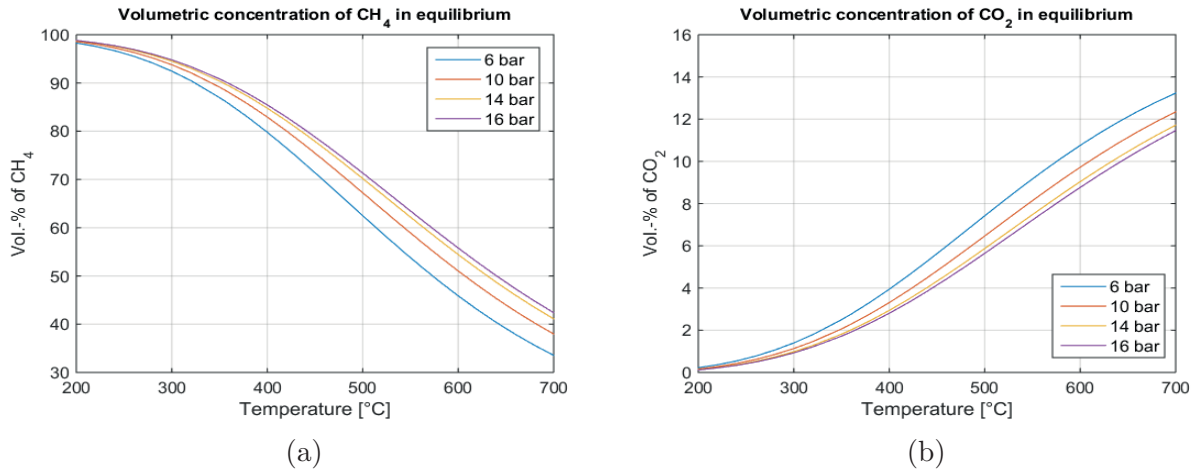


Figure 3.1: Volumetric concentration of CH_4 and CO_2 in equilibrium.

3.2 Governing equations

There have been some works done regarding the simulation of *Sabatier* reactors. Lunde [113] for instance proposed a mathematical model for a single-pass tubular packed-bed reactor which was cooled by an annular co-current flow, the model consisted of a thermal and chemical component. The thermal model did not consider temperature gradients in the radial coordinate but rather in the axial coordinate, axial and radial heat transfer were considered. The chemical component considers mass balance and kinetics, the reaction rate was calculated with an experimental expression proposed by Lunde and Kester

[114][115][4]. Haruhiko et al. [116] also modelled a round-shaped membrane reactor for methanation purposes, the model consisted of spatial ordinary differential equations for the mass balance of the gas components as well as a kinetic expression, the following assumptions were made: plug flow, uniform temperature of the catalyst. Er-rbib and Bouallou [117] modelled and simulated a CO methanation process for the storage of electricity from renewable energy sources, they considered a fixed-bed catalytic reactor and Aspen plusTM was the software implemented for modelling, the kinetics were modelled according to the approach used by Kopyscinski et al. [118], steady state and plug flow as well as negligible axial heat and mass transfer were assumed. Additionally, Schlereth and Hinrichsen [119] modelled a fixed-bed membrane reactor and the following assumptions were made: plug flow, the kinetics were described according to Xu and Froment [120], ideal gas behaviour; mass and energy balances were stated for the spatial and radial coordinate. Hou et al. [121] investigated as well a packed-bed *Sabatier* reactor which was implemented to provide water for space applications, in this case a three dimensional model which considered chemical reaction, axial and radial fluid dispersion, heat transfer among the packed particles and between the outer shell surface and atmosphere as well as heat conductivity in the reactor shell was used.

In this doctoral thesis, a one-dimensional mathematical model was programmed in Matlab-Simulink[®] in order to estimate the performance of the *Sabatier* reactor, the following assumptions were made:

- Good reactor insulation and thus no thermal losses to the environment are considered
- Ideal gas behaviour
- Pressure drop along the reactor channel is considered negligible.
- Plug flow reactor
- Uniform temperature of the channel wall
- Uniform distribution of the reacting gas in the reaction channels
- Operation at constant pressure
- High conductivity across the channel wall thus only heat transfer between the gas phase and the channel wall is considered.

- Heat flux in the axial coordinate due to gas conductivity and species transport

By means of the mathematical model, gas compositions at the reactor outlet can be estimated. The model consists of a system of partial differential mass-, momentum- and energy conservation equations established by Kee et al. [112] and Raja et al. [122] and implemented in Brooks et al. [45] and it is defined below:

$$\frac{\partial \rho}{\partial t} + \frac{\partial \rho u}{\partial x} = \frac{P_c}{A_c} \sum_{k=1}^{K_g} \dot{s}_k W_k, \quad (3.23)$$

$$\frac{\partial \rho Y_k}{\partial t} + \frac{\partial \rho Y_k u}{\partial x} + \frac{\partial j_k}{\partial x} = \frac{P_c}{A_c} \dot{s}_k W_k, \quad (3.24)$$

$$\frac{\partial \rho u}{\partial t} + \frac{\partial \rho u^2}{\partial x} = -\frac{\partial P}{\partial x} + \frac{P_h}{A_c} \tau_w, \quad (3.25)$$

$$\frac{\partial \rho e}{\partial t} + \frac{\partial q_g}{\partial x} = \dot{q}_{gw}. \quad (3.26)$$

3.2.1 Temporal derivative of the species mass fraction

The temporal derivative of the species mass fractions of the gas phase Y_k in the reactor are estimated by means of equation (3.24) which can be rearranged as follows:

$$\frac{\partial Y_k}{\partial t} = \frac{P_c}{\rho A_c} \dot{s}_k W_k - \frac{Y_k}{\rho} \frac{\partial \rho}{\partial t} - \frac{1}{\rho} \frac{\partial \rho Y_k u}{\partial x} - \frac{1}{\rho} \frac{\partial j_k}{\partial x} \quad (3.27)$$

Where, ρ denotes the density of the gas phase, t denotes time, x stands for the spatial coordinate, P_c and A_c denote the catalytically active perimeter and cross-sectional flow area of the channel respectively, W_k denotes the species molecular weight, \dot{s}_k stands for the species molar rate of consumption or production and it is defined as:

$$\dot{s}_k = \nu_k q \quad (3.28)$$

Where ν_k denotes the stoichiometric coefficient of the species k and q stands for the rate of progress for a global *Sabatier* reaction and it is defined as the difference between the forward and the reverse reaction rate.

$$q = k_f^n [X_{CO_2}]^n [X_{H_2}]^{4n} - k_r^n [X_{CH_4}]^n [X_{H_2O}]^{2n} \quad (3.29)$$

$[X_k]$ denotes the molar concentration of the gas-phase species and can be calculated as follows:

$$[X_k] = X_k \frac{P}{RT_g} \quad (3.30)$$

Where X_k is the molar fraction of species k , P stands for the gas phase pressure, R stands for the universal gas constant, T_g denotes the gas phase temperature. n denotes the empirical coefficient, k_f and k_r represent the forward and reverse rates respectively and these are defined as follows:

$$k_f = A \exp\left(\frac{-E_a}{RT_g}\right) \quad (3.31)$$

$$k_r = \frac{k_f}{K_e} \quad (3.32)$$

The forward rate constant k_f is defined in the Arrhenius form, A stands for the pre-exponential Arrhenius or frequency factor and E_a stands for the activation energy, K_e is the equilibrium constant for the *Sabatier* reaction, it is temperature dependent and can be defined as follows according to Hou et al. [121]:

$$K_e = \exp\left[0.503\left(\frac{5600}{T_g^2} + \frac{34633}{T_g} - 16.4\ln(T_g) + 0.00557 \cdot T_g + 33.165\right)\right] \quad (3.33)$$

Where, T_g stands for the gas phase temperature. The species diffusion flux j_k is defined as:

$$j_k = -\rho \frac{W_k}{W} D_{km} \frac{\partial X_k}{\partial x} \quad (3.34)$$

Where D_{km} stands for the mixture diffusion coefficients and are defined as follows:

$$D_{km} = \frac{1 - Y_k}{\sum_{j \neq k}^{K_g} X_j / D_{jk}} \quad (3.35)$$

Where X_j stands for the mole fraction of the species gas-phase and D_{jk} for the binary diffusion coefficients and can be defined according to Kee et al. [112] as follows:

$$D_{jk} = 0.0188 \frac{\sqrt{T_g^3 / W_{jk}}}{P \sigma_{jk}^2 \Omega^{(1,1)*}(T_{jk}^*)} \quad (3.36)$$

The binary diffusion coefficients are a function of the temperature T , pressure P , species reduced molecular weight W_{jk} (equation 3.37), reduced collision diameter σ_{jk} (equation 3.38), reduced collision integral $\Omega^{(1,1)*}$ which at the same time is a function of the reduced

temperature T_{jk}^* and the interaction potential between the molecules [112], the reduced collision integral¹ and temperature are defined in equations (3.39) and (3.40) respectively.

$$W_{jk} = \frac{W_j W_k}{W_j + W_k} \quad (3.37)$$

$$\sigma_{jk} = \frac{\sigma_j + \sigma_k}{2} \quad (3.38)$$

$$\Omega^{(1,1)*}(T_{jk}^*) = 1.0548T^{*-0.15504} + (T^* + 0.55909)^{-2.1705} \quad (3.39)$$

$$T_{jk}^* = \frac{k_B T}{\epsilon_{jk}} \quad (3.40)$$

The reduced temperature is a function of the temperature and the reduced potential well depth (ϵ_{jk}/k_B) which is defined as follows:

$$\frac{\epsilon_{jk}}{k_B} = \sqrt{\left(\frac{\epsilon_j}{k_B}\right)\left(\frac{\epsilon_k}{k_B}\right)} \quad (3.41)$$

Where k_B stands for the Boltzmann constant and ϵ_{jk} represents strength of the interaction between molecules j and k . Kee et al. [112] presents different ways to estimate σ and (ϵ/k_B) for each gas species. The model implemented in this doctoral thesis considers the following definitions for the aforementioned quantities after *5 and 7 rule* respectively:

$$\sigma = 2.393 \left(\frac{T_c}{P_c}\right)^{1/3} \quad (3.42)$$

$$\frac{\epsilon}{k_B} = 0.75T_c \quad (3.43)$$

T_c and P_c stand for the critical temperature in (K) and pressure in (atm).

3.2.2 Temporal derivative of the velocity

The temporal derivative of the gas phase velocity u is estimated by rearranging equation (3.25) as follows:

$$\frac{\partial u}{\partial t} = -\frac{1}{\rho} \frac{\partial P}{\partial x} + \frac{1}{\rho} \frac{P_h}{A_c} \tau_w - \frac{u}{\rho} \frac{\partial \rho}{\partial t} - \frac{1}{\rho} \frac{\partial \rho u^2}{\partial x} \quad (3.44)$$

¹It is defined assuming a Lennard-Jones potential for non-polar interactions. The Lennard-Jones potential describes the molecular interaction between the molecules as a function of the distance, it states that molecules are more-likely to repulse themselves when the distance between them is small, however if the distance between the molecules increases, an attraction force dominates their interaction.

Where P_h denotes the hydraulic diameter of the channel; in equation (3.44), the pressure gradient along the reactor channel $\partial P/\partial x$ is negligible, the shear stress between the fluid and channel wall τ_w is defined as:

$$\tau_w = \frac{f\rho u^2}{2} \quad (3.45)$$

Where f stands for a friction factor that depends on the Reynolds number Re (equation 3.48) and the channel aspect ratio α (equation 3.47)

$$f \approx \left[\frac{13.74}{Re} + \frac{10.38 \exp(-3.4/\alpha)}{Re} \right] \quad (3.46)$$

$$\alpha = \frac{H_{ch}}{W_{ch}} \quad (3.47)$$

Where H_{ch} and W_{ch} stand for the channel height and width respectively.

$$Re = \frac{\rho u P_h}{\mu} \quad (3.48)$$

P_h stands for the channel hydraulic diameter (equation 3.49), ρ stands for the density of the gas mixture, u and μ , gas phase velocity and viscosity respectively (equation 3.50).

$$P_h = \frac{2H_{ch}W_{ch}}{H_{ch} + W_{ch}} \quad (3.49)$$

The viscosity of the mixture can be calculated according to the semi-empirical equation proposed by Wilke [123] as follows:

$$\mu = \sum_{k=1}^K \frac{X_k \mu_k}{\sum_{j=1}^K X_j \Phi_{kj}} \quad (3.50)$$

Where Φ_{kj} can be calculated as shown below:

$$\Phi_{kj} = \frac{1}{\sqrt{8}} \left(1 + \frac{W_k}{W_j} \right)^{-1/2} \left(1 + \left(\frac{\mu_k}{\mu_j} \right)^{1/2} + \left(\frac{W_j}{W_k} \right)^{1/4} \right)^2 \quad (3.51)$$

The values of μ for each gas species are taken from the data base of the National Institute of Standards Technology (NIST).

3.2.3 Temporal derivative of the temperature

The temporal derivative of the gas phase temperature is estimated by using equation (3.26) where the specific internal energy e of the gas mixture can be substituted by the enthalpy and the temporal gradient of the pressure is negligible:

$$h = e + \frac{P}{\rho} \quad (3.52)$$

$$\frac{\partial T_g}{\partial t} = \frac{\dot{q}_{gw}}{\rho C_p} + \frac{\lambda \nabla^2 T_g}{\rho C_p} - \frac{u}{\rho C_p} \frac{\partial T_g}{\partial x} - \frac{1}{\rho C_p} \sum_{k=1}^{K_g} h_k \left(\frac{\partial \rho Y_k u}{\partial x} + \frac{\partial j_k}{\partial x} + \dot{s}_k W_k \right) - \frac{\partial \rho}{\partial t} \frac{\sum_{k=1}^{K_g} Y_k h_k}{\rho C_p} \quad (3.53)$$

Where C_p stands for the heat capacity of the gas mixture and it can be defined as:

$$C_p = \sum_{k=1}^{K_g} Y_k C_{pk} \quad (3.54)$$

\dot{q}_{gw} represents the convective heat transfer between the gas flow and the channel wall and it is defined as follows:

$$\dot{q}_{gw} = \frac{P_h}{A_c} h_{conv} (T_w - T_g) \quad (3.55)$$

Where, h_{conv} the convective heat transfer coefficient and the temperature of the reactor channel wall T_w . h_k stands for the enthalpy of species k and the term $\nabla^2 T_g$ denotes the second spatial derivative of the gas phase temperature.

$$h_{conv} = \frac{N_u \lambda}{P_h} \quad (3.56)$$

Equation (3.56) defines the convective heat transfer coefficient which is a function of the Nusselt number N_u (equation 3.57), the thermal conductivity of the gas phase mixture λ (equation 3.60) and the hydraulic diameter.

$$N_u = 2.977 + 6.854 \left(\frac{1000}{Gz} \right)^{-0.5368} \exp \left(-\frac{42.49}{Gz} \right) \quad (3.57)$$

The Nusselt number is a function of the Graetz number Gz . The Graetz number is a function of the Reynolds, Prandtl number (Re, Pr) as well as channel hydraulic diameter and the channel length x .

$$Gz = \frac{Re Pr P_h}{x} \quad (3.58)$$

$$Pr = \frac{C_p \mu}{\lambda} \quad (3.59)$$

The Prandtl number is a function of the mixture heat capacity C_p , viscosity μ and thermal conductivity λ which is calculated as follows:

$$\lambda = \frac{1}{2} \left(\sum_{k=1}^K X_k \lambda_k + \frac{1}{\sum_{k=1}^K X_k / \lambda_k} \right) \quad (3.60)$$

The values of λ_k which denote the thermal conductivity of species k were taken from the data base of the National Institute of Standards Technology (NIST) as it was done in the subsection 3.2.2.

3.3 Determination of the kinetic parameters of the Sabatier reaction

3.3.1 Lunde and Kester approach

Equation (3.28) defines the destruction/production rate of the gas-phase components which depends on the global rate of progress of the *Sabatier* reaction. The global rate of progress of the *Sabatier* reaction was defined in equation (3.29) as the difference between the forward and backward rates. In this expression, the activation energy E_a , the pre-exponential Arrhenius factor A and the empirical coefficient n are parameters which values are specific to the catalyst nature. Lunde and Kester [4][114] described in their work a procedure to determine experimentally these parameters. For the procedure, a stainless steel tubing reactor with an internal diameter of 1.1 cm and a length of 4.5 cm was used. The reactor was submerged in a oven-heated molten salt bath in order to ensure isothermal operation. According to Lunde and Kester [4], the gas phase kinetics for the *Sabatier* reaction can be proposed as follows:

$$-\frac{d[P_{CO_2}]}{dt} = k_f^n [P_{CO_2}]^n [P_{H_2}]^{4n} - k_r^n [P_{CH_4}]^n [P_{H_2O}]^{2n} \quad (3.61)$$

Where P_k stands for the partial pressure of species k , k_f and k_r are the forward and backward reaction rate respectively. n is equal to 1 for pure gas phase kinetics [114]. If the chemical

3. Modelling

equilibrium is reached, the temporal change of the CO₂ is equal to zero and consequently:

$$Ke = \frac{k_f}{k_r} = \frac{[P_{H_2O}]^2[P_{CH_4}]}{[P_{CO_2}][P_{H_2}]^4} \quad (3.62)$$

The empirical exponent n cancels and K_e can be defined as a classic thermodynamics. Then equation (3.61) can be rewritten as follows:

$$-\frac{d[P_{CO_2}]}{dt} = k_f^n \left\{ [P_{CO_2}]^n [P_{H_2}]^{4n} - \frac{[P_{CH_4}]^n [P_{H_2O}]^{2n}}{Ke^n} \right\} \quad (3.63)$$

The temperature dependence of the reaction rates as mentioned above has the general Arrhenius relationship:

$$k_f^n(T_g) = A \exp\left(\frac{-Ea}{RT_g}\right) \quad (3.64)$$

And the final form of the rate expression can be written as follows:

$$-\frac{d[P_{CO_2}]}{dt} = A \exp\left(\frac{-Ea}{RT}\right) \left\{ [P_{CO_2}]^n [P_{H_2}]^{4n} - \frac{[P_{CH_4}]^n [P_{H_2O}]^{2n}}{Ke^n} \right\} \quad (3.65)$$

Equation (3.65) can be rewritten and integrated over the reactor length:

$$\int_0^\tau A \exp\left(\frac{-Ea}{RT}\right) dt = \int_{P_{CO_2}^{in}}^{P_{CO_2}^{out}} \frac{-d[P_{CO_2}]}{[P_{CO_2}]^n [P_{H_2}]^{4n} - \frac{1}{Ke^n} [P_{CH_4}]^n [P_{H_2O}]^{2n}} \equiv \exp(Y) \quad (3.66)$$

$P_{CO_2}^{in}$ denotes the inlet partial pressure of CO₂, $P_{CO_2}^{out}$ stands for the outlet partial pressure of CO₂, τ denotes the contact time which is normally expressed as the space velocity $S_v = 1/\tau$. Integrating the left side of equation (3.66) and rearranging:

$$A \exp\left(\frac{-Ea}{RT}\right) = S_v \int_{P_{CO_2}^{in}}^{P_{CO_2}^{out}} \frac{-d[P_{CO_2}]}{[P_{CO_2}]^n [P_{H_2}]^{4n} - \frac{1}{Ke^n} [P_{CH_4}]^n [P_{H_2O}]^{2n}} \equiv \exp(Y) \quad (3.67)$$

The evaluation of $\exp(Y)$ in equation (3.67) can be carried out numerically. After each increment, corrected values of P_k are calculated [4] as follows:

$$P'_{CO_2} = P_{CO_2} - \Delta P_{CO_2} \quad (3.68)$$

$$P'_{H_2} = P_{H_2} - 4\Delta P_{CO_2} \quad (3.69)$$

$$P'_{CH_4} = P_{CH_4} - \Delta P_{CO_2} \quad (3.70)$$

$$P'_{H_2O} = P_{H_2O} - 2\Delta P_{CO_2} \quad (3.71)$$

A normalisation of the new pressures is required so that the sum equal the total pressure:

$$P'_{know} = P'_k \frac{\sum_k P_k}{\sum_k P'_k} \quad (3.72)$$

For a particular experimental run the rate expression can be then defined as:

$$\exp(Y) = A \exp\left(\frac{Ea}{RT_g}\right) \quad (3.73)$$

If logarithms on both sides of equation (3.73) are taken, the resulting expression is a line of the form:

$$Y = -\frac{Ea}{R} \left(\frac{1}{T_g}\right) + \ln(A) \quad (3.74)$$

Which means that the slope of a plot Y vs 1/T is -Ea/R and the y-intercept corresponds to the logarithm of the pre-exponential Arrhenius factor. The value of n must be determined by trial and error since incorrect n values do not correlate linearly the experimental data. Lunde and Kester [114] proposed also a method to determine the pre-exponential Arrhenius factor, once the values of n and Ea are known. In this case equation (3.65) can be rewritten as follows:

$$A = e^{Ea/RT} \left[\frac{dP_{CO_2}}{dt} \right] \left(\frac{-1}{[P_{CO_2}]^n [P_{H_2}]^{4n} - \frac{1}{Ke^n} [P_{CH_4}]^n [P_{H_2O}]^{2n}} \right) \quad (3.75)$$

If the change in the CO₂ partial pressure as the gas flows through the reactor is defined as X , the variables can be separated and integrated thus:

$$A = (e^{Ea/RT}) \frac{dX}{dt} \left[\frac{-1}{[P_{CO_2}^{in} - X]^n [P_{H_2}^{in} - 4X]^{4n} - \frac{1}{Ke^n} [X]^n [2X]^{2n}} \right] \quad (3.76)$$

$$A = (e^{Ea/RT}) \frac{\int_{P_{CO_2}^{in}}^{P_{CO_2}^{out}} \left[\frac{dx}{[P_{CO_2}^{in} - X]^n [P_{H_2}^{in} - 4X]^{4n} - \frac{1}{Ke^n} [X]^n [2X]^{2n}} \right]}{\int_{t_{in}}^{t_{out}} dt} \quad (3.77)$$

Substituting the space velocity s_v , equation (3.77) can be rewritten as follows:

$$A = (e^{Ea/RT})_{s_v} \int_0^{P_{CO_2}^{in} - P_{CO_2}^{out}} \left[\frac{dx}{[P_{CO_2}^{in} - X]^n [P_{H_2}^{in} - 4X]^{4n} - \frac{1}{Ke^n} [X]^n [2X]^{2n}} \right] \quad (3.78)$$

3. Modelling

The integral described in equation (3.78) involves known kinetic parameters, inlet and outlet concentrations of CO₂ ($P_{CO_2}^{in}$, $P_{CO_2}^{out}$), inlet concentration of H₂ ($P_{H_2}^{in}$) and the variable X , it can be solved graphically or numerically [114]. *Figure 3.2* shows an example of the method proposed by Lunde and Kester for the determination of the kinetic parameters.

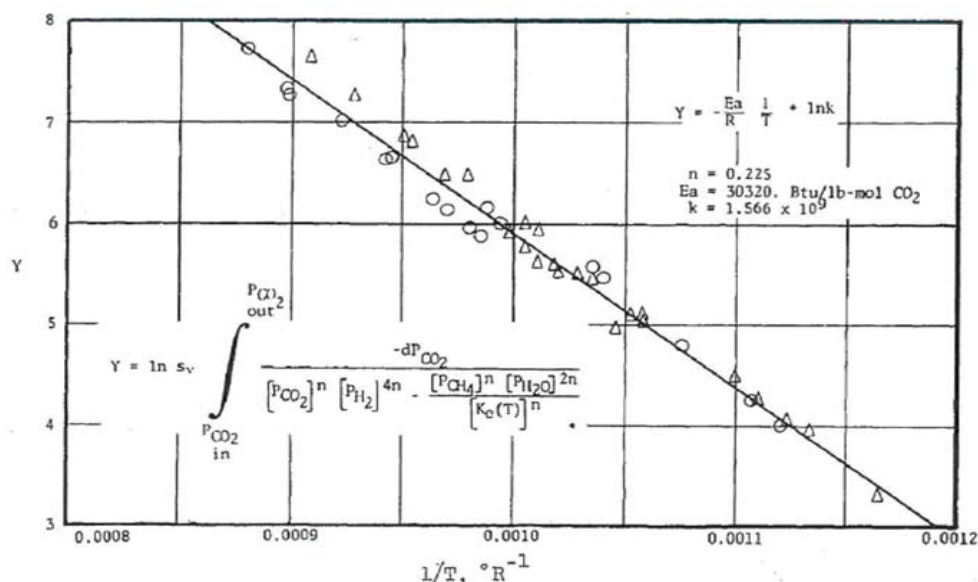


Figure 3.2: Determination of the activation energy using the method proposed by Lunde and Kester.

3.3.2 Experimental runs

For the determination of the parameters E_a , A and n , 22 experimental tests² were run in the lab. Half of them were used to determine the value of E_a whereas the remaining half of the tests were used to determine the value of A . For Each test the volumetric percentages of CO₂, H₂, and CH₄ were measured with the gas chromatograph at the reactor outlet. The reactor temperature, pressure and inlet volumetric flow of species were set by the control strategy of the PtG plant. The reactor and the PtG plant used to carry out the experiments are described in chapter 4. *Figure 7.3* and *7.4* in the appendix list the experimental conditions for all tests. The acquired data were used to estimate the conversion of hydrogen and the volumetric percentage of water vapour produced during the reaction, but the following assumptions are necessary:

²The volumetric percentages of species at the reactor outlet were measured by the gas chromatograph 5 times for each experimental run.

- No production of side products such as ethane and propane
- No production of intermediate product such as carbon monoxide

This estimation was necessary since water is condensed upstream the gas chromatograph. In order to estimate the conversion of hydrogen, the sum of the relative error between the estimated and measured volumetric percentage of species was minimised using equation (3.79). Where $\xi_{H2_{est}}$ is the estimated conversion of hydrogen, $\dot{V}_{k_{est}}$ denotes the estimated³ volumetric percentage of species k at the reactor outlet and $\dot{V}_{k_{mes}}$ denotes the volumetric percentage of species k which was measured by the gas chromatograph at the reactor outlet.

$$\xi_{H2_{est}} = \min \left[\left(\frac{\dot{V}_{CO2_{est}} - \dot{V}_{CO2_{mes}}}{\dot{V}_{CO2_{mes}}} \right)^2 + \left(\frac{\dot{V}_{H2_{est}} - \dot{V}_{H2_{mes}}}{\dot{V}_{H2_{mes}}} \right)^2 + \left(\frac{\dot{V}_{CH4_{est}} - \dot{V}_{CH4_{mes}}}{\dot{V}_{CH4_{mes}}} \right)^2 \right] \quad (3.79)$$

After the estimated conversion of hydrogen was determined, new volumetric percentages of species, molar fractions and partial pressures were calculated at the outlet as follows:

$$\dot{V}_{CO2_{new}} = \dot{V}_{CO2_{in}} - \frac{1}{4} \cdot \xi_{H2_{est}} \dot{V}_{H2_{in}} \quad (3.80)$$

$$\dot{V}_{H2_{new}} = \dot{V}_{H2_{in}} - \xi_{H2_{est}} \dot{V}_{H2_{in}} \quad (3.81)$$

$$\dot{V}_{CH4_{new}} = \dot{V}_{CH4_{in}} + \frac{1}{4} \cdot \xi_{H2_{est}} \dot{V}_{H2_{in}} \quad (3.82)$$

$$\dot{V}_{H2O_{new}} = \dot{V}_{H2O_{in}} + \frac{1}{2} \cdot \xi_{H2_{est}} \dot{V}_{H2_{in}} \quad (3.83)$$

Where $\dot{V}_{k_{new}}$ denotes the new outlet volumetric percentage of species k which is calculated on the basis of the estimated conversion of hydrogen ($\xi_{H2_{est}}$) and the inlet volumetric of species k ($\dot{V}_{k_{in}}$) as well as hydrogen ($\dot{V}_{H2_{in}}$). *Figure 3.3* and *3.4* show the measured and new volumetric percentages of the gas components used in the determination of the activation energy and the pre-exponential Arrhenius factor respectively.

³The estimated values of the volumetric percentages for the species k ($\dot{V}_{k_{est}}$) were computed by varying the conversion of hydrogen from 0 - 1.

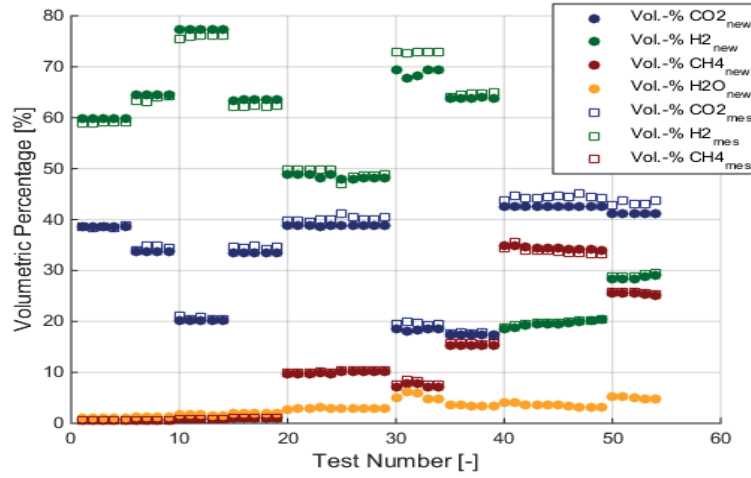


Figure 3.3: Estimated and measured vol.% of CO₂, H₂, CH₄ as well as estimated vol.% of H₂O used in the determination of the activation energy.

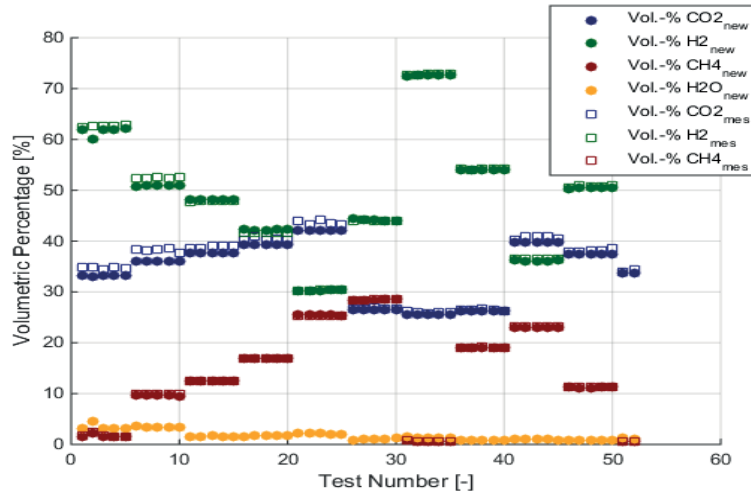


Figure 3.4: Estimated and measured vol.% of CO₂, H₂, CH₄ as well as estimated vol.% of H₂O used in the determination of the pre-exponential Arrhenius factor.

The new molar fractions ($X_{k_{new}}$) were calculated as the ratio between the new volumetric percentages and their total sum ($\dot{V}_{total_{new}}$).

$$X_{CO2_{new}} = \frac{\dot{V}_{k_{new}}}{\dot{V}_{total_{new}}} \quad (3.84)$$

$$X_{H2_{new}} = \frac{\dot{V}_{H2_{new}}}{\dot{V}_{total_{new}}} \quad (3.85)$$

$$X_{CH_4_{new}} = \frac{\dot{V}_{CH_4_{new}}}{\dot{V}_{total_{new}}} \quad (3.86)$$

$$X_{H_2O_{new}} = \frac{\dot{V}_{H_2O_{new}}}{\dot{V}_{total_{new}}} \quad (3.87)$$

The partial pressures of CO_2 , H_2 , CH_4 and H_2O were calculated assuming ideal gas mixture which states that the partial pressure of a species k (P_k) can be calculated as a function of the gas phase pressure and the molar fraction of species k as follows:

$$P_k = X_{k_{new}} \cdot P \quad (3.88)$$

In equation (3.88), P denotes the gas phase pressure which was held at 15 bar during the 22 experimental runs. After the partial pressures of the gas components considering water vapour were calculated, the approach proposed by Lunde and Kester which was described in section 3.3.1 was carried out. Different values of the empirical coefficient n between 0.1 - 1.0 were tested, after calculating the standard deviation of the points generated by equation (3.67) to the curve fit, n was determined as the value which generated the plot with the minimum standard deviation. *Figure 3.5* depicts the value of the standard deviation vs the empirical coefficient n in the aforementioned range.

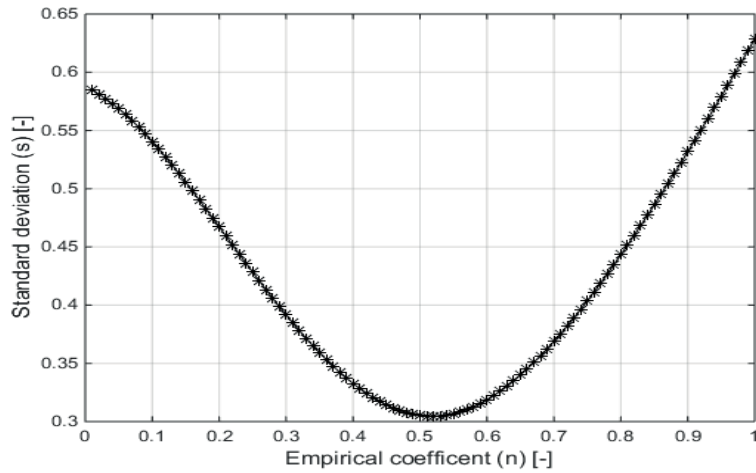


Figure 3.5: Standard deviation of the Y values with respect to the curve fit vs the empirical coefficient n .

Lunde and Kester [115] reported in their work an interval of values for n with a minimum standard deviation of 0.1532 which generated reasonable correlations to their experimental data. The value of n reported by these authors is 0.225. Regarding the experimental

3. Modelling

data obtained in the PtG lab, no interval was found, a minimum value for the standard deviation of 0.3046 and a value for n of 0.52 were determined. The results are depicted in *figure 3.6*. Where, Y is the natural logarithm of the quantity defined in equation (3.67).

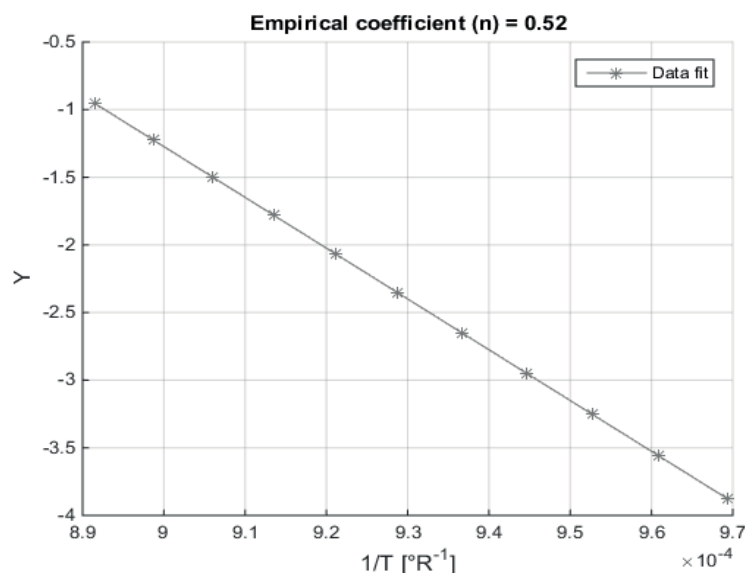


Figure 3.6: Y vs the inverse of the reactor mean temperature. Experimental data used to determine the activation energy of the Ru-based catalyst in the reactor.

After following the methodology described above and determining the value of n , values for Ea and A of 74567 btu/lb mol CO_2 (173.43 kJ/mol) and $0.1975 \times 10^{15} \text{ hr}^{-1} \text{ atm}^{-1.6}$ ($3.777 \times 10^{11} \text{ mol}^{-0.52} \text{ m}^{-1.56} \text{ sec}^{-1}$) were respectively found. As it can be seen in *figure 3.6* and *figure 7.5* in the *appendix*, the values of Y are too scattered if they are compared with the data found in the literature (*figure 3.2*) i.e. the standard deviation of the experimental data to the fit is greater than those reported by Lunde and Kester [4]. These results are attributed to the non-isothermal operation of the reactor which is caused by its size, since its temperature is controlled and set by the control strategy as the mean value of seven thermocouples along the reactor. In *figure 3.7*, a comparison is presented between the values reported in the literature and those obtained in the PtG lab.

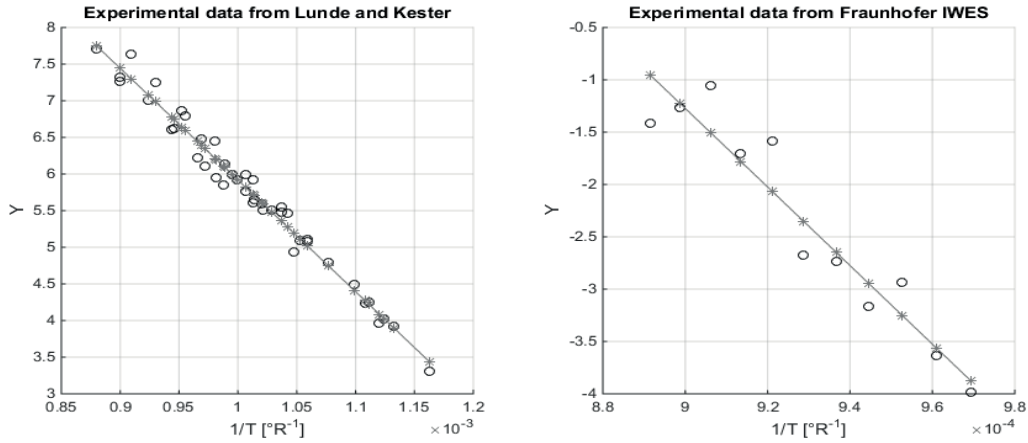


Figure 3.7: Y vs the inverse of the reactor mean temperature. *Left*: Experimental data found by Lunde und Kester [4]. *Right*: Experimental data used to determined the activation energy of the Ru-based catalyst in the reactor.

3.4 Spatial discretisation

For the spatial discretisation of the reactor model, equally spaced control volumes in the direction of flow are defined. The state variables (ρ, Y_k, u, T) are computed at the nodes x_n , whereas the inlet and outlet boundary conditions are model parameters that are defined and can vary during the simulation. *Figure 3.8* illustrates the discretisation of the reactor spatial coordinate.

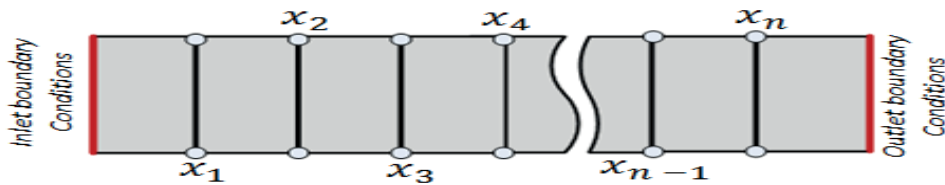


Figure 3.8: Discretisation of the spatial coordinate.

The first and second order spatial derivatives are computed for every time iterations and defined as follows:

$$\frac{\partial f}{\partial x} = \frac{f(x_{n+1}) - f(x_n)}{x_{n+1} - x_n} \quad (3.89)$$

$$\frac{\partial^2 f}{\partial x^2} = \frac{f(x_{n+1}) - 2f(x_n) + f(x_{n-1}))}{(x_{n+1} - x_n)^2} \quad (3.90)$$

Once the partial differential equations are discretised, a system of ordinary differential equations which depends on time is solved with one of the built-in Simulink solvers. Fur-

3. Modelling

thermore, an optimisation regarding the number of segments was carried out by analysing how much the estimated volumetric percentage of CH₄ changed with the number of segments. As it can be seen in *figure 3.9* the optimum number of segments found was 40. This is the smallest number of segments within a tolerance of $\pm 1.0\%$.

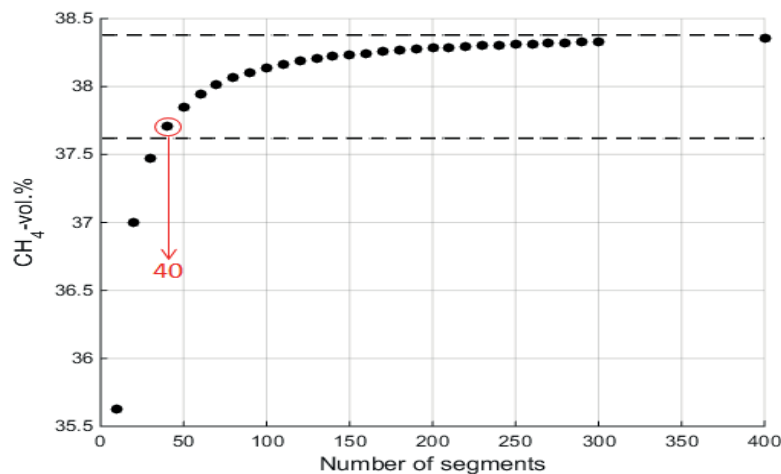


Figure 3.9: Optimum number of segments.

3.5 Model structure and simulation environment

3.5.1 Model structure

The reactor model has as inputs initial, boundary conditions of the gas phase as well as reactor and reaction parameters. As outputs, the density, species mass fractions, velocity, temperature and pressure of the gas phase are computed, the model structure is depicted in *figure 3.10*.

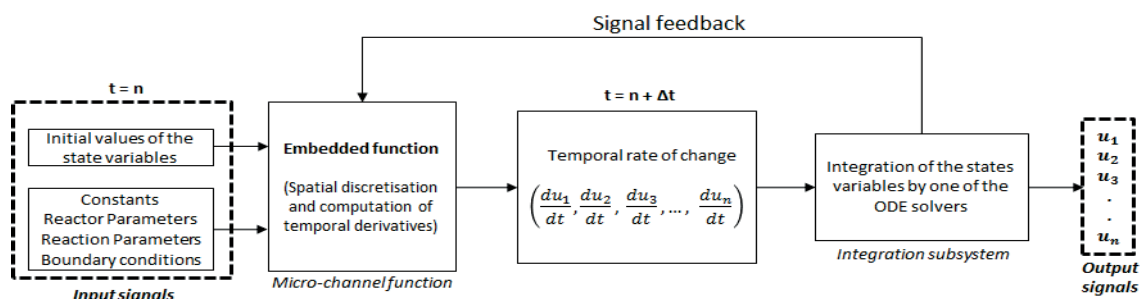
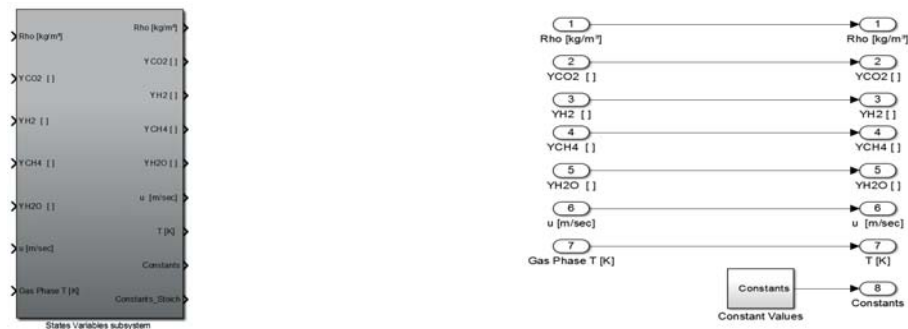


Figure 3.10: Structure of the Matlab-Simulink model

3.5.2 Simulation environment

The simulation environment was assembled in Matlab-Simulink®. It consists of two simulink subsystems, (*state variables* and *integration*) as well as one embedded-function (*microchannel function*). *State variables* subsystem contains the values of the state variables and constant values such as reaction, reactor and species-dependent parameters as well as inlet and outlet boundary conditions as shown in *figure 3.11a* and *3.11b*. The out-



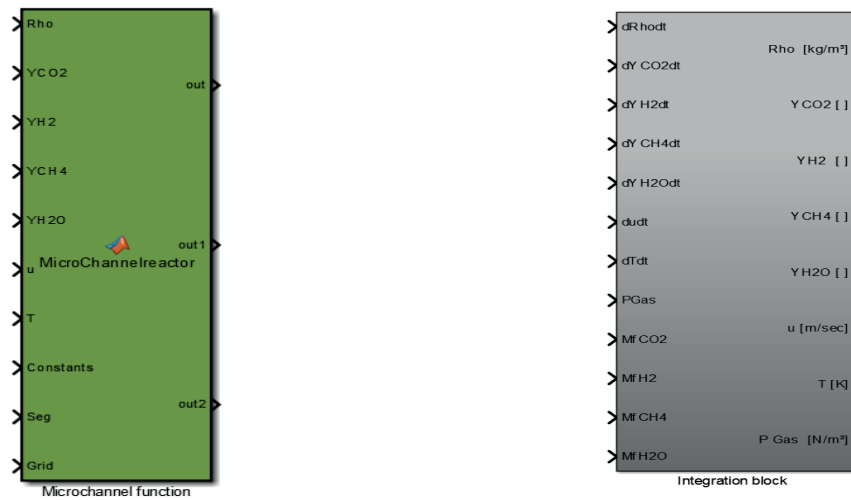
(a) Subsystem state of variables

(b) Subsystem inputs and outputs

Figure 3.11: Subsystem state of variables (graphical representation)

puts of this subsystem are conveyed to the *microchannel function* (*figure 3.12a*) where the temporal derivatives of the state variables (*equation 3.23, 3.27, 3.44 and 3.53*) are computed. The value of the state model state variable is obtained by integrating the temporal derivatives and this takes place in the *integration* subsystem (*figure 3.12b*). Subsequently, the outputs of the integration subsystem are fed back as inputs of the *state variables* subsystem thus the temporal derivatives for the next time step are computed.

3. Modelling



(a) Microchannel embedded function

(b) Integration subsystem

Figure 3.12: Micro-channel function and integration Subsystem

Figure 3.13 depicts structure of the integration subsystem. The temporal derivatives of the density, species mass fraction, velocity, temperature of the gas phase are integrated through integrator blocks whereas the gas phase pressure is considered to be constant.

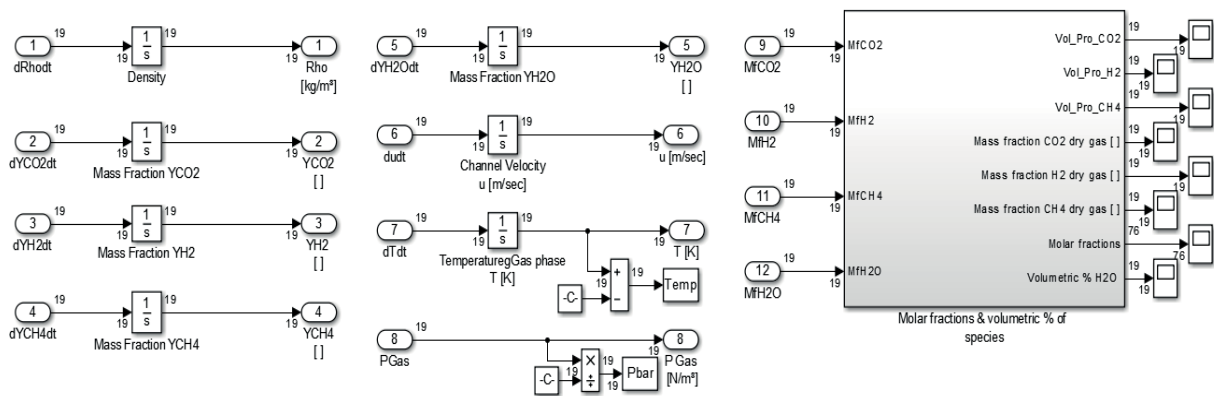


Figure 3.13: Structure of the integration subsystem

The species mole fractions are calculated as follows:

$$X_k = \frac{Y_k \bar{W}}{W_k} \quad (3.91)$$

Where \bar{W} stands for the average molecular weight of the gas mixture (equation 3.92). Figure 3.14 shows the structure of the simulation environment.

$$\bar{W} = \frac{\rho RT}{P} \quad (3.92)$$

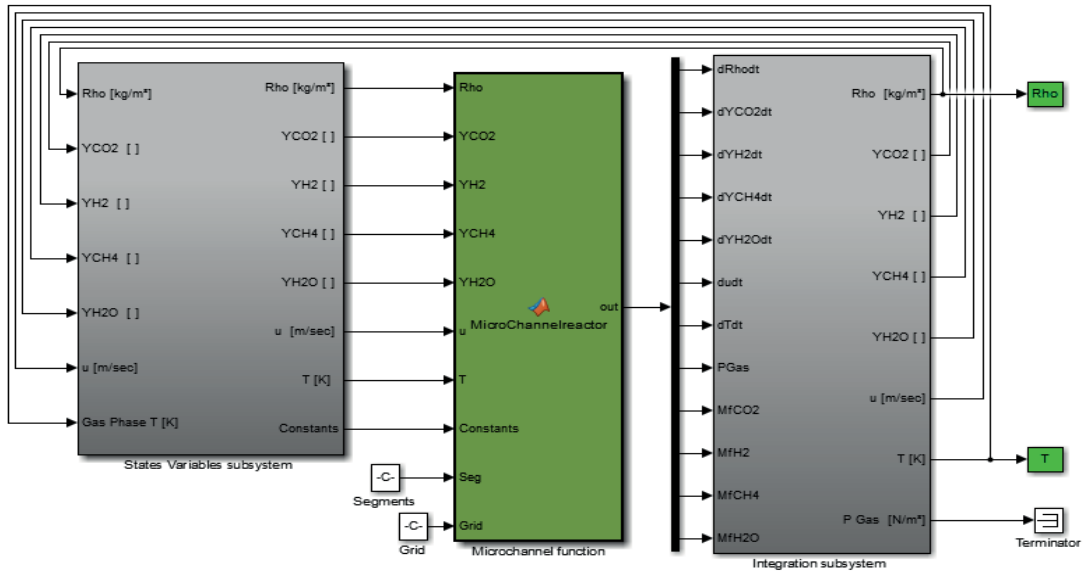


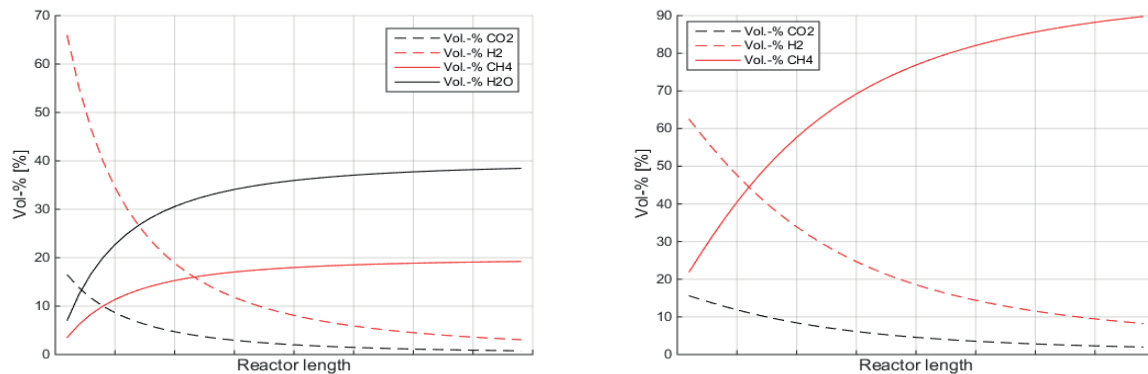
Figure 3.14: Simulation environment programmed in Matlab-Simulink

3.5.3 Model results

This subsection presents the temporal profiles of the volumetric percentages at the reactor outlet for CH₄, CO₂ and H₂. The effect of the temperature, pressure and inlet volumetric flow of educt gas on the outlet volumetric percentage of these gas species is analysed and discussed. To analyse the effect of the temperature, a determined pressure and different channel wall temperatures were set as model parameters, whereas the effect of the pressure was analysed by setting a determined channel wall temperature and varying the reactor operating pressure, the value of the inlet volumetric flow of educt gas was set to 1.0 Nm³/h for both analysis. The analysis of the inlet volumetric flow of educt gas was analysed by carrying out different simulations in which the volumetric flow was varied as a model parameter. Additionally, for this case a determined channel wall temperature and pressure were set as parameters in the reactor model as well. In all the aforementioned cases, the

3. Modelling

gas composition of educt gas had the following volumetric proportion: 4:1 with respect to H_2 and CO_2 and 1:1 with respect to CO_2 and CH_4 . *Figure 3.15a and 3.15b* show the estimated volumetric percentage of the gas components along the reactor length for an inlet volumetric flow of $1 \text{ Nm}^3/\text{h}$ and $350 \text{ }^\circ\text{C}$.



(a) Vol.-% of CO_2 , H_2 , CH_4 and H_2O . Inlet composition of the mixture: 80% H_2 , and 20% CO_2

(b) Vol.-% of CO_2 , H_2 , CH_4 . Inlet composition of the mixture: 66.6% H_2 , 16.6% CO_2 and 16.8% CH_4

Figure 3.15: Vol.-% of the gas components along the reactor length; Inlet volumetric flow $1 \text{ Nm}^3/\text{h}$ and $350 \text{ }^\circ\text{C}$.

3.5.3.1 Temperature effect on the CH_4 , CO_2 and H_2 outlet volumetric percentage

In order to analyse the effect of the temperature on the CH_4 , CO_2 and H_2 volumetric percentage, simulations were carried out setting a constant channel wall temperature of 200, 225, 250, 275, 300, 325, 350 $^\circ\text{C}$ and a pressure of 15 bar, the estimated volumetric concentration of CH_4 is shown in *figure 3.16*.

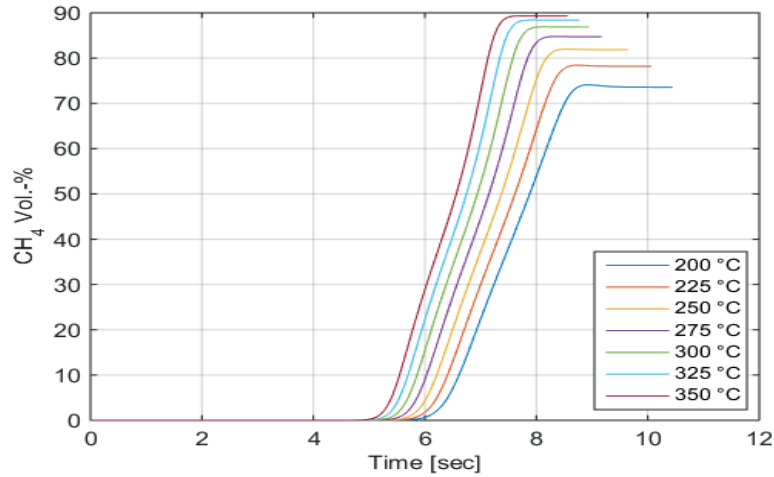


Figure 3.16: Temperature effect on the CH₄ outlet volumetric percentage. 1 Nm³/h inlet volumetric flow of educt gas, 15 bar reactor operating pressure.

Figure 3.16 depicts the temporal profile of the CH₄ volumetric percentage at the temperatures specified above. An increase in the CH₄ volumetric percentage in steady state can be seen as the reactor wall temperature increases e.g. 73.6% was estimated at a reactor wall temperature of 200 °C whereas at a 350 °C the highest concentration (89.3%) was estimated. This is explained by the temperature dependency of the reaction kinetics i.e. an increase in the temperature accelerates the kinetics of the *Sabatier* reaction and this leads to higher CO₂ conversion rates and CH₄ volumetric percentages.

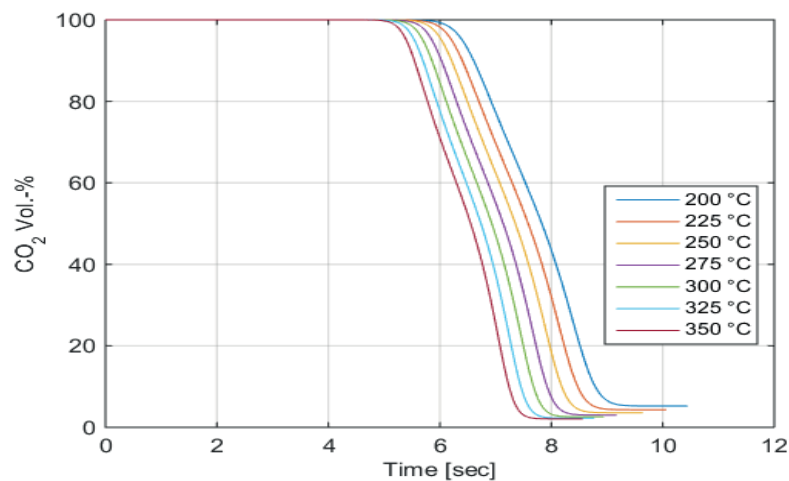


Figure 3.17: Temperature effect on the CO₂ outlet volumetric percentage. 1 Nm³/h inlet volumetric flow of educt gas, 15 bar reactor operating pressure.

3. Modelling

Figure 3.17 shows the temporal profile of the CO₂ volumetric percentage at the temperatures specified above. The CO₂ volumetric percentage in steady state decreases as the reactor wall temperature increases e.g. 5.2% was estimated when the reactor wall temperature was set to 200 °C, a simulation in which the reactor wall temperature was set to 350 °C, estimated a CO₂ volumetric percentage of 2%. This corroborates the previous statement regarding the reaction kinetics and its temperature dependency. In figure 3.17 can also be seen that the initial CO₂ volumetric percentage is equal to 100%, this is due to the fact that during the experimental runs only CO₂ was fed into the reactor in order to set the operating pressure before the reaction began.

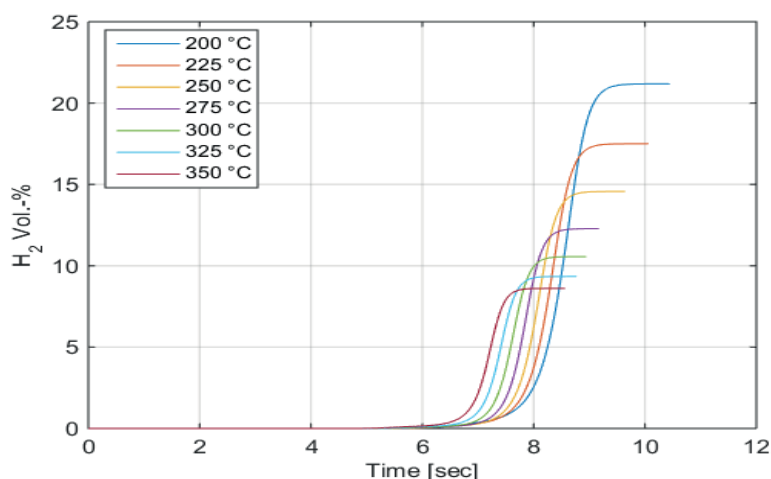


Figure 3.18: Temperature effect on the H₂ outlet volumetric percentage. 1 Nm³/h inlet volumetric flow of educt gas, 15 bar reactor operating pressure.

Figure 3.18 shows the temporal profile of the H₂ volumetric percentage for the temperatures specified above. It can also be seen that higher reactor wall temperatures lead to higher H₂ conversions in steady state e.g. simulations in which the reactor wall temperature was set to 200 °C, estimated a H₂ volumetric percentage of 21.2%, whereas, 8.6% was estimated when the reactor wall temperature was set to 350 °C.

3.5.3.2 Pressure effect on the CH₄ CO₂ and H₂ outlet volumetric percentage

The effect of the reactor pressure on the CH₄, CO₂, and H₂ volumetric percentage was analysed by carrying out simulations where the gas-phase pressure was set to 7, 9, 11, 13, and 15 bar. In all simulations the reactor wall temperature was set to 350 °C and the inlet volumetric flow of educt gas was set to 1 Nm³/h. Figure 3.19 depicts the temporal

profile of the CH_4 volumetric percentage for the pressures mentioned above. It can be seen that an increase in the gas-phase pressure leads to higher CH_4 volumetric percentages in steady state e.g. a CO_2 volumetric percentage of 65.4% was estimated at 7 bar whereas 89.3% was estimated at 15 bar. An increase in pressure displaces the equilibrium of the *Sabatier* reaction towards product formation, moreover the gas molecules can reach easier the catalyst active sites.

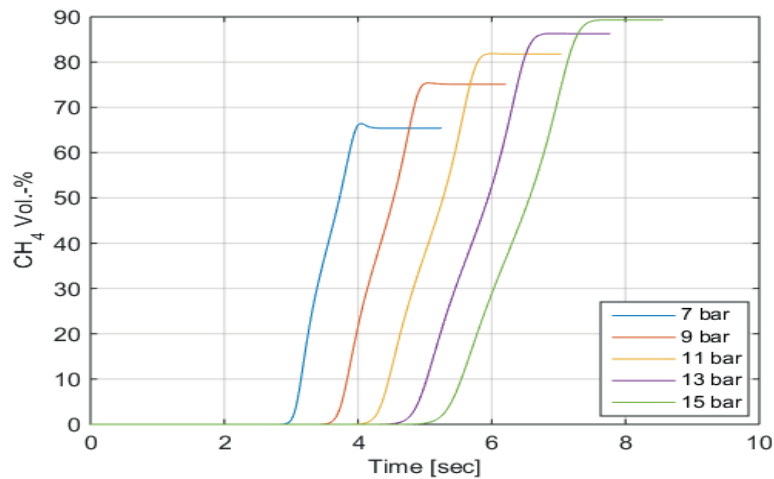


Figure 3.19: Pressure effect on the CH_4 outlet volumetric percentage. 1 Nm^3/h inlet volumetric flow of educt gas, 350 °C reactor wall temperature

Figure 3.20 shows the temporal profile of the volumetric percentage of CO_2 for the pressures mentioned above. As it is expected, the volumetric percentage of CO_2 in steady state decreases when the pressure increases as a consequence of the reaction nature. For instance, a CO_2 volumetric percentage of 6.9% was estimated for an operating pressure of 7 bar, whereas a CO_2 volumetric percentage of 2.1% for an operating pressure of 15 bar.

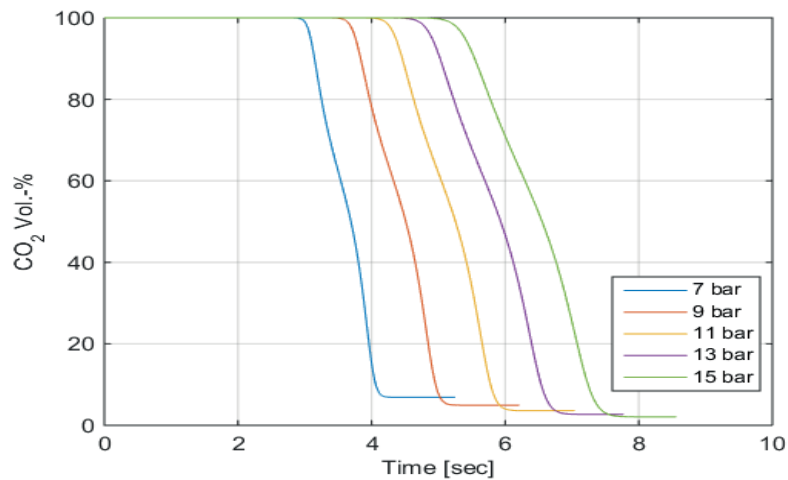


Figure 3.20: Pressure effect on the CO₂ outlet volumetric percentage. 1 Nm³/h inlet volumetric flow of educt gas, 350 °C reactor wall temperature

A similar behaviour can be observed for the case of the H₂ volumetric percentage in *figure 3.21* which depicts the temporal profile for the pressures mentioned above. According to the simulations, 27.7% was estimated at a pressure of 7 bar whereas 8.6% was estimated at 15 bar.

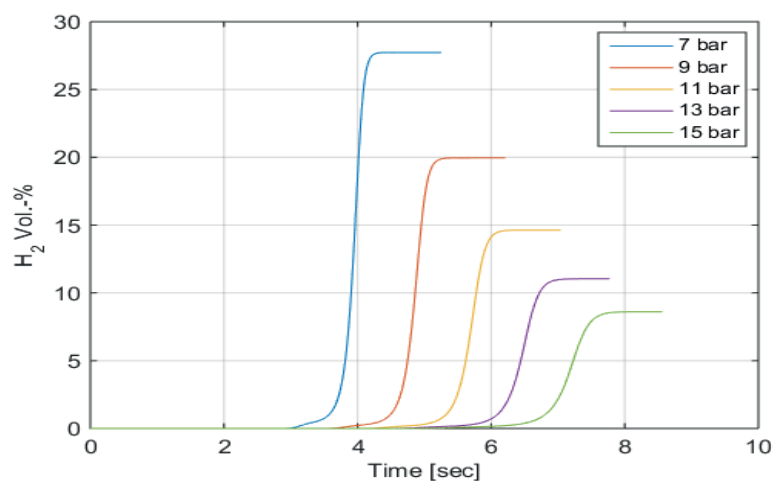


Figure 3.21: Pressure effect on the H₂ outlet volumetric percentage. 1 Nm³/h inlet volumetric flow of educt gas, 350 °C reactor wall temperature

3.5.3.3 Effect of the inlet volumetric rate on the CH₄, CO₂ and H₂ outlet volumetric percentage

To analyse the effect of the inlet volumetric flow of educt gas on the CH₄, CO₂ and H₂ outlet volumetric percentage, simulations were carried out for 0.75, 1.0 and 1.5 Nm³/h. For all simulations, the channel wall temperature and pressure were set to 350 °C and 15 bar as model parameters. *Figure 3.22* shows the temporal profile of the CH₄ volumetric percentages for the inlet flows mentioned above. It can be seen that higher inlet volumetric flows lead to lower CH₄ volumetric percentages in steady state due to shorter residence times of the educt gas. For instance, 89.3% was estimated for a volumetric flows equals to 1 Nm³/h whereas, 83.1% was estimated for an inlet volumetric flow of 1.5 Nm³/h.

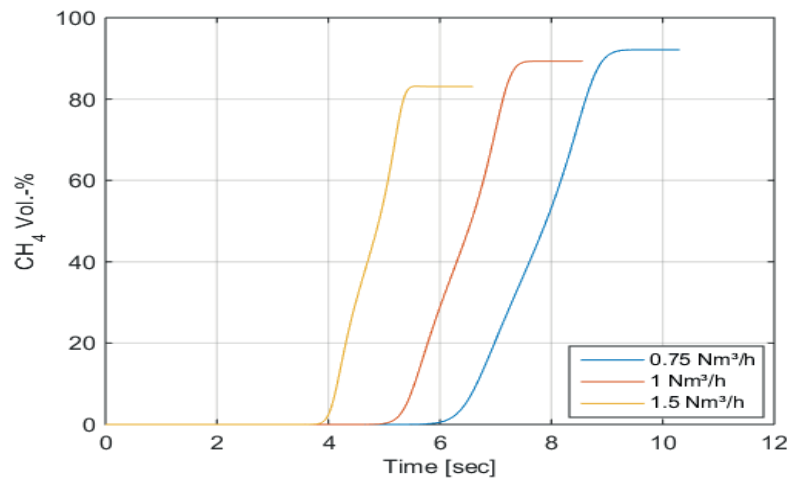


Figure 3.22: Effect of the inlet volumetric flow on the CH₄ outlet volumetric percentage. 350 °C reactor wall temperature and 15 bar operating pressure.

Figure 3.23 shows the temporal profile of the CO₂ outlet volumetric percentage for the inlet flows mentioned above. The simulation shows higher CO₂ volumetric percentages as the inlet flow increases which is consequent with the tendency shown by CH₄. For instance, 2.1% was estimated when the inlet flow was set to 1 Nm³/h, whereas 3.3% was estimated for an inlet flow of 1.5 Nm³/h.

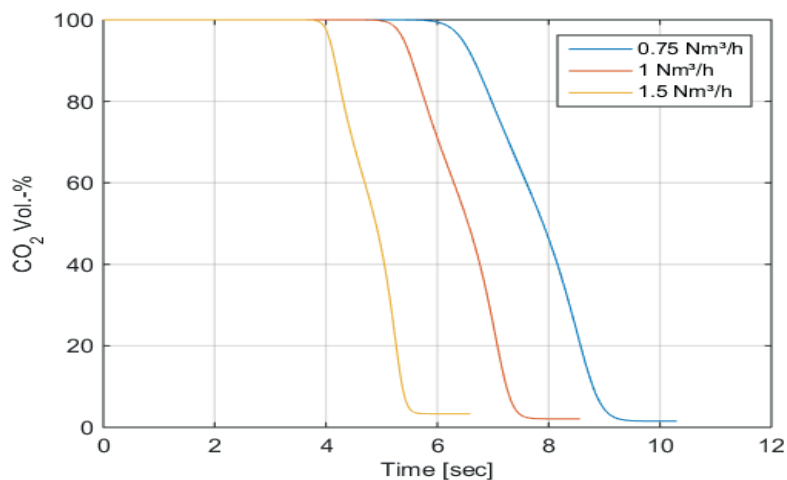


Figure 3.23: Effect of the inlet volumetric flow on the CO₂ outlet volumetric percentage. 350 °C reactor wall temperature and 15 bar operating pressure.

Figure 3.24 shows the temporal profile of the H₂ volumetric percentage for the inlet flows mentioned above. The simulation shows higher H₂ volumetric percentages as the inlet flow increases which is consequent with the tendency shown by CH₄ and CO₂. For instance, 8.6% was estimated when the inlet flow was set to 1 Nm³/h, whereas 13.6% was estimated for an inlet flow of 1.5 Nm³/h.

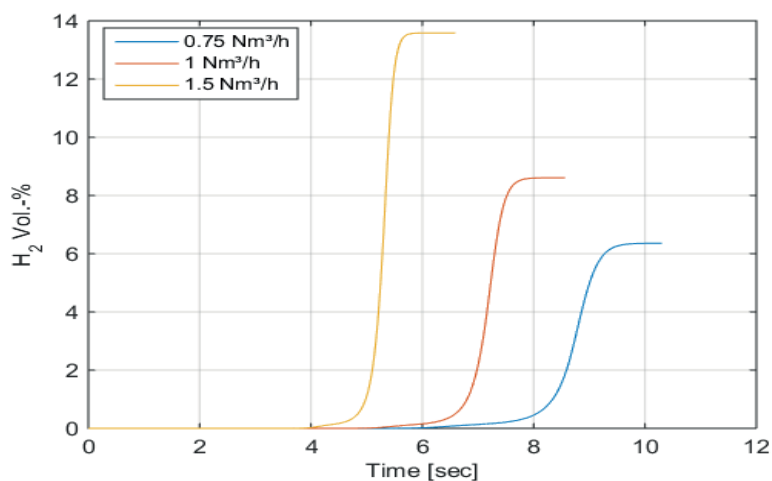


Figure 3.24: Effect of the inlet volumetric flow on the H₂ outlet volumetric percentage. 350 °C reactor wall temperature and 15 bar operating pressure.

3.6 Control strategy and the reactor model

The operation of the lab-scale PtG plant was ensured through a control strategy programmed in C++. Different operating states were defined in the control strategy i.e. according to the state, different instructions are transmitted to the software and then specific actions are carried out by the actuators in the system. The transition between states is achieved by checking certain logical conditions which determine whether to change state or not. This program is run each 10 ms in a Beckhoff PLC. Additionally, the real-time signals of the system can be visualised through graphical interfaces. In case of a system failure, the process is interrupted and the shut-down of the system is triggered by the control strategy [124]. *Figure 3.25* shows the states which were defined for the operation of the lab-scale PtG plant.

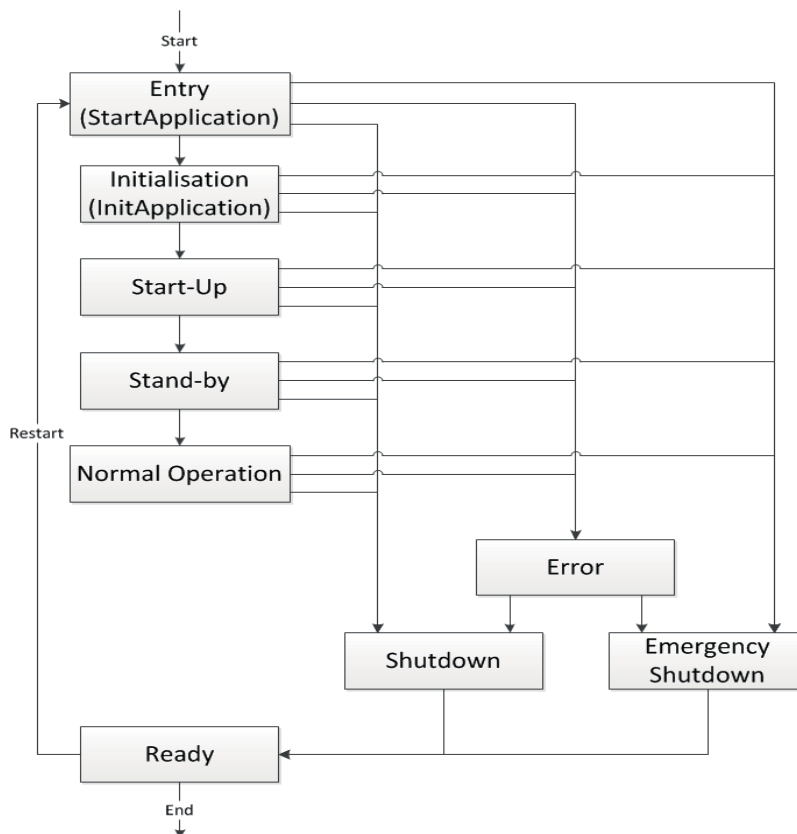


Figure 3.25: State machine

[124]

3.6.1 Reactor model as state observer

A state observer is a computer tool which is used in control strategies to estimate indirectly the internal state of a real plant based on its inputs and outputs. Normally, the state of the system of interest depends on some variables which cannot be measured. Moreover, model simplifications are commonly implemented as a way to optimise calculation times. The state of a system of interest can be described by its known inputs and unknown disturbances as shown in equation 3.93.

$$q[t + 1] = Aq[n] + bx[n] + w[n] \quad (3.93)$$

Where, the term $q[n]$ denotes the system state, $x[n]$ represents the known input(s) and $w[n]$ denotes the unknown system disturbances. The known or measured output(s) of the system $y[n]$ are described in equation (3.94), the term $\zeta[n]$ represents the measurement noise [125].

$$y[n] = c^T q[n] + dx[n] + \zeta[n] \quad (3.94)$$

The reactor model is going to be used as an state observer for a larger PtG plant. It will be integrated in a control strategy in order to monitor the performance of the *Sabatier reactor*, more specifically the real-time CH₄ outlet volumetric percentage will be compared to the model estimate at specific operating conditions (temperature, pressure and inlet volumetric percentage of educt gas). However, the model needs to be linearised due to the fact that it consists of non-linear partial differential equations which do not allow a simulation in real time.

4 PtG lab-scale plant

This chapter describes the components of the PtG plant which was operated in order to carry out the reactor experimental runs. The PtG lab-scale plant consists of two components, the gas supply and the methanation unit. Since a reactor warmup and cooling is required during the startup and shutdown state respectively, a heat exchange between an electric heater (during the reactor warmup), water (during the reactor cooling) and a thermal coolant took place. Gas samples of the product stream were taken in steady state operation and sent to a lab in order to determine their composition. See *appendix 7* for a better understanding of the structure and functioning of the PtG plant.

4.1 Gas supply

The gas supply consisted of standard pressurised bottles of CO_2 , CH_4 , H_2 and N_2 . The gas mixture was adapted in order to emulate a biogas plant and the electrolyser. N_2 was used to purge the plant. The gas bottles were placed inside three special cabinets for security reasons. CH_4 , H_2 and N_2 were stored at 200 bar, whereas CO_2 was stored at 60 bar. In order to achieve the desire composition of the educt gas, mass flow controllers manufactured by Bronkhorst[®] were installed as shown in *figure 4.1b*.



(a) Security cabinets



(b) Mass flow controllers

Figure 4.1: Gas supply [126].

A set of pressure reducers manufactured by IBEDA were integrated between each gas bottle and the mass flow controllers in order to set the working pressure of the plant. The educt gas was then directed to the reactor through a stainless steel pipeline c.a. 10 m long. *Figure 4.2* shows a graphical representation of the pressure reducers.

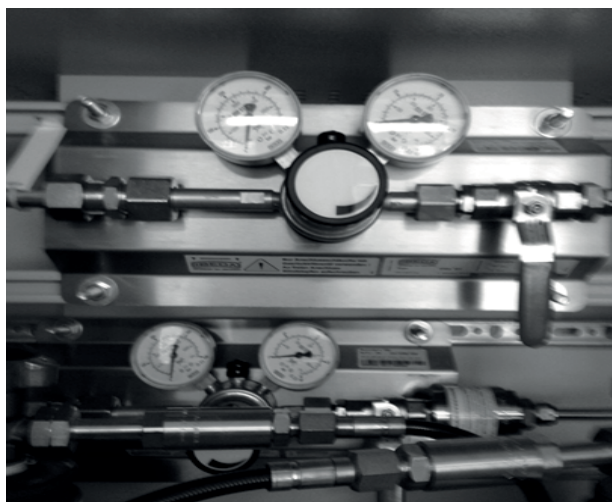


Figure 4.2: Pressure reducers

4.2 Methanation

The methanation, consisted of a micro-channel reactor with counter-flow heat exchanging properties. The reactor was manufactured by Fraunhofer ICT-IMM and consisted of two stacks, the distributing and reacting stack. Moreover, the reactor was equipped with 4 electric heaters (each of them with a rated power of 300 W) for start-up purposes. The distributing stack ensured a homogeneous distribution of the educt gas in the reactor channels, whereas in the reacting stack the *Sabatier* reaction took place. The reacting stack consisted of two different types of platelets, those which were in contact with the educt gas and those which were in contact with the thermal coolant. The first type of platelet had a width of 1 mm, a height of 0.7 mm, a length of 130 mm and were coated with Ru-based catalyst layer (80 μm -thick). The second type of platelet had a width of 0.3 mm, a height of 0.3 mm and a length of 99 mm. The reacting stack was made of 70 platelets (35 in contact with the educt gas and 35 with the thermal coolant), 40 micro-channels were etched on each platelet [127]. In order to avoid thermal a mechanical stress of the material, the reactor could not be heated up or cooled with a velocity greater/lower

than ± 15 °C/min and the pressure difference between the reacting and cooling side could not exceed 2 bar.

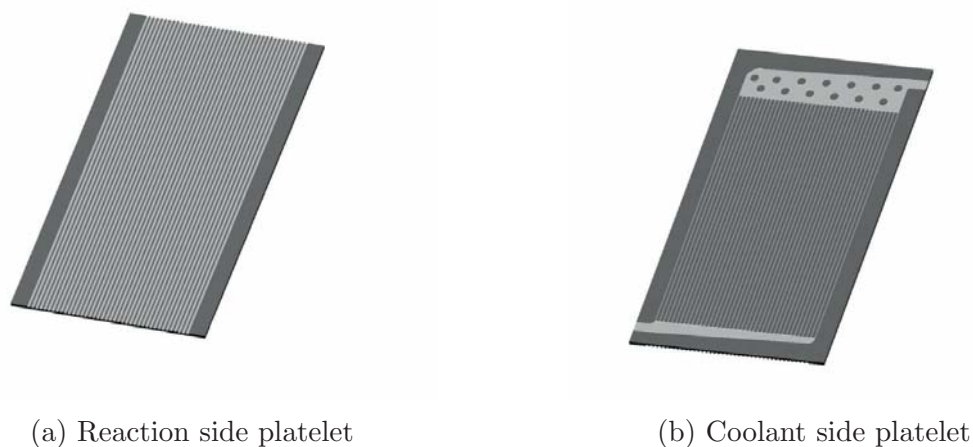


Figure 4.3: Type of platelets in the reacting stack [128].

Figure 4.3a illustrates a platelet in contact with the educt gas. Whilst, *figure 4.3b* illustrates the type of platelet which is in contact with the thermal coolant. *Figure 4.4a* illustrates how the reacting stack was manufactured, a counter-flow between the educt gas and the thermal coolant can be seen.

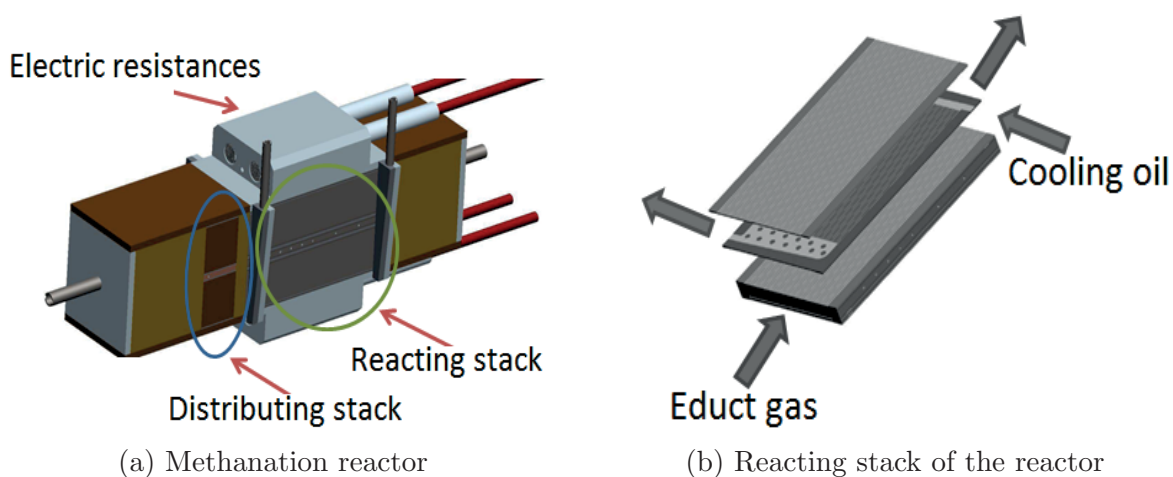


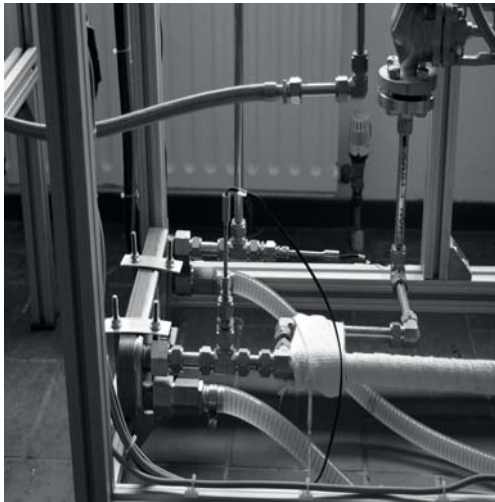
Figure 4.4: Methanation reactor and its reacting stack [128].

A periphery which allowed the flow and heat transfer of the thermal coolant, reactor, electric heater, heat exchanger and water was also part of the PtG lab plant. During the start-up process, the coolant was heated up through a micro-channel electric heater with a rated power of 2.4 kW which was manufactured by Fraunhofer ICT-IMM. Thereby,

heat was transferred from the thermal coolant to the Sabatier reactor thus the operating temperature could be reached. In order to cool the methanation reactor, during the shut-down process part of the thermal coolant was directed to a plate heat exchanger by the means of the three-way valve. The plate heat exchanger operated at atmospheric pressure and ambient temperature. This part of the lab-scale PtG plant can be divided as follows:

- *Thermal coolant* which consisted of a heat transfer fluid manufactured by FRAGOL GmbH + Co. KG, the thermal coolant could be used between 10 - 380 °C and it had a boiling point of 271 °C at atmospheric pressure. Heat recovery from flue gas, indirect heating of chemical processes and cooling of exothermic reactions are examples of its applications.
- *Circulating pump* with a motor rated power of 0.5 kW and a maximum volumetric flow of 30 l/min.
- *Plate heat exchanger* manufactured by Lytrons[®] with a performance of 16 kW. It was made of 10 stainless steel plates which can operate in a temperature range of -195 to 350 °C and it could withstand a maximum operating pressure of 31.5 bar.
- *Three-way valve*, used to create a by-pass between plate heat exchanger and the Sabatier reactor during the shutdown state.

Figure 4.5a and *figure 4.5b* show the plate heat exchanger and the three-way valve that were implemented during the shut-down process of the lab-scale PtG plant. Additionally, *figure 4.6* shows the circulating pump used to circulate the thermal coolant.



(a) Plate heat exchanger



(b) Three-way valve

Figure 4.5: Plate heat exchanger and three-way valve

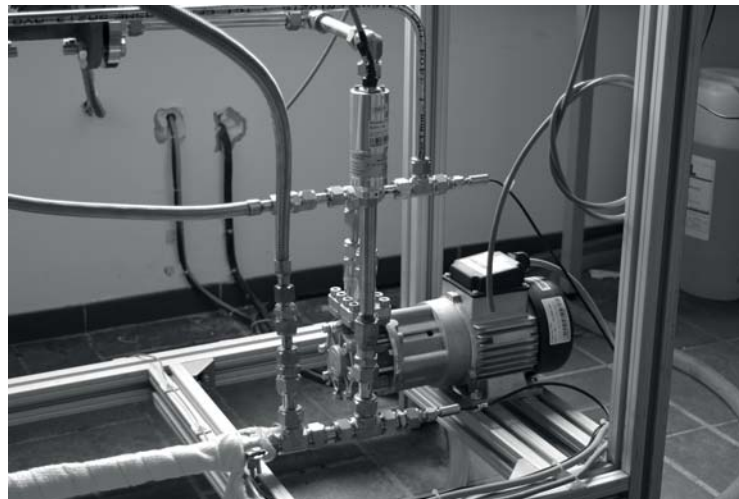


Figure 4.6: Pump

4.3 Technique of measurement

For the measuring of the product gas, an analyser manufactured by Sensors Europe was implemented. Before analysing the composition of the product gas, water vapour was condensed. However accurate measurements were not possible to be taken because the sensors showed species cross-sensitivity. Consequently, gas samples which contained the product gas were taken and analysed at SGS INSTITUT FRESENIUS GmbH. Tedlar and multi-

layer polypropylene bags with a maximum capacity of 1 L were used for such a purpose. Moreover, samples of the educt gas were as well taken and analysed in order to calibrate the mass flow controllers. Later on in the project, a micro gas chromatograph manufactured by Agilent was integrated into the PtG plant in order to compare the measurements of the gas analyser (Sensors Europe) and correct the species cross-sensitivity. The gas chromatograph consisted of four independent column channels which have a micro-machined injector, carrier gas control, an analytical column and a micro thermal conductivity detector (μ TCD) which detects the difference between a reference cell (gas carrier only) and a measurement cell (gas carrier with components) [129]. Argon was used as gas carrier for channel 1, whereas Helium was used for channel 2, 3, 4. Channel 1 consisted of a molsieve 5Å column, it is designed to separate permanent gases, methane, CO, NO, among others and it was used in this case to measure H₂. Channel 2 likewise consisted of a molsieve 5Å column, it is designed to separate O₂, N₂, CH₄, and CO. However, in this case only CH₄ was measured on this channel. Channel 3 consisted of a PoraPLOT U column, it is designed to separate Hydrocarbons C₁–C₆, halocarbons/freons, anesthetics, H₂S, CO₂, SO₂, volatile solvents, ethane, ethylene, and acetylene. In this case, only CO₂ was measured on this channel. Channel 4 consisted of a PlotAl₂O₃/KCL column which is designed to separate light hydrocarbons C₁–C₅ saturated and unsaturated, this channel was used to measure propane [129]. A graphical representation of the micro gas chromatograph is depicted in *figure 4.7*.

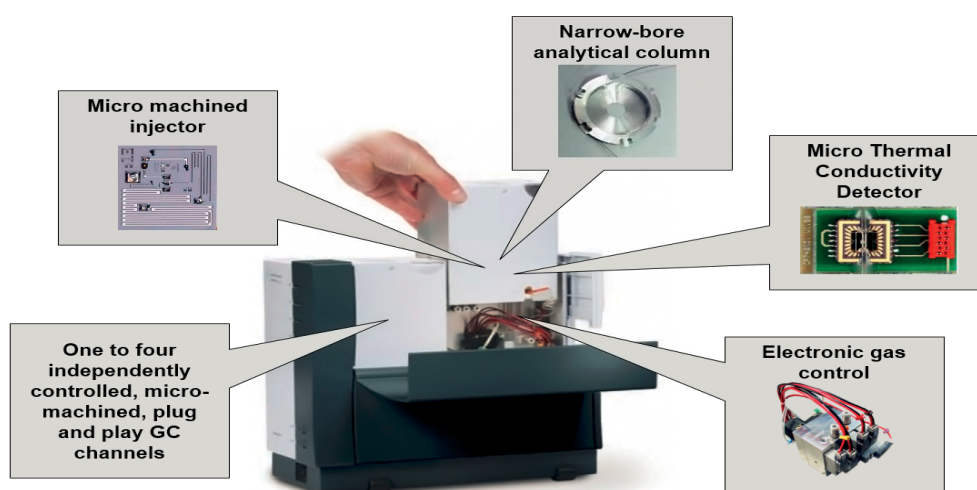


Figure 4.7: Overview of the micro gas chromatograph [129].

5 Experimental set-up and results

The methanation reaction was tested for four different inlet volumetric flows of educt gas (0.25, 0.50, 0.75 and 1.0 Nm³/h) which correspond to the 25%, 50%, 75% and 100% of the reactor nominal capacity. For these inlet volumetric flows, the temperature and pressure of the reactor were set to 350 °C and 15 bar. *Figure 5.1* shows the estimated, measured and equilibrium volumetric percentage of CH₄ for the aforementioned operating points. The measured data show a CH₄ volumetric percentage of 75, 52.6, 44 and 36.6 for the four

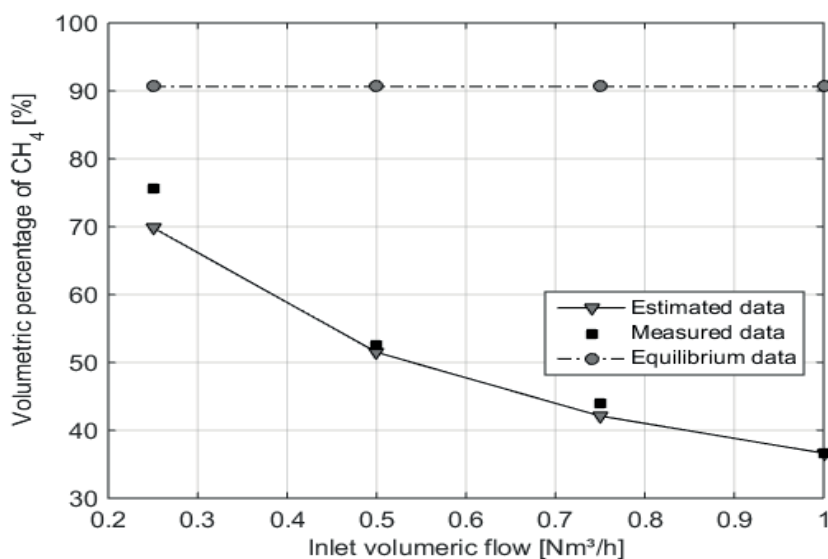


Figure 5.1: Measured, estimated and equilibrium concentration of CH₄. Operating conditions: 350 °C, 15 bar, 0.25, 0.50, 0.75 and 1.0 Nm³/h.

variations of the inlet volumetric flow. As the inlet volumetric flow increases, a decrease in the volumetric percentage of CH₄ is expected due to the fact that the residential time of the gas mixture in the reactor increases and therefore the reaction time is reduced. The model estimates a CH₄ volumetric percentage of 69.84, 52.6, 42.12 and 36.6 for the four variations of the inlet volumetric flow which corresponds to an absolute error of 4, 0.8, 1.6 and 0.03 between the estimated and measured data. Moreover, the equilibrium volumetric

5. Experimental set-up and results

percentage of CH₄ (90.63) for the specified temperature and pressure conditions was not reached by the reactor during the experiments, the possible reasons are discussed in chapter 6.

6 Discussion

A mathematical model consisting of partial differential equations which describe the performance of a micro-channel *Sabatier* reactor was programmed in Matlab-Simulink. In order to compare the estimated and measured data, the *Sabatier* reactor was operated at 350 °C, 15 bar and four inlet volumetric flows were considered for the experiments (0.25, 0.50, 0.75 and 1.0 Nm³/h), an inlet gas composition of 4:1 regarding H₂/CO₂ and 1:1 regarding CO₂/CH₄ was set by the mass flow controllers of the lab-scale PtG plant, the product gas was sent to SGS INSTITUT FRESENIUS GmbH for its analysis. The highest volumetric percentage of CH₄ was achieved at an inlet volumetric flow of 0.25 Nm³/h and corresponded to 75.6% which means that equilibrium values for these experimental conditions were not reached. Additional experimental runs were carried out in the lab in order to determine the kinetic parameters A , E_a and n . Values of $0.1975 \times 10^{15} \text{ hr}^{-1} \text{ atm}^{-1.6}$ for A , 74567 btu/lb mol CO₂ for E_a and 0.52 for n were found, Lunde and Kester [114] found lower values for E_a , A and n (30320 btu/lb mol, $0.1769 \times 10^{10} \text{ hr}^{-1} \text{ atm}^{-0.125}$ and 0.225).

The mathematical model described well the dependency of the outlet volumetric percentages of the gas components in regard to temperature, pressure and inlet volumetric flow. During the simulations, it was observed that for some segments the sum of the mass fractions do not sum to one. The same issue was reported by Kee et al. [112] when it was discussed that the mixture formulas are approximations and that there is no constrain which ensures that the net species diffusion flux is zero. Consequently the use of equation (3.35) may lead to some nonconservation. Additionally, Kee et al. [112] explained that the resolution of the conservation problem requires detailed knowledge of the specific problem, discretisation method and that no generic solution can be given. It also is important to mention that further calibration of the mathematical model which considers more operating points i.e. different temperatures, pressures and volumetric flows needs to be carried out in order to have better estimates of the reactor performance.

Finally, during the experiments a decrease in the volumetric percentage of CH_4 was observed throughout the time. A *post mortem* analysis will be carried out at Fraunhofer-Institut ICT-IMM in order to determine whether catalyst deactivation took place; if it is the case, the exact deactivation mechanism will be identified and the catalyst will be reactivated to regain nominal capacity of the *Sabatier* reactor.

Bibliography

- [1] Bundesministerium für Wirtschaft und Energie. Das erneuerbare-energien-gesetz 2014. die wichtigsten fakten zur reform des eeg. Technical report.
- [2] Julia Michaelis, Julian Junker, and Martin Wietschel. Eine bewertung der regelen-ergievermarktung im power-to-gas-konzept. *Zeitschrift für Energiewirtschaft*, 2013.
- [3] Siegfried Bajohr, Manuel Götz, Frank Graf, and Felix Ortloff. Speicherung von regenerativ erzeugter elektrischer energie in der erdgasinfrastruktur. Technical report, DVGW-Forschungsstelle am Engler-Bunte-Institut des Karlsruher Instituts für Technologie (KIT), 2011.
- [4] Peter J. Lunde and Frank L. Kester. Rates of methane formation from carbon dioxide and hydrogen over a ruthenium catalyst. *Journal of catalysis*, 30(3):423–429, 1973.
- [5] Mareike Jentsch. *Potenziale von Power-to-Gas Energiespeicher. Modellbasierte Analyse des markt- und netzseitigen Einsatzes im zukünftigen Stromversorgungssystem*. PhD thesis, Elektrotechnik/Informatik der Universität Kassel, 2014.
- [6] Aktionsprogramm klimaschutz 2020. Technical report, Bundesministerium für Umwelt, Naturschutz, Bau und Reaktorsicherheit, 2014.
- [7] Joachim Nitsch. ”szenario 2013” - eine weiterentwicklung des leitszenarios 2011 (eckdaten und kurzbeschreibung). Technical report, BMU, 2013.
- [8] Kaspar Knorr, Britta Zimmermann, Dirk Kirchner, Markus Speckmann, Raphael Spieckermann, Martin Widdel, Manuela Wunderlich, Reinhard Mackensen, Kurt Rohrig, Florian Steinke, Philipp Wolfrum, Thomas Leveringhaus, Thomas Lager, Lutz Hofmann, Dirk Filzek, Tina Göbel, Bettina Kusserow, Lars Nicklaus, and Peter Ritter. Kombikraftwerk 2. Technical report, Fraunhofer IWES, IEH, CUBE, SMA, Solar World, SIEMENS, DWD, ENERCON, Agentur für Erneuerbare Energien and ÖKOBIT, 2014.

- [9] Mareike Jentsch and Tobias Trost. Analyse von power-to-gas-energiespeichern im regenerativen energiesystem. Technical report, Fraunhofer-Institut für Windenergie und Energiesystemtechnik, 2014.
- [10] B. Krautkremer. Perspektiven der bioenergie.
- [11] Ulrik Neupert, Thomas Euting, Thomas Kretschmer, Claudia Notthoff, Klaus Ruhlig, and Birgit Weimert. Energiespeicher. technische grundlage und energiewirtschaftliches potenzial. Technical report, Fraunhofer Institut für Naturwissenschaftlich-Technische Trendanalysen, 2009.
- [12] Christian Doetsch, Anna Grevé, and Kurt Rohrig. Metastudie energiespeicher. Technical report, Fraunhofer-Institut für Umwelt-, Sicherheits-, und Energietechnik UMSICHT and Fraunhofer-Institut für Windenergie und Energiesystemtechnik IWES, 2014.
- [13] W. Buckles and WV Hassenzahl. Superconducting magnetic energy storage. *IEEE Power Engineering Review*, 2000.
- [14] Dagmar Oertel. Energiespeicher - stand und perspektiven. Technical report, Büro für Technikfolgen-Abschätzung beim deutschen Bundestag, 2008.
- [15] Martin Wietschel, Marlene Arens, Christian Dötsch, Sebastian Herkel, Wolfram Krewitz, Dominik Möst, and Martin Scheufen. Energietechnenergie 2050 - schwerpunkte für forschung und entwicklung. Technical report, Fraunhofer-Institut für System- und Innovationsforschung ISI, 2010.
- [16] Gert Müller-Syring, Marco Henel, Wolfgang Köppel, Herwig Mlaker, Michael Sterner, and Thomas Höcher. Entwicklung von modularen konzepten zur erzeugung, speicherung und einspeisung von wasserstoff und methan ins erdgasnetz. Technical report, Deutsche Verein des Gas- und Wasserfaches e.V. DVGW, 2013.
- [17] Joachim Nitsch, Thomas Pregger, Tobias Naegler, Dominik Heide, Diego Luca de Tena, Franz Trieb, Yvonne Scholz, Kristina Nienhaus, Norman Gerhardt, Michael Sterner, Tobias Trost, Amany von Oehsen, Rainer Schwinn, Carsten Pape, Henning Hahn, Manuel Wickert, and Bernd Wenzel. Langfristszenarien und strategien für den ausbau der erneuerbaren eenergie in deutschland bei berücksichtigung der entwicklung in europa und global. Technical report, Deutsches Zentrum für Luft-

- und Raumfahrt, Institut für Technische Thermodynamik Abt. Systemanalyse und Technikbewertung, Fraunhofer Institut für Windenergie und Energiesystemtechnik (IWES), Ingenieurbüro für neue Energien, 2012.
- [18] Tom Smolinka, Emile Tabu, and Jürgen Garcke. *Electrochemical Energy Storage for Renewable Sources and Grid Balancing*, chapter Hydrogen Production from Renewable Energies - Electrolyzer Technologies, pages 103 – 128. Elsevier B.V., 2015.
- [19] Markus Lehner, Robert Tichler, Horst Steinmüller, and Markus Koppe. *Power-to-gas: Technology and Business Models*. Springer, 2014.
- [20] F. Tietz, D. Sebold, A. Brisse, and J. Schefold. Degradation phenomena in a solid oxide electrolysis cell after 9000 h of operation. *Journal of power sources*, 223:129 – 135, 2013.
- [21] Manuel Götz, Jonathan Lefebvre, Friedemann Mörs, Amy McDaniel Koch, Frank Graf, Siegfried Bajohr, Rainer Reimert, and Thomas Kolb. Renewable power-to-gas: A technological and economic review. *Renewable Energy*, 85:1371 – 1390, 2016.
- [22] Jan Kopyscinsky, Tilman J. Schildhauer, and Serge M.A. Biollaz. Production of synthetic natural gas (sng) from coal and dry biomass - a technology review from 1950 to 2009. *Fuel*, 89(8):1763 – 1783, 2010.
- [23] Daniels L., Sparling R, and Sprott G. D. Bioenergetics of methanogenesis. *Biochimica et Biophysica Acta*, 768(2):113–163, 1984.
- [24] Frank Graf, Alexander Krajete, and Ulrich Schmack. Techno-ökonomische studie zur biologischen methanisierung bei power-to-gas-konzepten. Technical report, Deutscher Verein des Gas- und Wasserfaches e.V., 2014.
- [25] Fischer F, Lieske R, and Winzer K. Biologische gasreaktionen. i. mitteilung: die umsetzung des kohlenoxyds. *Biochem Zeitschr*, pages 247 – 267, 1931.
- [26] Fischer F, Lieske R, and Winzer K. Biologische gasreaktionen. ii: Über die bildung von essigsäure bei der biologische umsetzung von kohlenoxyd und kohlendäure mit wasserstoff zu methan. *Biochem Zeitschr*, pages 2 – 12, 1932.
- [27] Stephenson M. The chemistry of bacteria. *Annu. Rev. Biochem*, pages 485 – 502, 1933.

6. Bibliography

- [28] G. Alex Mills and Fred W. Steffgen. Catalytic methanation. *Catalysis Reviews: Science and Engineering*, 8(1):159–210, 2006.
- [29] Serge R. Guiot, Ruxandra Cimpoaia, and Gäel Carayon. Potential of wastewater-treating anaerobic granules for biomethanation of synthesis gas. *Environmental Science and Technology*, 45(5):2006 – 2012, 2011.
- [30] Klasson K. T., Elmore B. B., Vega J. L., Ackerson M. D., Clausen E. C., and Gaddy J. L. Biological production of liquid and gaseous fuels from synthesis gas. *Applied Biochemistry and Biotechnology*, 1990.
- [31] Wise D. L., Cooney C. L., and Augenstein D. C. Biomethanation anaerobic fermentation of CO_2 , H_2 and CO to methane. *Biotechnology and Bioengineering*, pages 1153 – 1172, 1978.
- [32] Barik S, Vega J. L., Clausen E. C., and Gaddy J. L. Biological conversion of coal and gas to methane. *Applied Biochemistry and Biotechnology*, 1988.
- [33] Marko Burkhardt and Günter Busch. Methanation of hydrogen and carbon dioxide. *Applied energy*, 111:74–79, 2013.
- [34] Jean-Paul Peillex, Marie-Laure Fardeau, Robert Boussand, Jean-Marie Navarro, and Jean-Pierre Belaich. Growth of *Methanococcus thermolithotrophicus* in batch and continuous culture on H_2 and CO_2 influence agitation. *Applied Microbiology and Biotechnology*, 29(6):560 – 564, 1988.
- [35] Linda M., I. de Poorter, Wim J. Geerts, and Jan T. Keltjens. Coupling of *Methanothermobacter thermoautotrophicus* methane formation and growth in fed-batch and continuous cultures under different H_2 gassing regimens. *Applied and Environmental Microbiology*, 73(3):740 – 749, 2007.
- [36] S. Rittmann, A. Seifert, and C. Herwig. Quantitative analysis of media dilution rate effects on *Methanothermobacter marburgensis* grown in continuous culture of H_2 and CO_2 . *Biomass and Bioenergy*, 36:293 – 301, 2012.
- [37] A H Seifer, S.Rittmann, S. Bernacchi, and C. Herwig. Method for assessing the impact of emission gasses on physiology and productivity in biological methanogenesis. *Bioresource Technology*, 136:747 – 751, 2013.

- [38] Keith A. Strevett, Robert F. Vieth, and Domenic Grasso. Chemo-autotrophic biogas purification for methane enrichment: mechanism and kinetics. *The Chemical Engineering Journal and the Biochemical Engineering Journal*, 58(1):71–79, 1995.
- [39] Linda M. I. de Poorter, Wim J. Geerts, and Jan T. Keltjens. Coupling of *Methanothermobacter thermautotrophicus* methane formation and growth in fed-batch and continuous cultures under different H_2 gassing regimens. *Applied and Environmental Microbiology*, 73(3):740 – 749, 2007.
- [40] Domenic Grasso, Keith Strevett, and Robert Fisher. Uncoupling mass transfer limitations of gaseous substrates in microbial systems. *The Chemical Engineering Journal and the Biochemical Engineering Journal*, 59(2):195 – 204, 1995.
- [41] J.L. Vega, E.C. Clausen, and J.L. Gaddy. Design of bioreactors for coal synthesis gas fermentations. *Resources, Conservation and Recycling*, 3(2-3):149 – 160, 1990.
- [42] K.T. Klasson, M.D. Ackerson, E.C. Clausen, and J.L. Gaddy. Bioreactors for synthesis gas fermentations. *Resources, Conservation and Recycling*, 5(2-3):145 – 165, 1991.
- [43] K. Thomas Klasson, Michael D. Ackerson, Edgar C. Clausen, and James L. Gaddy. Bioconversion of synthesis gas into liquid or gaseous fuels. *Enzyme and Microbial Technology*, 14(8):602 – 608, 1992.
- [44] Maximilian A. Schöß, Alexander Redenius, Thomas Turek, and Robert Güttel. Chemische speicherung regenerativer elektrischer energie durch methanisierung von prozessgasen aus der stahlindustrie. *Chemie Ingenieur Technik*, 86(5):734 – 739, 2014.
- [45] Kriston P. Brooks, Jianli Hu, Huayang Zhu, and Robert J. Kee. Methanation of carbon dioxide by hydrogen reduction using sabatier process in microchannel reactors. *Chemical Engineering Science*, 2006.
- [46] S. Medsford. *J. Chem Soc*, pages 123 – 1452, 1923.
- [47] H. A. Bahr and Th. Bahr. Die kohlenoxyd-spaltung an nickel. *European Journal of Inorganic Chemistry*, 61(9):2177 – 2183, 1928.

6. Bibliography

- [48] Karim Ghaib, Korbinian Nitz, and Fatima-Zahrae Ben-Fares. Katalytische methanisierung von kohlenstoffdioxid. *Chemie Ingenieur Technik*, pages 1435 – 1443, 2016.
- [49] U.S. department of energy. Fixed-bed reactor.
- [50] KH. Eisenlohr, FW. Moeller, and M. Dry. Influence of certain reaction parameters on methanation of coal to sng. *Fuels ACS Div Preprints*, 1974.
- [51] GPGP. Practical experience gained during the first twenty years of operation of the great plains gasification plant and implications for future projects. Technical report, U.S. Department of Energy office of Fossil Energy, 2006.
- [52] Hans Harms, Bernd Höhlelein, and Allan Skov. Methanisierung kohlenmonoxidreicher gase beim energie-transport. *Chemie Ingenieur Technik*, 52(6):504 – 515, 1980.
- [53] Ensell R.L and Stroud HJF. The british gas hicom methanation process sng production. In *Proceedings of the international gas research conference, British Gas Corporation*, pages 472 – 481, 1983.
- [54] G. A. White, T. R. Roszkowski, and D. W. Standbridge. *Methanation of Synthesis Gas*, chapter The RMProcess, pages 138 – 148. American chemical society, 1975.
- [55] M. D. Schlesinger, J.J. Demeter, and Murray Greyson. Catalyst for producing methane from hydrogen and carbon monoxide. *Industrial & Engineering Chemistry*, 48(1):68–70, 1956.
- [56] Streeter RC, editor. *Recent developments in fluidized-bed methanation reserach. In: Proceedings of ninth synthetic pipeline gas symposium*, 1977.
- [57] Greyson M., Demeter J.J., Schlesinger M.D, Johnson G.E., Jonakin J., and Myers J.W. Synthesis of methane. Technical report, U.S. Bur. of Mines, 1955.
- [58] James T. Cobb Jr. and Robert C. Streeter. Evaluation of fluidized-bed methanation catalyst and reactor modeling. *Industrial & Engineering Chemistry Process Design and Development*, 18(4):672 – 678, 1979.
- [59] Lommerzheim W and Flockenhaus C. One stage combined shift-conversion and partial methanation process for upgrading synthesis gas to pipeline quality. In *Proceedings of tenth synthetic pipeline gas Symposium*. American Gas Association, 1978.

- [60] Perry M and Eliason D. CO₂ recovery and sequestration at dakota gasification company inc. Technical report, Gasification technology conference, 2004.
- [61] Rajamani Krishna, Jeroen W.A. De Swart, Jürg Ellenberger, and Gilbert B. Martina. Gas holdup in slurry bubble columns: Effect of column diameter and slurry concentrations. *AlChE Journal*, 1997.
- [62] Ashfag Shaikh. *Bubble and slurry bubble column reactors: Mixing, flow regime transition and scaleup*. PhD thesis, Washington university. Department of Energy, Environmental and chemical Engineering, 2007.
- [63] Peter M. Wilkinson, Arie P. Spek, and Laurent L. van Dierendonck. Design parameters estimation for scale-up of high-pressure bubble columns. *AlChE Journal*, 38(4):544 – 554, 1992.
- [64] Frank ME, Sherwin MB, and Mednick RL. Liquid phase methanation - shift pdu results and pilot plant status. In *Proceeding of eighth synthetic pipeline gas symposium*. American Gas Association, 1976.
- [65] Manuel Götz. *Methanisierung im Dreiphasen-Reaktor*. PhD thesis, Karlsruher Institut für Technologie (KIT) Fakultät für Chemieingenieurwesen und Verfahrenstechnik, 2014.
- [66] Dominik Schollenberger. Nutzung von wabenreaktoren zur methanisierung bei ptg-prozessen. Master's thesis, Karlsruher Institut für Technologie Institut für Technische Chemie und Polymerchemie, 2013.
- [67] Gunther Kolb and Volker Hessel. Micro-structured reactors for gas phase reactions. *Chemical Engineering Journal*, 98(1-2):1–38, 2004.
- [68] T. Cui, J. Fang, J. Maxwell, J. Gardner, R. Besser, and B. Elmore. Proceedings of the 4th international conference on microreaction technology. 2000.
- [69] R. Besser and M. Prevot. Proceedings of the 4th international conference on microreaction technology. page 278, 2000.
- [70] X. Ouyang and R. Besser. Proceedings of the aiche spring meeting topical conference. page 254, 2002.

- [71] V. Cominos, S.Hardt, V.Hessel, G.Kolb, H.Löwe, M.Wichert, and R.Zapf. A methanol steam micro-reformer for low power fuel cell applications. *Chemical Engineering Communications*, 192(5), 2005.
- [72] Patrick L. Mills, David J. Quiram, and James F. Ryley. Microreactor technology and process miniaturization for catalytic reactions - a perspective on recent developments and emerging technologies. *Chemical Engineering Science*, 62(24):6992–7010, 2007.
- [73] J.-C. Charpentier. Process intensification by miniaturization. *Chemical Engineering & Technology*, 28(3):255–258, 2005.
- [74] J.M. Commenge, L. Falk, J.P. Corriou, and M. Matlosz. Optimal design for flow uniformity in microchannel reactors. *AIChE Journal*, 48(2):345–358, 2002.
- [75] V. Hessel and H. Löwe. Microchemical engineering: Components, plant concepts, user acceptance - part ii. *Chemical Engineering & Technology*, 26(4):391–408, 2003.
- [76] Kazuhiro Mae. Advanced chemical processing using microspace. *Chemical Engineering Science*, 62(18-20), 2007.
- [77] Helmut Pennemann, Paul Watts, Stephen J. Haswell, Volker Hessel, and Holger. Benchmarking of microreactor applications. *Organic Process Research & Development*, 8(3):422–439, 2004.
- [78] Helmut Pennemann, Volker Hessel, and Holger Löwe. Chemical microprocess technology-from laboratory-scale to production. *Chemical Engineering Science*, 59(22-23):4789–4794, 2004.
- [79] Klavs F. Jensen. Microreaction engineering - is small better? *Chemical Engineering Science*, 56(2):293 – 303, 2001.
- [80] A.J. Franz, D.J. Quiram, R. Srinivasan, I.-M.Hsing, S.L. Firebaugh, K.F. Jensen, and M.A. Schmidt. Proceedings of the 2nd international conference on microreaction technology. Number 33, 1998.
- [81] Ch. Alépée, R. Maurer, L. Parette, L. Vulpecu, Ph. Renaud, and A. Renken. Proceedings of the 3rd international conference on microreaction technology. 1999.
- [82] Georg Wießmeier and Dieter Hönicke. Heterogeneously catalyzed gas-phase hydrogenation of cis, trans,trans-1,5,9-cyclododecatriene on palladium catalysts having

-
- regular pore systems. *Industrial & Engineering Chemistry Research*, 35(12):4412 – 4416, 1996.
- [83] A. Kursawe, R. Pilz, H. Dürr, and D. Hönicke. Proceedings of the 4th international conference on microreaction technology. 2000.
- [84] G. Kolb, J. Schürer, D. Tiemann, M. Wichert, R. Zapf, V. Hessel, and H. Löwe. Fuel processing in integrated micro-structured heat-exchanger reactors. *Journal of power sources*, 2007.
- [85] S.P. Fitzgerald, R.S. Wegend, A.Y. Tonkovich, Y. Wang, H.D. Freeman, J.L. Marco, G.L. Roberts, and D.P. VanderWiel. Proceedings of the 4th international conference on microreaction technology. 2000.
- [86] S. Walter, E. Joannet, M. Schiel, I. Boulet, R. Philips, and M.A. Liauw. Proceedings of the 5th international conference on microreaction technology. 2000.
- [87] A.I.Y. Tonkovich, D.M. Jimenez, J.L. Zilka, M.J. LaMont, Y. Wang, and R.S. Wegeng. Proceedings of the 2nd international conference on microreaction technology. 1998.
- [88] M. Kevin Drost, Chuck Call, Judy Cuta, and Robert Wegeng. Microchannel combustor evaporator thermal processes. *Microscale thermophysical engineering*, 1(4), 2010.
- [89] Calvin H. Bartholomew. Mechanism of catalyst deactivation. *Applied Catalysis A: General*, 212(1 - 2):17 – 60, 2001.
- [90] B. Delmon and G.F. Froment, editors. *Studies in Surface Science and Catalyst*. Elsevier, 1987.
- [91] B. Delmon and G.F., editors. *Studies in Surface Science and Catalyst*. Elsevier, 1980.
- [92] Jonathan Lefebvre, Manuel Götz, Siegfried Bajohr, Rainer Reimert, and Thomas Kolb. Improvement of three-phase methanation reactor performance for steady-state and transient operation. *Fuel Processing Technology*, 132:83–90, 2015.
- [93] Michael Sterner. *Bioenergy and renewable power methane in integrated 100% renewable energy systems*. PhD thesis, Universität Kassel, 2009.

6. Bibliography

- [94] Tanja Schaaf, Jochen Grünig, Markus Roman Schuster, Tobias Rothenfluh, and Andreas Orth. Methanation of CO_2 - storage of renewable energy in a gas distribution system. *Energy, Sustainability and Society*, 2014.
- [95] Bundesministerium für Wirtschaft und Energie. Energiedaten: Gesamtausgabe. Technical report, Bundesministerium für Wirtschaft und Energie, 2015.
- [96] Tobias Trost, Mareike Jentsch, Uwe Holzhammer, and Sönke Horn. Die Biogasanlagen als zukünftigen CO_2 -produzenten für die Herstellung von erneuerbarem Methan. Technical report, Fraunhofer Institut für Windenergie und Energiesystemtechnik (IWES), März 2012.
- [97] Biogaspartner. Biogaseinspeisung in Deutschland, September 2016.
- [98] Dennis Y.C. Leung, Giorgio Caramanna, and M. Mercedes Maroto-Valer. An overview of current status of carbon dioxide capture and storage technologies. *Renewable and Sustainable Energy Reviews*, 39:426 – 443, 2014.
- [99] Veawab A, Aroonwilas A, and Tontiwachwuthikul P. CO_2 absorption performance of aqueous alkanolamines in packed columns. In *ACS Division of Fuel Chemistry, Preprints*, volume 47, pages 49–50, 2002.
- [100] *Experience with CO_2 capture from coal flue gas in pilot-scale: Testing of different amine solvents*, volume 1, 2009.
- [101] Hari Prasad Mangalapally, Ralf Notz, Sebastian Hoch, Norbert Asprion, Georg Sieder, Hugo Garcia, and Hans Hasse. Pilot plant experimental studies of post combustion CO_2 capture by reactive absorption with MEA and new solvents. *Energy Procedia*, 1(1):963 – 970, 2009.
- [102] J. Kittel, R. Idem, D. Gelowitz, P. Tontiwachwuthikul, G. Parrain, and A. Bonneau. Corrosion in MEA units for CO_2 capture: pilot plant studies. *Energy Procedia*, 1(1):791 – 797, 2009.
- [103] Anirban Nandy, Chanchal Loha, Sai Gu, Pinaki Sarkar, Malay K. Karmakar, and Pradip K. Chatterjee. Present status and overview of chemical looping combustion technology. *Renewable and Sustainable Energy Reviews*, 59:597 – 619, 2014.

- [104] Andreas Thon, Marvin Kramp, Ernst-Ulrich Hartge, Stefan Heinrich, and Joachim Werther. Operational experience with a system of coupled fluidized beds for chemical looping combustion of solid fuels using ilmenite as oxygen carrier. *Applied Energy*, 118:309 – 317, 2014.
- [105] Jochen Ströhle, Matthias Orth, and Bernd Epple. Chemical looping combustion of hard coal in a 1 mw_{th} pilot plant using ilmenite as oxygen carrier. *Applied Energy*, 157:288 – 294, 2015.
- [106] Silje Fosse Håkonsen, Carlos A. Grande, and Richard Blom. Rotating bed reactor for clc: Bed characteristics dependencies on internal gas mixing. *Applied Energy*, 113:1952 – 1957, 2014.
- [107] Roda Bounaceur, Nancy Lape, Denis Roizard, Cécile Vallieres, and Eric Favre. Membrane prprocess for post-combustion carbon dioxide capture: A parametric study. *Energy*, 31(14):2556 – 2570, 2006.
- [108] A. Brunetti, F.Scura, G. Barbieri, and E. Drioli. Membrane technologies for co₂ separation. *Journal of Membrane Science*, 359(1 - 2):115 – 125, 2010.
- [109] Ponnivalavan Babu, Praveen Linga, Rajnish Kumar, and Peter Englezos. A review of the hydrate based gas separation (hbgs) process for carbon dioxide pre-combustion capture. *Energy*, 85:261 – 279, 2015.
- [110] Nexant. Simteche hydrate co₂ capture process. Technical report, Nexant and SIMTECHE and los Alamos National Laboratory, 2006.
- [111] Peter Atkins and Julio de Paula. *Physical chemistry*. Oxford University Press, eighth edition, 2006.
- [112] R. Kee, M. Coltring, and P. Glarborg. *Chemically Reacting Flow: Theory and Practice*. Wiley-Interscience, 2003.
- [113] Peter J. Lunde. Modeling, simulation, and operation of a sabatier reactor. *Industrial & Engineering Chemistry Research Process Design and Development*, 13(3):226 – 233, 1974.
- [114] Peter J. Lunde and Frank L. Kester. Kinetics of carbon dioxide methanation on a ruthenium catalyst. *Industrial & Engineering Chemistry Process Design and Development*, 1974.

6. Bibliography

- [115] Peter J. Lunde and Frank L. Kester. Carbon dioxide methanation on a ruthenium catalyst. *Industrial & Engineering Chemistry Process Design and Development*, 13(1):27–33, 1974.
- [116] Haruhiko Ohya, Jun Fun, Hironori Kawamura, Koutarou Itoh, Hirofumi Ohashi, Masahiko Aihara, Shigeharu Tanisho, and Youichi Negishi. Methanation of carbon dioxide by using membrane reactor integrated with water vapor permselective membrane and its analysis. *Journal of membrane of science*, 131(1-2):237 – 247, 1997.
- [117] Hanaa Er-rbib and Chakib Bouallou. Modeling and simulation of co methanation process for renewable electricity storage. *Energy*, 75, 2014.
- [118] Jan Kopyscinsky, Tilman J. Schildhauer, and Serge M.A. Biollaz. Methanation in a fluidized bed reactor with high initial co partial pressure: Part ii - modeling and sensitivity study. *Chemical Engineering Science*, 66(8):1612 – 1621, 2011.
- [119] David Schlereth and Olaf Hinrichsen. A fixed-bed reactor modeling study on the methanation of CO_2 . *Chemical engineering research and design*, 92(4):702 – 712, 2014.
- [120] Jianguo Xu and Gilbert F. Froment. Methane steam reforming, methanation and water-gas shift: I. intrinsic kinetics. *AIChE Journal*, 35(1):88 – 96, 1989.
- [121] Baolin Hou, Yanqiang Huang, Xiaodong Wand, Xiaofeng Yang, Hongming Duan, and Tao Zhang. Optimization and simulation of the sabatier reaction process in a packed bed. *Transport phenomena and fluid mechanics*, 62(8):2879 – 2892, 2016.
- [122] Laxminarayan L. Raja, Robert J. Kee, Olaf Deutschmann, and Juergen WarnatRobert J. Kee. Schmidt. A critical evaluation of navier-stokes, boundary-layer, and plug-flow models of the flow and chemistry in a catalytic-combustion monolith. *Catalysis today*, 59(1-2):47–60, June 2000.
- [123] C.R. Wilke. A viscosity equation for gas mixtures. *The Journal of chemical Physics*, 1949.
- [124] Fabian Bonnet. Entwicklung und implementierung einer simulationsumgebung zur regelung und betriebsführung einer methanisierungsanlage im labormaßstab. Master’s thesis, Universität Kassel - Fachbereich Elektrotechnik/Informatik, 2016.

- [125] Alan V. Oppenheim and George C. Verghese. Signals system and inference, 2010.
- [126] Frank Schünemeyer, Henning Hahn., Lena Vogel., Dirk Kirchner., and Jochen Bard. Direktmethanisierung von biogas. Technical report, Fraunhofer-Institut für Windenergie und Energiesystemtechnik, IWES, 2015.
- [127] ICT-IMM. Methanisierungsreaktor-katalysatortests. 2014.
- [128] Fraunhofer ICT-IMM. Methanisierungs-reaktor met-01. 2014.
- [129] Agilent Technologies. *Agilent 490 Micro Gas Chromatograph User Manual*. Agilent Technologies, fifth edition, July 2016.

7 Appendix

Graphical representation of the PtG-plant



Figure 7.1: PtG lab-scale plant. Source: Fraunhofer IEE

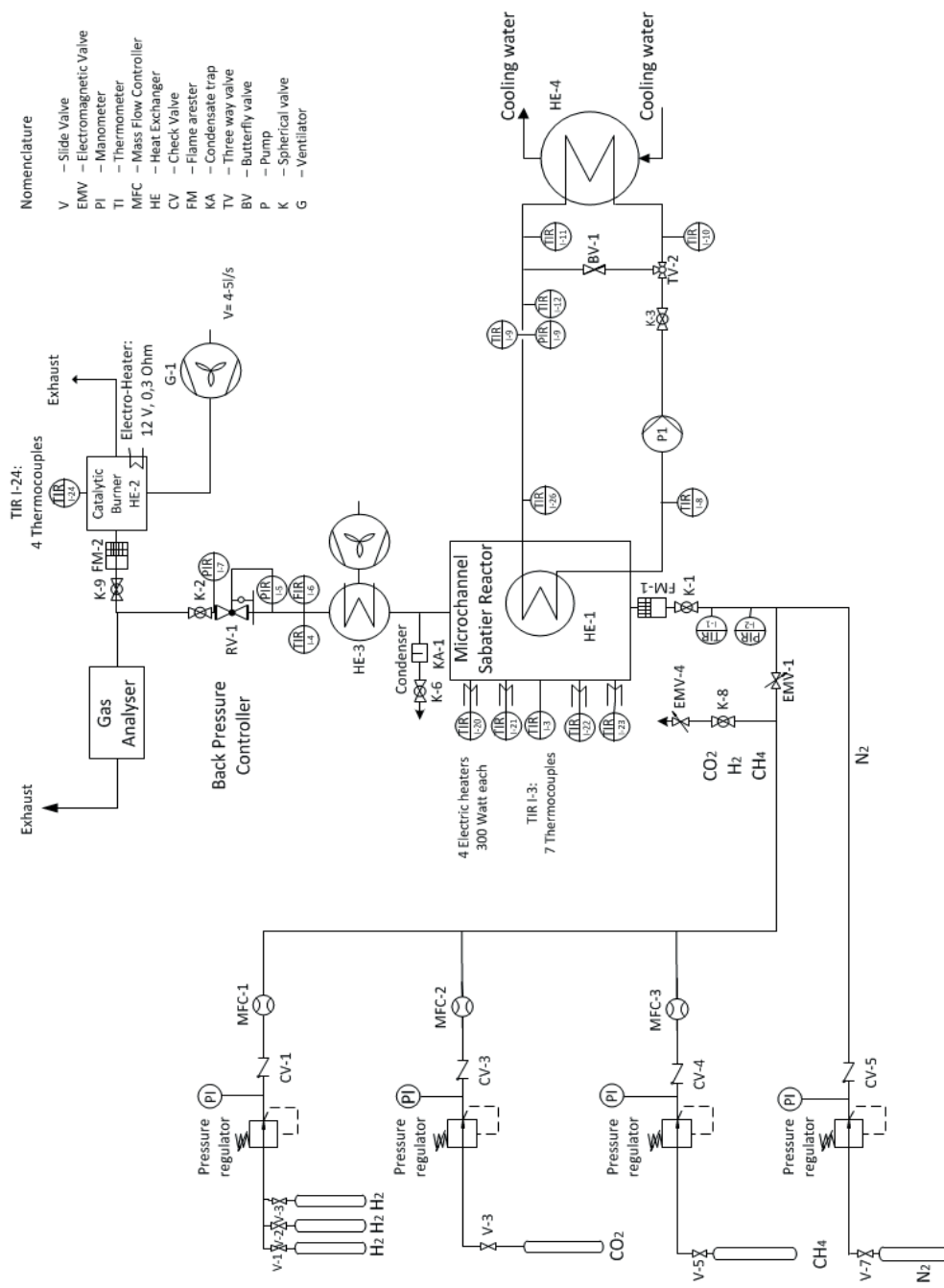


Figure 7.2: PtG process diagram. Source: Fraunhofer IEE

Experimental conditions for the determination of E_a and A

Test Nummer	Rep	Reactor Temp [°C]	Inlet VolFlow [l/h]	Inlet Partial. P CO ₂ [bar]	Inlet Partial. P H ₂ [bar]	Inlet Partial P CH ₄ [bar]	Outlet Partial P CO ₂ [bar]	Outlet Partial P H ₂ [bar]	Outlet Partial P CH ₄ [bar]	Outlet Partial P H ₂ O [bar]
EA-1	Rep.1	300	1006,800	5,800	9,200	0,000	5,781	8,968	0,0839	0,168
	Rep.2	300	1006,800	5,800	9,200	0,000	5,781	8,972	0,0825	0,165
	Rep.3	300	1006,800	5,800	9,200	0,000	5,781	8,974	0,0817	0,163
	Rep.4	300	1006,800	5,800	9,200	0,000	5,781	8,978	0,0804	0,161
	Rep.5	300	1006,800	5,800	9,200	0,000	5,781	8,979	0,0798	0,160
EA-2	Rep.1	305	940,410	5,073	9,927	0,000	5,041	9,665	0,0977	0,195
	Rep.2	305	940,410	5,073	9,927	0,000	5,042	9,670	0,0959	0,192
	Rep.3	305	940,410	5,073	9,927	0,000	5,042	9,669	0,0964	0,193
	Rep.4	305	940,410	5,073	9,927	0,000	5,042	9,672	0,0952	0,190
	Rep.5	305	940,410	5,073	9,927	0,000	-	-	-	-
EA-3	Rep.1	310	940,400	3,112	11,888	0,000	3,038	11,583	0,1262	0,252
	Rep.2	310	940,400	3,112	11,888	0,000	3,039	11,588	0,1244	0,249
	Rep.3	310	940,400	3,112	11,888	0,000	3,040	11,591	0,1229	0,246
	Rep.4	310	940,400	3,112	11,888	0,000	3,041	11,595	0,1215	0,243
	Rep.5	310	940,400	3,112	11,888	0,000	3,041	11,595	0,1212	0,242
EA-4	Rep.1	315	965,410	5,073	9,927	0,000	5,023	9,514	0,1544	0,309
	Rep.2	315	965,410	5,073	9,927	0,000	5,025	9,531	0,1481	0,296
	Rep.3	315	965,410	5,073	9,927	0,000	5,026	9,540	0,1445	0,289
	Rep.4	315	965,410	5,073	9,927	0,000	5,026	9,540	0,1445	0,289
	Rep.5	315	965,410	5,073	9,927	0,000	5,026	9,540	0,1446	0,289
EA-5	Rep.1	320	933,970	5,856	7,940	1,205	5,811	7,337	1,4426	0,410
	Rep.2	320	933,970	5,856	7,940	1,205	5,809	7,314	1,4517	0,426
	Rep.3	320	933,970	5,856	7,940	1,205	5,809	7,319	1,4495	0,422
	Rep.4	320	933,970	5,856	7,940	1,205	5,803	7,239	1,4811	0,476
	Rep.5	320	933,970	5,856	7,940	1,205	5,810	7,321	1,4487	0,420
EA-6	Rep.1	325	958,220	5,881	7,854	1,265	5,833	7,193	1,5263	0,448
	Rep.2	325	958,220	5,881	7,854	1,265	5,833	7,199	1,5242	0,444
	Rep.3	325	958,220	5,881	7,854	1,265	5,834	7,208	1,5206	0,438
	Rep.4	325	958,220	5,881	7,854	1,265	5,834	7,207	1,5207	0,438
	Rep.5	325	958,220	5,881	7,854	1,265	5,834	7,210	1,5195	0,436
EA-7	Rep.1	330	933,960	2,998	11,327	0,675	2,773	10,396	1,0829	0,748
	Rep.2	330	933,960	2,998	11,327	0,675	2,719	10,172	1,1808	0,928
	Rep.3	330	933,960	2,998	11,327	0,675	2,733	10,230	1,1553	0,881
	Rep.4	330	933,960	2,998	11,327	0,675	2,777	10,414	1,0749	0,734
	Rep.5	330	933,960	2,998	11,327	0,675	2,780	10,424	1,0708	0,726
EA-8	Rep.1	335	974,390	2,779	10,262	1,959	2,612	9,565	2,2936	0,530
	Rep.2	335	974,390	2,779	10,262	1,959	2,613	9,570	2,2909	0,526
	Rep.3	335	974,390	2,779	10,262	1,959	2,617	9,586	2,2835	0,514
	Rep.4	335	974,390	2,779	10,262	1,959	2,619	9,594	2,2794	0,507
	Rep.5	335	974,390	2,779	10,262	1,959	2,615	9,577	2,2877	0,521
EA-9	Rep.1	340	934,420	6,421	3,846	4,733	6,377	2,786	5,2291	0,608
	Rep.2	340	934,420	6,421	3,846	4,733	6,377	2,801	5,2221	0,600
	Rep.3	340	934,420	6,421	3,846	4,733	6,381	2,893	5,1788	0,547
	Rep.4	340	934,420	6,421	3,846	4,733	6,382	2,916	5,1683	0,534
	Rep.5	340	934,420	6,421	3,846	4,733	6,383	2,929	5,1623	0,526
EA-10	Rep.1	345	934,420	6,421	3,846	4,733	6,383	2,927	5,1628	0,527
	Rep.2	345	934,420	6,421	3,846	4,733	6,385	2,972	5,1419	0,501
	Rep.3	345	934,420	6,421	3,846	4,733	6,386	2,997	5,1304	0,487
	Rep.4	345	934,420	6,421	3,846	4,733	6,386	3,015	5,1217	0,477
	Rep.5	345	934,420	6,421	3,846	4,733	6,388	3,050	5,1057	0,457
EA-11	Rep.1	350	935,310	6,225	5,510	3,266	6,159	4,237	3,8247	0,779
	Rep.2	350	935,310	6,225	5,510	3,266	6,159	4,242	3,8226	0,776
	Rep.3	350	935,310	6,225	5,510	3,266	6,160	4,262	3,8141	0,764
	Rep.4	350	935,310	6,225	5,510	3,266	6,163	4,320	3,7883	0,728
	Rep.5	350	935,310	6,225	5,510	3,266	6,165	4,348	3,7760	0,711

Figure 7.3: Experimental conditions and outlet partial pressures of the gas components used for the determination of E_a .

Appendix

Test Nummer	Rep	Reactor Temp [°C]	Inlet VolFlow [l/h]	Inlet Partial. P CO ₂ [bar]	Inlet Partial. P H ₂ [bar]	Inlet Partial P CH ₄ [bar]	Outlet Partial P CO ₂ [bar]	Outlet Partial P H ₂ [bar]	Outlet Partial P CH ₄ [bar]	Outlet Partial P H ₂ O [bar]
A-1	Rep.1	330	950,67	5,073	9,927	0,000	4,996	9,289	0,238	0,477
	Rep.2	330	950,67	5,073	9,927	0,000	4,962	9,006	0,344	0,688
	Rep.3	330	950,67	5,073	9,927	0,000	4,995	9,279	0,242	0,484
	Rep.4	330	950,67	5,073	9,927	0,000	4,997	9,301	0,234	0,468
	Rep.5	330	950,67	5,073	9,927	0,000	4,998	9,307	0,232	0,463
A-2	Rep.1	325	954,4	5,474	8,389	1,137	5,401	7,611	1,448	0,540
	Rep.2	325	954,4	5,474	8,389	1,137	5,404	7,635	1,438	0,523
	Rep.3	325	954,4	5,474	8,389	1,137	5,404	7,636	1,438	0,523
	Rep.4	325	954,4	5,474	8,389	1,137	5,404	7,644	1,435	0,517
	Rep.5	325	954,4	5,474	8,389	1,137	5,406	7,659	1,429	0,506
A-3	Rep.1	320	950,68	5,679	7,602	1,719	5,650	7,240	1,868	0,242
	Rep.2	320	950,68	5,679	7,602	1,719	5,650	7,239	1,868	0,243
	Rep.3	320	950,68	5,679	7,602	1,719	5,650	7,235	1,870	0,246
	Rep.4	320	950,68	5,679	7,602	1,719	5,650	7,237	1,869	0,244
	Rep.5	320	950,68	5,679	7,602	1,719	5,650	7,239	1,868	0,243
A-4	Rep.1	315	951,52	5,909	6,721	2,370	5,883	6,345	2,529	0,242
	Rep.2	315	951,52	5,909	6,721	2,370	5,882	6,324	2,538	0,256
	Rep.3	315	951,52	5,909	6,721	2,370	5,882	6,329	2,536	0,252
	Rep.4	315	951,52	5,909	6,721	2,370	5,883	6,336	2,533	0,248
	Rep.5	315	951,52	5,909	6,721	2,370	5,883	6,337	2,533	0,247
A-5	Rep.1	310	948,52	6,338	5,077	3,585	6,312	4,526	3,830	0,332
	Rep.2	310	948,52	6,338	5,077	3,585	6,313	4,540	3,824	0,323
	Rep.3	310	948,52	6,338	5,077	3,585	6,313	4,544	3,822	0,321
	Rep.4	310	948,52	6,338	5,077	3,585	6,314	4,562	3,814	0,310
	Rep.5	310	948,52	6,338	5,077	3,585	6,314	4,572	3,810	0,304
A-6	Rep.1	300	956,27	3,999	6,865	4,136	3,967	6,650	4,244	0,140
	Rep.2	300	956,27	3,999	6,865	4,136	3,964	6,633	4,253	0,151
	Rep.3	300	956,27	3,999	6,865	4,136	3,962	6,617	4,260	0,161
	Rep.4	300	956,27	3,999	6,865	4,136	3,959	6,600	4,269	0,172
	Rep.5	300	956,27	3,999	6,865	4,136	3,958	6,595	4,272	0,175
A-7	Rep.1	300	1008,2	3,869	11,132	0,000	3,814	10,848	0,113	0,226
	Rep.2	300	1008,2	3,869	11,132	0,000	3,821	10,883	0,099	0,197
	Rep.3	300	1008,2	3,869	11,132	0,000	3,823	10,895	0,094	0,188
	Rep.4	300	1008,2	3,869	11,132	0,000	3,822	10,890	0,096	0,192
	Rep.5	300	1008,2	3,869	11,132	0,000	3,822	10,892	0,095	0,190
A-8	Rep.1	300	1018,8	3,956	8,290	2,754	3,925	8,101	2,844	0,131
	Rep.2	300	1018,8	3,956	8,290	2,754	3,924	8,098	2,845	0,133
	Rep.3	300	1018,8	3,956	8,290	2,754	3,923	8,091	2,848	0,138
	Rep.4	300	1018,8	3,956	8,290	2,754	3,924	8,095	2,846	0,135
	Rep.5	300	1018,8	3,956	8,290	2,754	3,924	8,097	2,845	0,134
A-9	Rep.1	300	1019,8	5,986	5,663	3,351	5,971	5,423	3,458	0,148
	Rep.2	300	1019,8	5,986	5,663	3,351	5,970	5,412	3,463	0,155
	Rep.3	300	1019,8	5,986	5,663	3,351	5,970	5,411	3,464	0,155
	Rep.4	300	1019,8	5,986	5,663	3,351	5,970	5,418	3,461	0,151
	Rep.5	300	1019,8	5,986	5,663	3,351	5,972	5,439	3,451	0,138
A-10	Rep.1	300	1016,8	5,640	7,754	1,607	5,623	7,551	1,689	0,137
	Rep.2	300	1016,8	5,640	7,754	1,607	5,625	7,579	1,678	0,118
	Rep.3	300	1016,8	5,640	7,754	1,607	5,625	7,577	1,679	0,119
	Rep.4	300	1016,8	5,640	7,754	1,607	5,624	7,570	1,682	0,124
	Rep.5	300	1016,8	5,640	7,754	1,607	5,625	7,574	1,680	0,121
A-11	Rep.1	300	1013,7	5,073	9,927	0,000	5,044	9,690	0,089	0,177
	Rep.2	300	1013,7	5,073	9,927	0,000	5,045	9,700	0,085	0,170
	Rep.3	300	1013,7	5,073	9,927	0,000	-	-	-	-
	Rep.4	300	1013,7	5,073	9,927	0,000	-	-	-	-
	Rep.5	300	1013,7	5,073	9,927	0,000	-	-	-	-

Figure 7.4: Experimental conditions and outlet partial pressures of the gas components used for the determination of the pre-exponential Arrhenius factor A .

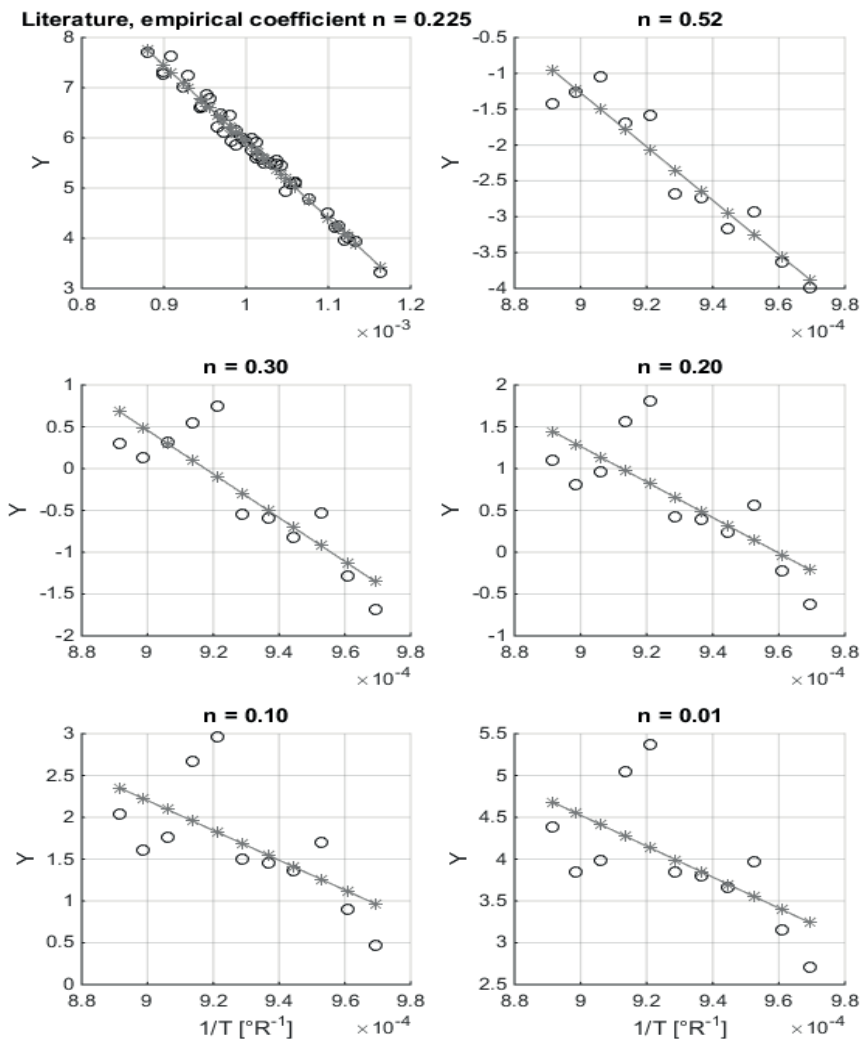


Figure 7.5: Y vs the inverse of the reactor temperature. Comparison between the values found by Lunde and Kester and the values found experimentally in the lab.

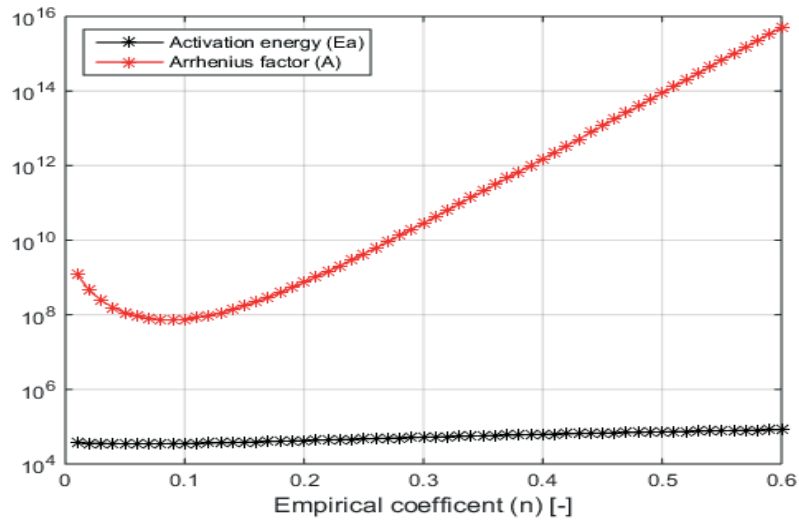


Figure 7.6: Values of the activation energy Ea and the pre-exponential Arrhenius factor A vs n .

The scope of this dissertation is the development of a state observer for Power-to-Gas (PtG) plants. A physical performance model of an innovative reactor concept for different operation conditions has been developed and implemented in Matlab-Simulink. Experiments in a lab-scale PtG plant are used to validate the model; a comparison between the experimental and modelled data is presented. The experiments cover a wide temperature range, different operating pressures and inlet volumetric flows. Furthermore, experimental runs are carried out to determine the experimental value of the kinetic parameters, namely the activation energy (E_a), the pre-exponential factor of the Arrhenius form (A) and an empirical coefficient (n). The state observer predicts the performance of the reactor for a specific operating point and allows to identify a decrease of the reactor performance, such an identification of a system state leads to maintenance or modifications in the operating control.

ISBN 978-3-8396-1378-8



9 783839 613788